Simulation of Amorphous Silicon Anode in Lithium-Ion Batteries

By

Miao Wang

A DISSERTATION

Submitted to
Michigan State University
in partial fulfillment of the requirements
for the degree of

Mechanical Engineering - Doctor of Philosophy

2017

ABSTRACT

SIMULATION OF AMORPHOUS SILICON ANODE IN LITHIUM-ION BATTERIES

By

Miao Wang

The energy density of the current generation of Li-ion batteries (LIBs) is only about 1% of that of gasoline. Improving the energy density of the LIBs is critical for vehicle electrification. Employing high capacity electrode materials is a key factor in this endeavor. Silicon (Si) is one of the high capacity anode materials for LIBs. However, Si experiences large volume variation (up to 300%) during battery cycling, which affects the structural integrity of battery and results in rapid capacity fading. It has been shown that the cycle life of Si anode can be improved greatly through novel electrode designs. So far, such work is conducted through experiments.

Numerical simulations have the potentials for design optimization of LIBs, as demonstrated in multiphysics models for LIBs with graphite anode. This research extends a previously developed microstructure-resolved multiphysics (MRM) model to LIBs with amorphous Si anode. The MRM model considers the electrochemical reactions, Li transport in electrodes and electrolyte, lithiation induced volume change, mechanical strains and stresses, material property evolution with lithiation, and the chemo-mechanical coupling. The model is solved using finite element package COMSOL Multiphysics.

The major challenges in this work are the large deformation of the Si, and the uncertainty in parameters and the coupling relation. To simulate the large deformation of Si, a large strain based formulation for the concentration induced volume expansion was used. The electrolyte was modeled as fluid. A method to simulate the galvanostatic charge/discharge of a finite deformation electrode with moving boundary was developed.

Important model parameters were determined one by one by correlating the simulation to appropriate experiments. For example, the Li diffusivity in Si reported in literature varies from 10^{-13} to 10^{-19} m²/s. To estimate this parameter, the in-situ transmission electron microscope experiment of two-phase lithiation of a-Si nanospheres was simulated. The diffusivity was found at the order of 2×10^{-17} m²/s for the lithium poor phase in first lithiation and 2×10^{-15} m²/s for lithium rich phase and in subsequent cycles. The reaction rate constant and the apparent transfer coefficient are determined in a similar way using different experiments.

In literature, different forms of chemo-mechanical coupling theories have been proposed for Li diffusion in Si. The coupling relationship and parameters were often derived based on one type of experiment even though the process is highly coupled. In this work, the chemo-mechanical coupling was investigated by simulations of two geometries: a thin film and a sphere. A strong asymmetric rate behavior between lithiation and delithiation has been observed in thin film a-Si anode but not in other geometries. The results reveal that the rate behavior is affected by the geometry and the constraint of the electrode, the chemo-mechanical coupling, and the prior process. A substrate-constrained film has a relatively low surface/volume ratio and a constant surface area. Its lithiation has a great tendency to be hindered by surface limitation. The chemo-mechanical coupling plays an important role in the specific rate behavior of a geometry.

Finally, an MRM model was built for a half cell with a-Si nanowalls as anode. The specific and volumetric capacities of the cell as a function of size, length/size ratio, spacing of the nanostructure, and the Li⁺ concentration in electrolyte were investigated. The results show that the factors reducing the concentration polarization can enhance the maximum achievable SOC of the cell. However, the cell with the highest SOC does not necessarily lead to the highest capacity.

ACKNOWLEDGEMENT

First of all, I would like to express my deepest appreciation to my advisor, Prof. Xinran Xiao. After spending a few years with her for my Ph.D. study, I learned a lot and progress greatly. Her attitude towards research and life inspired me greatly. She is always very informative and respectful. She patiently guided me through difficulties in my research, not only on specific problems, but also on the research methodologies. She trained me repeatedly to become an independent researcher. Moreover, she always encouraged me to become a better person, full with courage and hope towards my life. Her integrity, hardworking and ethnic set an excellent example for me to follow.

I would like to express my deep thanks to my committee members, Professors Alejandro Diaz, Peter Lillehoj and Jason Nicholas for their helpful directions and suggestions on my researches. Additionally, special thanks to our collaborator, Dr. Xiaosong, Huang, at General Motor R&D for his helpful discussions and technical contributions to this project. It has been a great pleasure to work with him.

I also want to thank all my friends at Michigan State University I made through these years: Wei Zhang, Wu Zhou, Shutian Yan, Danghe Shi, Christopher Cater and Andy Vanderklok, etc. It has been a pleasure to know you and spent such a wonderful time with you.

The most importantly, I want to thank my beloved ones for their truthful care, endless love and support. This work is dedicated to my parents. I would like to thank my husband, Fang Hou for his being with me.

This research is supported by NSF CMMI 1030821, the start-up funding to Dr. Xiao from Michigan State University and support from Department of Mechanical Engineering.

TABLE OF CONTENTS

LIST OF TA	ABLES	viii
LIST OF FI	GURES	x
KEY TO AI	BBREVIATIONS	xv
Chapter 1	Introduction	1
	hium-Ion Battery	
	Anode	
	ope of the Work	
	tline of the Dissertation	
Chapter 2	Literature Review	11
2.1 Lit	hiation of Silicon	11
2.1.1	Two-Phase and Single-Phase Lithiation	11
2.1.2	Lithiation Induced Volume Expansion	13
2.2 Ch	emical-Mechanical Two Way Coupling	14
2.2.1	Experimental Observations	14
2.2.2	Theories for Diffusion Induced Stress	16
2.2.3	Theories for Stress Influenced Li Diffusion	18
2.2.3.	1 Stress Effect on Li Diffusivity	20
2.2.3.	2 Stress Effect on Chemical Potential	20
2.3 Ma	terial Property Variations during Si Lithiation	22
2.3.1	Li Diffusivity in Si	
2.3.2	Electrochemical Kinetics with Si Anode	23
2.3.3	Mechanical Properties	23
2.4 Sin	nulation of Si Particles and Li-Ion Cells	24
2.4.1	Si Anode	25
2.4.2	Li-Ion Cell	26
2.4.3	Modeling of Li Transport	27
Chapter 3	Microstructural-Resolved Multiphysics Model for Li-ion Battery	29
	attery" Sub-Model	
3.1.1	Mass Transport	
3.1.2	Electron Transport	
3.1.3	Electrochemical Kinetics	34
3.1.4	Boundary Conditions	36
3.2 "St	ress" Sub-Model	
3.2.1	Deformation of Si	
3.2.2	Coupling between Li Transport inside Si and Volume Expansion	
3.2.3	Stress Generation in Si	
3.2.4	Fluid Electrolyte	41
325	Current Collector	42

3.2.6 Boundary Conditions	42
3.3 Modeling Parameters	43
3.3.1 Parameters in "Battery" Sub-Model	43
3.3.1.1 Electrode Properties	
3.3.1.2 Electroly Properties	
3.3.2 Mechanical Properties	45
3.3.3 Source of Parameter and Form of Si Used	46
Chapter 4 Study of Lithium Diffusivity in Amorphous Silicon via Finite Element Analysis	
4.1 Introduction	
4.2 Model Development and Implementation	
4.3 Li Diffusivity in a-Si	
4.4 Results and Discussion	
4.4.1 Two-Phase Lithiation	
4.4.2 Single-Phase Lithiation	
4.4.3 Concentration Dependency of Diffusivity	
4.5 Conclusion	60
Chapter 5 Investigation of the Chemo-Mechanical Coupling in Lithiation of Amorphous	Si
through Simulations of Si Thin Films and Si Nanospheres	
5.1 Introduction	
5.2 Model Setup	64
5.3 FE Models and Simulation Conditions	
5.3.1 Amorphous Si Thin Film Model	65
5.3.2 Si Nanosphere Model	
5.4 Results and Discussion	
5.4.1 The Rate Behaviors	70
5.4.2 Electrode Geometry	
5.4.3 Chemo-Mechanical Coupling	
5.4.3.1 Thin Film	
5.4.3.2 Nanosphere	
5.4.4 Effect of Prior Process	
5.5 Conclusion	
Chapter 6 A Microstructure-Resolved Multiphysics Model for Li-ion Battery Si Anode	83
6.1 Introduction	
6.2 Model Description	
6.3 Model Parameters	
6.3.1 Chemical Potential	
6.3.2 Li Diffusivity in a-Si	
6.3.3 Electrolyte Properties	
6.3.4 Determine the Reaction Rate Constant and Apparent Transfer Coefficient	
6.4 Model Validation	
6.5 Cell Design with Si Nanowalls	
6.5.1 Design Parameter Study	
6.5.2 Concentration Polarization.	
6.5.3 Potential Evolution	97 07

6.5.4	Cell Capacity	101
6.6 Co	nclusion	
Chapter 7	Conclusion and Outlook	105
7.1 Co	nclusion and Contributions	105
7.1.1	Identify the Range of Li Diffusion for a-Si Anode	105
7.1.2	Identify the Chemical-Mechanical Two-Way Coupling Mechanism for Si u	ınder
Large I	Deformation Framework	105
7.1.3	Identify the Range of the Electrochemical Kinetic Parameters	106
7.1.4	A Design Tool for the Optimal Design of Battery Cells with a-Si Anode	106
7.2 Ou	tlook of Future Work	107
7.2.1	Interfacial Interplay between Si and Other Components	107
7.2.2	Thermal Management of Li-Ion Cell	107
7.2.3	Extension of Model to Other High Energy Density Electrode Material Li-Io	on Cell
		108
APPENDIC	ES	109
Appendix	AEffect of Li Transport Distance Change and Geometrical Constraint on	Different
Si Geome	etries	110
A. 1	Si Thin Film	110
A.2	Si Nanosphere	111
Appendix	A B Transport Phenomena in Si-Li Cells	114
Appendix	C Electrical Conductivity	118
Appendix	D Si-Current Collector Interaction	120
Appendix	E Stress State in Si Nanosphere	125
E.1	Si Nanosphere with Two Phase Lithiation	125
E.2	Si Nanosphere with Single Phase Lithiation	126
BIBLIOGR.	APHY	127

LIST OF TABLES

Table 1.1 Specific and areal capacities of Si nanostructures
Table 3.1 Parameters used in the MRM model
Table 3.2 Source of parameter used for Si
Table 4.1 Governing equations for Si model in Chapter 4 (Symbols are explained in Nomenclature)
Table 4.2 Literature data on Li diffusivity in Si
Table 4.3 Diffusivity study test cases
Table 4.4 Comparison of simulations with experimental results of two-phase lithiation 54
Table 5.1 Governing equations for Si model in Chapter 5 (Symbols are given in Nomenclature)
Table 5.2 Two conditions used in simulations
Table 5.3 The specific lithiation/delithiation capacity at 100C in respect of the capacity at 0.1C for the thin film and nanosphere under Conditions 1 and 2
Table 6.1 Governing equations for cell model in Chapter 6 (Symbols are in Nomenclature) 85
Table 6.2 Electrolyte systems used in chosen experiments
Table 6.3 Comparison of reaction rate constant, exchange current density and apparent transfer coefficient between literature and current work
Table 6.4 Model dimensions used in the Si nanowire model
Table 6.5 Model dimensions used in the Si thin film model
Table 6.6 Model dimensions used in the baseline model
Table 6.7 Half cells with SiNWs of different design parameters and the maximum SOC at 1C.96
Table 6.8 The influences of design parameters on c_2 polarization, ϕ_2 , η , ϕ_1 and SOC 100
Table 6.9 Comparison of the specific and volumetric capacity of half cell with SiNWs under 0.25C, 1C and 4C
Table 6.10 Comparison of the SOC and the capacity retention of half cell with SiNWs under 0.25C, 1C and 4C

Table B.1 Results in baseline test at t=130s (SOC=0.03)	116
Table D.1 Preliminary study on Si-Ni interface	123

LIST OF FIGURES

Figure 1.1 Comparison of energy density for various chemistries [3]
Figure 1.2 Inside a battery. Schematics are from referenced source[4–6] and self-drawn changes are made according to needs.
Figure 1.3 Gravimetric and volumetric capacities for pure metals as anodes for Li-ion batteries, in comparison with graphite [14].
Figure 1.4 In situ observation of a string of a-Si beads during lithiation [16]4
Figure 1.5 Capacity fading mechanism in Si system: (a) particle pulverization; (b) whole Si electrode morphology change and active material losing contact to current collector [18]
Figure 1.6 Nanostructured Si anodes: (a) 1000 nm a-Si film after 5 cycles [39]; (b) structure of c–Si nanocomposite [40] B1–B2, TEM images recorded at different magnifications. The black arrows point to spherical a-Si nanoparticles. (d) morphology evolution of an a-Si/CNF in the first two cycles [41]. Nanocracks nucleated during the second delithiation process (red dots); (d) cycling of an a-Si sphere [42]; (e) typical cross-sectional SEM image of hollow Si nanospheres at different magnifications E1-E2 [36]; (f) images of Si NWs after carbon coating F1-F2 [43] 6
Figure 1.7 Schematics of the modeling tasks with their relations
Figure 2.1 Summary of the first lithiation and subsequent cycling of a-Si and c-Si[42]
Figure 2.2 Stress history during cycling of a-Si thin film along X and Y direction in thin film plane [60].
Figure 2.3 Lithiation of c-Si nanoparticles showed in lithiated thickness changes vs. time plot of multiple nanoparticles[61].
Figure 2.4 Comparison of stress in a-Si thin film during lithiation and delithiation cycle and DFT calculation of yield stresses for Li _x Si[65]
Figure 2.5 (a) Inelastic deformation of Si during lithiation; (b) yield function Ψ defined in the space of deviatoric stress S_{ij} and driving force ζ from chemical potential[65]
Figure 2.6 Free energy diagram[80]. Diffusion process is influenced by (a) free energy differences between the ground state and product, and (b) activation energy
Figure 2.7 Experimental measurement and simulation prediction of variation of stress with time during cycles with a-Si thin film electrode[60]
Figure 2.8 Mechanical properties generally decreases with Li concentration (state of charge): (a) Young's modulus measured in in situ[102] and ex situ[103] experiments, and calculated in first

principle simulation[108]; (b) Poisson's Ratio calculated in first principle simulation[108]; and (c) yield stress calculated in first principle simulation[105]
Figure 2.9 Multiscale studies of Li-ion battery and their corresponding simulation technique[108–115]
Figure 3.1 A schematic presentation of the FE model, the governing equations and boundary conditions for a half cell with Si anode and Li reference electrode. (a) "Battery" sub-model, and (b) "stress" sub-model. The schematics were not drawn to scale
Figure 3.2 The ratio of c_1 to c as functions of volume ratio V/V_0
Figure 3.3 Verification of the mass correction coefficient with (a) a free expanding Si sphere and (b) a constrained thin film Si on a substrate, expanding only in the through thickness direction. (c) The mass rate ratio as a function of volume ratio V/V_0 . The results showed that the mass correction coefficient follows the relation of $m_c=V/V_0$. (d) The mass conservation was maintained for both thin film and sphere geometries
Figure 3.4 The stress-strain curve for (a) Cu substrate[157], and (b) stainless steel substrates[158]
Figure 3.5 Measurement of electronic conductivity in amorphous Si thin film held at various potentials between 350 and 0 mV where the Li-Si alloy phase form [107]
Figure 3.6 Mechanical properties of Li _x Si used: (a) elastic modulus, (b) Poisson's ratio, and (c) yield stress
Figure 4.1 Axisymmetric model for modeling lithiation of a-Si nanoparticle. (a) Experimental setup by McDowell et al.[30]; (b) two-phase lithiation in the first lithiation observed in experiment [30]; and (c) simulating two-phase lithiation of a-Si nanospheres using an axisymmetric 2D model. 48
Figure 4.2 Constant diffusivity was assigned separately for Li-rich and Li-poor phases with a small transition at around Li ₂ Si
Figure 4.3 Concentration profile comparison: (a) The image intensity during lithiation of the 570 nm diameter sphere during lithiation in experiments[42]. Red circles label the concentration Figure 4.3 (cont'd) drop at the reaction front. (b) Lithiation of Si in Tests 3 to 6 in simulations: concentration profile vs. distance to particle center
Figure 4.4 Lithiated thickness as a function of time during lithiation of a-Si spheres, including: (a) Two-phase lithiation comparison between results from experiments and simulations. Experimental curves (black) #1-#4 are from McDowell et al.[42] out of 26 nanospheres with unspecified diameter range. Simulation curves (red) are a-Si spheres of 400 nm and 570 nm. (b) Comparing lithiation speed between single-phase lithiation and two-phase lithiation

Figure 4.5 Simulations of lithiation of Si sphere of 570 nm diameter with a concentration dependent diffusivity. (a) Diffusivity functions; (b) Lithiated-thickness versus time, comparing to experimental data reported in Ref. [30] as shown in Fig. 4.4(a)
Figure 5.1 Asymmetric rate performance of 70nm a-Si thin film observed in experiment[173]. 66
Figure 5.2 Schematic illustration of the 2D model for a-Si thin film with boundary conditions (BCs), and the FE mesh. The schematic is not drawn to scale
Figure 5.3 Biaxial stress in thin film during cycling of a-Si thin film of 250 nm thickness under C/4 rate were plotted, (a) the stress history vs. SOC was compared with the experimental result was from Sethuraman et al.[60]. In simulations, the lithiation started with a residual stress from delithiation at the same rate; (b) the stress profiles inside the thin film showed that the stress distribution was almost uniform in the film during lithiation
Figure 5.4 (a) The anode with Si nanospheres encapsulated inside graphite shells[174] and (b) its capacity measured under various cycling rates, reproduced from Fig. S8 in Ref. [174]. (c) The FE model and its boundary conditions used in simulations
Figure 5.5 The predicted specific capacities vs. C rate for both 70nm a-Si thin film and a single a-Si nanosphere with (α =0.01) and without (α =0) the stress effect (a) thin film under Condition 1 (b) thin film under Condition 2; (c) nanosphere under Condition 1 and (d) nanosphere under Condition 2
Figure 5.6 Profiles of Li concentration, hydrostatic stress and Li flux vs. the distance to the bottom of the thin film at 100C under Condition 1. Solid line for without (α =0) and dash line for Figure 5.6 (cont'd) with the stress effect (α =0.01). (a) and (b) plot the Li concentration; (c) and (d) plot the hydrostatic stress; (e) and (f) plot the Li flux Nz . (a)(c)(e) are under 100C lithiation and (b)(d)(f) are under 100C delithiation
Figure 5.7 Profiles of Li concentration, hydrostatic stress and Li flux vs. the radial distance for the sphere at 100C under Condition 1. Solid line for without (α =0) and dash line for with the Figure 5.7 (cont'd) stress effect (α =0.01). (a) and (b) plot the Li concentration; (c) and (d) plot the hydrostatic stress; (e) and (f) plot the Li flux Nz . (a)(c)(e) are under 100C lithiation and (b)(d)(f) are under 100C delithiation.
Figure 5.8 Profiles of Li concentration and hydrostatic stress vs. the distance to the bottom of the thin film at 100C with α =0.01 under Condition 1 (dashed line) and Condition 2 (solid line). (a) and (b) are Li concentration; (c) and (d) are hydrostatic stress. (a) and (c) are under 100C lithiation; (b) and (d) under 100C delithiation.
Figure 6.1 (a) The relaxation potential of lithiated Si during lithiation and delithiation from Sethuraman et al.[118] and the OCP curve used in the current work. (b) The chemical potential derived from extrapolated OCP curve using Eq. 3.6
Figure 6.2 The ionic conductivity k_2 as a function of the salt concentration of LiPF ₆ in EC:DMC (2:1 vol.%)[131]

Figure 6.3 (a) The schematic of cell model with Si nanowire and (b) the mesh. (c) Comparisons of the cell voltage vs. SOC curves obtained by simulations with $k_0 = 8 \times 10^{-15}$ (m/s) (mol/m ³) ^{-0.7} , α_a =0.7 and α_c =0.3 (solid lines) and the experimental results (markers) by Zhang et al.[30] 92
Figure 6.4 Simulation of the experiment of the thin film a-Si electrode by Sethuraman et al. [60]. The FE model used was depicted in (a) and the mesh used in (b). The comparison between simulations and experiments were given for both (c) cell voltage and (d) biaxial stress vs. SOC during cycling at C/4 rate.
Figure 6.5 Schematic of the model used for the parameter study for Si half cell. Line ① and Point A are for the data analysis in later discussion
Figure 6.6 (a) The cell voltage changes with SOC at various test cases, and (b) the Li ⁺ concentration along the Si-electrolyte interface (line ① in Fig. 6.5) at the end of lithiation in each test case.
Figure 6.7 The evolution of potentials at point A for (a) the baseline test; (b) Thickness = 400 nm and (c) 3M LiPF ₆ electrolyte
Figure 6.8 The profiles of (a) electrolyte potential and (b) overpotential along line ① in Fig. 6.5 at SOC=0.03 for various test cases.
Figure 6.9 Si nanowalls of 200 nm thickness with various AR and SR in 1 M LiPF ₆ . (a) The specific capacity and (b) the volumetric capacity at 0.25C rate, (c)(d) at 1C, and (e)(f) at 4C 103
Figure A.1 Control elements at electrode surface in Si geometry (a) thin film and (b) sphere 110
Figure B.1 (a) Schematic of the model used for the parameter study for Si half cell. Line ① and Points A-C are for the data analysis in later discussion; (b)-(f) are profiles at the end of charging at 1C for the case of 200nm SiNWs, with SR=1, AR=15, in 1M LiPF ₆ in EC/DMC. The original sizes and shapes are shown in dark lines. (b) Li concentration in Si; (c) Li ⁺ in electrolyte; (d) the hydrostatic stress in Si and in current collector; (e) the magnitude of fluid velocity in the electrolyte.
Figure C.1 The investigation of electronic conductivity in Li-Si alloy by plotting the Si potential along ① in (a) at same time (t=150s) when (b) k_I =33 S/m; (c) k_I =0.33 S/m; (d) k_I =0.033 S/m.
Figure D.1Lithiation and delithiation of a-Si pillars on Ni substrate: (a) lithiation of pillars with diameter of 2100 nm and height of 2300nm; (b) delithiation of pillars with diameter of 2600 nm and height of 2300nm, in which crack is observed at Si surface near Si-Ni interface; (c) delithiation of pillar with diameter of 3150 nm and height of 2100nm, in which the crack propagates toward center of Si pillar[167]
Figure D.2Mechanical properties for the bulk Si and the interface region are modeled separately. (a) Young's Modulus as a function of concentration; (b) yield stress as a function of concentration.

Figure	E.1	Hydrostatic	stress	along	particle	radius	at	selected	times	during	(a)	two	phase
lithiatio	on, ai	nd (b) single	phase l	ithiatio	n								126

KEY TO ABBREVIATIONS

С	Li concentration in Si based on its initial volume, mol m ⁻³
c_+, c	Concentration of positive and negative ions in electrolyte, mol m ⁻³
c_1	Li concentration in Si based on its current volume, mol m ⁻³
c_2	Li ⁺ concentration in fluid electrolyte, mol m ⁻³
c_{theory}	Theoretical maximum Li concentration based on initial Si volume, mol m ⁻³
C	Elastic right Cauchy-Green deformation tensor
D_1	Li diffusivity in Li _x Si, m ² s ⁻¹
D_2	Li ⁺ diffusivity in fluid electrolyte, m ² s ⁻¹
D_{poor}	Li diffusivity in Li poor phase in first lithiation of Si, mol m ⁻³
D_{rich}	Li diffusivity in Li rich phase in first lithiation of Si, mol m ⁻³
E	Elastic Green-Lagrange strain tensor
f_{\pm}	Average molar activity coefficient
F	Faraday constant, 96485 C mol ⁻¹
F	Deformation gradient tensor
\mathbf{F}_{el}	Elastic deformation gradient tensor
\mathbf{F}_{inel}	Inelastic deformation gradient tensor
\mathbf{F}_{p}	Plastic deformation gradient tensor
\mathbf{F}_{c}	Li concentration induced deformation gradient tensor
i	Current density, A m ⁻²
$i_{1,2}$	Transfer current per unit of interfacial area at Si-electrolyte interface, A m
$i_{0,2}$	Transfer current per unit of interfacial area at Li-electrolyte interface, A m
i_{s_i} , i_{I_i}	Exchange current density at Si-electrolyte/Li-electrolyte interface, A m ⁻²

- I Identity matrix
- J Determinant of deformation gradient
- k_0 Reaction rate constant, (m s⁻¹) (mol m⁻³)^{- α a}
- K Electrical conductivity, S m⁻¹
- m_c Mass correction coefficient
- n Number of charges carried by Li⁺
- N_+, N_- Molar flux of positive and negative ions, mol m⁻²
 - R Gas constant, 8.314 J (K mol)⁻¹
 - S Second Piola-Kirchhoff stress tensor, Pa
- t_+, t_- Transport number of the positive and negative ions
 - T Temperature, K
 - **u** Displacement vector, m
 - U Open-circuit potential, V
- **v**_{fluid} Electrolyte fluid velocity, m s⁻¹
 - V Current volume of Si
- V_0 Initial volume of Si
- W_s Strain energy density, J m⁻³
- z_+, z_- Charge numbers of the positive and negative ions

Greek Alphabets

- α Stress effect coefficient
- $\alpha_a \alpha_c$ Apparent transfer coefficient
 - β Thermal expansion coefficient, K⁻¹
- $\beta(c_{eff})$ Mass expansion coefficient, m³ mol⁻¹

- δ_{ij} Kronecker delta
- ε_{ij}^{T} Thermal strain
- η Overpotential, V
- λ Stretch ratio
- Λ Lamé constant, $\Lambda = \nu E / ((1 + \nu)(1 2\nu))$, Pa
- μ_{fluid} Electrolyte viscosity, Pa s
- μ_{Li_xSi} Li chemical potential, J mol⁻¹
- μ_{Li} Li chemical potential the compound is in its standard state, J mol⁻¹
- $\mu_{Li}(\sigma)$ Li chemical potential including stress contribution, J mol⁻¹
 - M Lamé constant, $M = E/(2(1+\nu))$, Pa
 - σ Cauchy stress tensor, Pa
 - σ_h Hydrostatic stress, Pa
 - σ_i Principal stresses, subscript i = 1, 2, 3, Pa
- σ_{ii}^{ave} Averaged in-plane stress, subscript i = x, y, Pa
- σ_{VM} Von Mises stress, Pa
- σ_Y Yield stress, Pa
- ϕ Electrical potential, V
- Ω Partial molar volume of Li, m³ mol⁻¹

Subscripts and superscripts

- 1 Solid phase Si
- 2 Fluid electrolyte
- c Current collector
- surf Surface of Si

Chapter 1 Introduction

Secondary (also called rechargeable) batteries are the most convenient form of energy storage devices. Among all commercially available secondary batteries, lithium-ion (Li-ion) batteries offer the highest energy density, as shown in Fig. 1.1. The light weight and compact volume of Li-ion batteries has made them the primary choice in many consumer electronics, such as portable computers and cell phones. Nevertheless, current Li-ion battery technology is still far from satisfactory in meeting the power demands for electric or hybrid-electric vehicles (EV or HEV)[1,2]. To improve the range of EVs, the specific power and energy density of the batteries must be improved drastically.

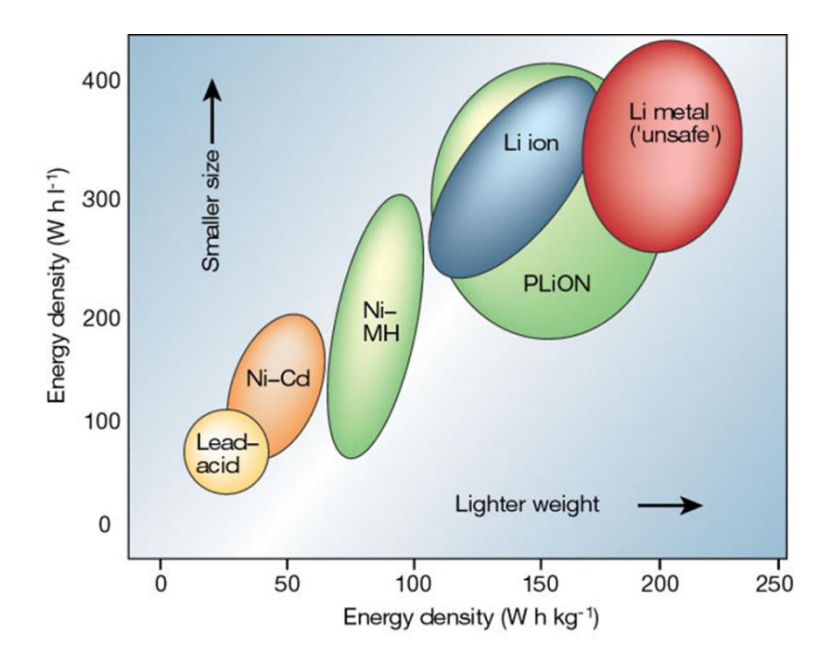


Figure 1.1 Comparison of energy density for various chemistries[3]

1.1 Lithium-Ion Battery

A typical Li-ion battery can be in the form of a coin cell, a cylindrical cell, a prismatic cell, or a pouch cell. It is usually composed of multiple basic cells, stacking together, as shown schematically in Fig. 1.2.

A basic Li-ion battery cell consists of two electrodes, namely cathode and anode, two current collectors and a separator. The electrodes in commercial cells consist of active materials, binder and additives. The binder holds active electrode materials together and attaches them to current collector. Carbon blacks are common additives used to improve the electrical conduction of the electrode. The separator is a porous thin film which provides the electrical insulation between the cathode and anode while allows ionic conduction. Fluid electrolyte fills the battery cell, providing Li⁺ pathway in between electrodes.

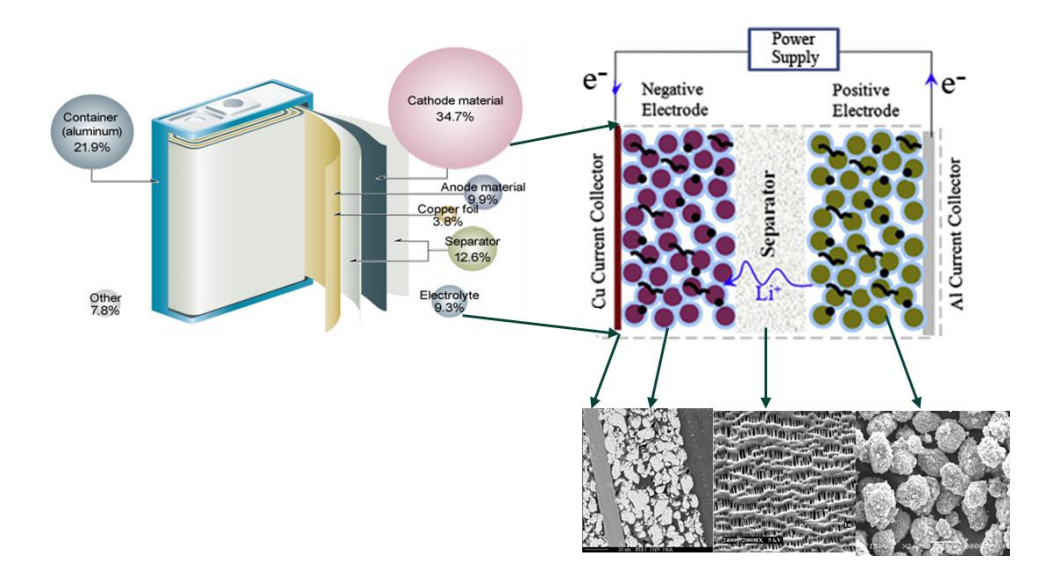


Figure 1.2 Inside a battery. Schematics are from referenced source[4–6] and self-drawn changes are made according to needs.

Li-ion batteries are closed systems where the electrical energy is provided by the active electrodes via redox reactions. For example, for a cell with LiCoO₂ as cathode material and graphite as anode, the charge and discharge processes are as follows:

Discharge

Anode: $\text{Li}_{x}\text{C}_{6} \rightarrow 6\text{C} + x\text{Li}^{+} + xe^{-}$

Cathode: $\text{Li}_{1-y}\text{CoO}_2 + y\text{Li}^+ + y\text{e}^- \rightarrow \text{LiCoO}_2$

Charge

Anode: $6C + xLi^+ + xe^- \rightarrow Li_xC_6$

Cathode: $\text{LiCoO}_2 \rightarrow \text{Li}_{1-y}\text{CoO}_2 + y\text{Li}^+ + y\text{e}^-$

1.2 Si Anode

The energy density of a battery is measured by the specific gravimetric energy (mAh/g) and specific volumetric energy (mAh/cm³). These are determined by the total Li-ion storage capacity of the cell divided by the total mass or volume of all components, including the non-active materials such as the current collectors, separator, binder and additives, etc.

A very lucrative way to increase the specific energy density of Li-ion batteries is to replace the graphite, the anode material employed since the first commercial Li-ion battery was introduced in 1991, with high capacity materials. Graphite has a gravimetric capacity of 372 mAh/g and a volumetric capacity of 843 mAh/cm³. A number of materials offer a much higher Li storage capacity[7–9], as shown in Fig. 1.3. Among all Li storage materials, silicon (Si) is the most promising[10,11]. Si has a theoretical gravimetric capacity of 3579 mAh/g and volumetric capacity of 8339 mAh/cm³, ten times of that of graphite[12–14].

3

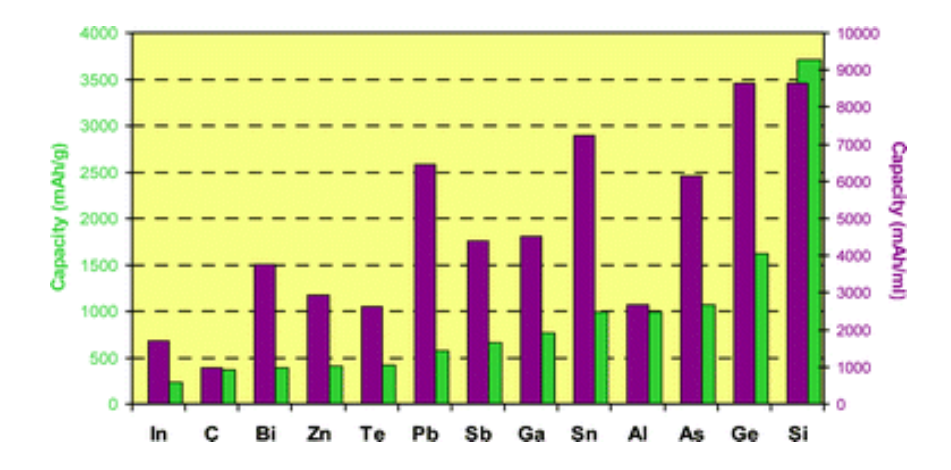


Figure 1.3 Gravimetric and volumetric capacities for pure metals as anodes for Li-ion batteries, in comparison with graphite [14].

However, the major obstacle in the use of large capacity anode materials like Si in Li-ion batteries is the large volume variation accompanied with lithiation and delithiation cycles. Fig. 1.4 presents the dramatic volume expansion of a string of amorphous Si beads during lithiation. It is reported that when Si is in fully lithiated state, the volume of the particle expands to about 400% of its original size (300% volume change)[15,16].

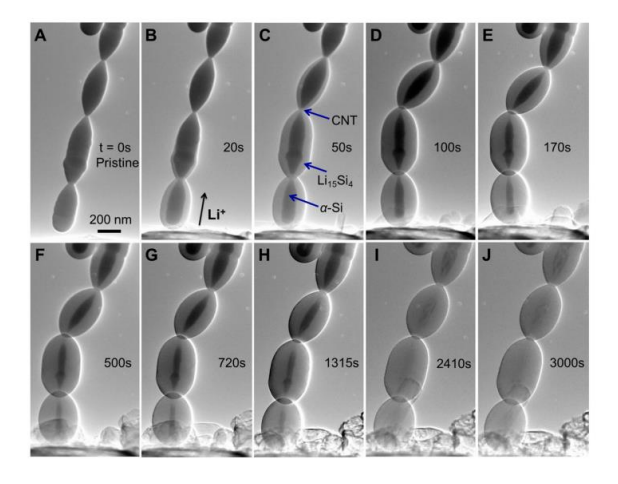


Figure 1.4 In situ observation of a string of a-Si beads during lithiation[16].

The large volume variation can induce high stresses inside the active materials. Li moves inside the host material through diffusion. The Li concentration gradient results in a non-uniform volume variation in the material, which induces the so-called diffusion induced stresses (DIS), similar to that induced by a temperature gradient. The large diffusion induced stress can cause fracture and even pulverize the Si particles. Moreover, the large volume variation of the active particles also strains the binder, which provides the electrical connectivity throughout the electrode. The capacity loss due to binder or binder/particle interface failure is common in electrodes with high capacity active particles. The above problems, as shown in Fig. 1.5, have been attributed to the short cycle life[10,11,17] and rapid capacity fading observed in Li-ion batteries with Si anode.

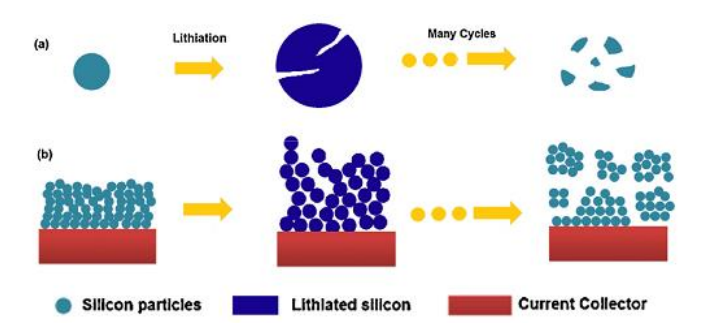


Figure 1.5 Capacity fading mechanism in Si system: (a) particle pulverization; (b) whole Si electrode morphology change and active material losing contact to current collector[18].

Numerous strategies have been proposed to mitigate the problems related to the large volume variation in Si. Reducing the size of the active materials has been proven to be an effective way to reduce the stress[10,11]. Nanostructured Si anodes also reduce the tendency of crack formation. The size dependent fracture behavior has been explained from the viewpoint of

fracture mechanics[18–21]. In a smaller structure, the stress-relief volume accompanying crack growth is not significant enough to overcome the surface energy penalty associated with the crack growth and hence a smaller size offers a greater resistance to crack initiation and propagation[18]. This has led to the use of various nano-sized Si including Si nanoparticles[22,23] and their composites[10,11,24,25], ultrathin Si films[26–29], Si nanowires[30,31], Si whiskers[32], Si coated carbon nanofiber (CNF)[33,34], Si coated metal fiber[35], Si hollow spheres[36], nanostructured porous Si[37], Si NWs on CNF film[38] etc. Fig. 1.6 presents some typical nanostructured Si anodes reported in literature. Table 1.1 summarizes the state-of-the-art performance of various nanostructured Si anodes. As shown, their cycle lives are generally low. The nanostructured Si anodes have improved the capacity retention from less than 10 cycles[10,11] to 40~100 cycles or more, but they still fall short to meet the target of 3000 cycles for EV or HEV applications.

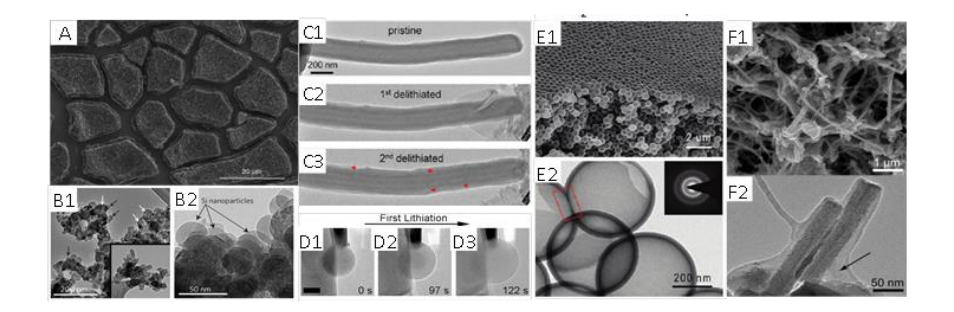


Figure 1.6 Nanostructured Si anodes: (a) 1000 nm a-Si film after 5 cycles[39]; (b) structure of c—Si nanocomposite[40] B1–B2, TEM images recorded at different magnifications. The black arrows point to spherical a-Si nanoparticles. (d) morphology evolution of an a-Si/CNF in the first two cycles[41]. Nanocracks nucleated during the second delithiation process (red dots); (d) cycling of an a-Si sphere[42]; (e) typical cross-sectional SEM image of hollow Si nanospheres at different magnifications E1-E2[36]; (f) images of Si NWs after carbon coating F1-F2[43].

Table 1.1 Specific and areal capacities of Si nanostructures.

Geometry	Specific capacity (mAh/g) Initial/after # cycles	Area capacity mAh/cm ²	Loading mg/cm ²	comment
Baseline graphite	370	1.48*	4	-
Si film of 50nm[28]	3500/3500 (2C, 200 cycles)	0.087*	0.039755*	-
Si Nanowire on CNF[38]	1800/1500 (C/10, 40 cycles)	-	3.6	collector free
C-Si core-shell tube[33]	2000/1600 (C/5, 55 cycles)	4	2.4	-
a-Si on CNF[34]	1500/1000 (100 cycles)	-	-	-
Cu-Si NW array[35]	883/839* (C/10, 40 cycles)	0.16	0.19	-
Si Nano Particles[22,23]	2500/1400 (600 cycles) 2200/2200 (C/10, 30 cycles)	0.42 3.3	0.3*	conductive binder
Si Hollow sphere[36]	2725/1500 (C/2, 700 cycles)	-	0.56~0.76*	-
3D Porous Si Particles[37]	2840/2800 (C/5, 100 cycles)	-	-	-

^{*}Estimated value

The large volume variation of the Si anode also presents a great challenge in the dimensional control of the battery. The volume change of the anode and cathode is opposite in sign during a battery cycle. The dimensional variation of the Si anodes is an order higher than the common cathode materials. How to make a dimensional stable Li-ion battery with Si anode is still an open question.

Si in Li-ion batteries presents tremendous technical challenges far beyond the boundary of electrochemistry. The physical phenomena in a Li-ion battery include the species and charge transports in electrodes and electrolyte, reaction at the electrochemical interface, heat generation and heat transfer, and stresses and deformations caused by lithiation, thermal and mechanical loads. These phenomena are coupled. To improve the design a system with such complexity, computer simulations would be an imperative tool. As it is now, computational models for LIBs with high capacity battery electrodes are still in its infancy.

1.3 Scope of the Work

The objective of this work is to develop a computation model for Li-ion battery cell with a-Si anode. This model will be used for design optimization of Si anode and battery cell performance. Towards this end, a microstructure-resolved multiphysics (MRM) model is required.

In the previous work, such model has been developed for Li_xC₆/Li_PF₆/Li_yMn₂O₄ cell as shown in the center panel of Fig. 1.7. To implement the model for Li-ion batteries with a-Si anode, there are a number of challenges. In the proposed work, we will focus on the following two aspects: (1) the lack of the key material properties of lithiated silicon (Li_xSi); and (2) the chemical-mechanical coupling relationship between Li diffusion and stress. These problems will be investigated through systematically conducted numerical simulations and correlations of numerical simulations with experiments, as illustrated in Fig. 1.7. The outline of the thesis is given in following section 1.4.

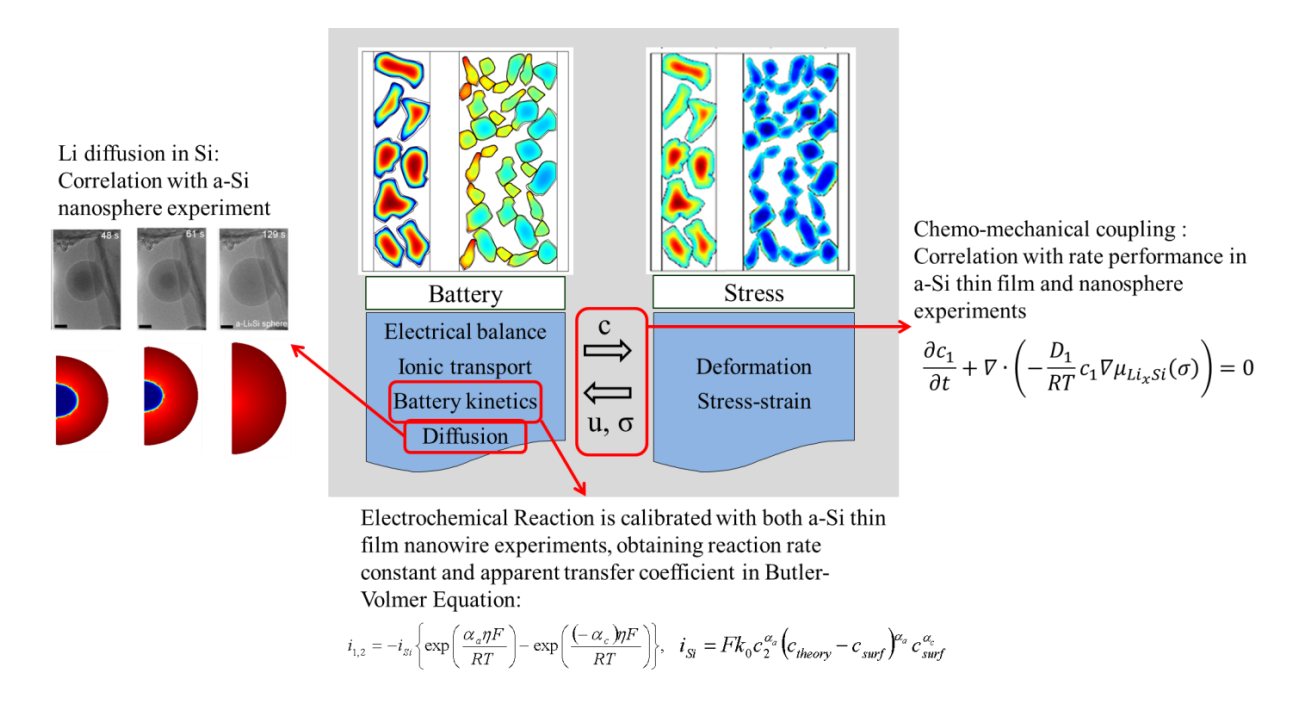


Figure 1.7 Schematics of the modeling tasks with their relations.

1.4 Outline of the Dissertation

This thesis is organized as follows.

Chapter 1 introduces the problem and defines the scope of work.

Chapter 2 provides a literature review on current understanding about Si anode, including the lithiation/delithiation process, the dimensional changes during lithiation, the theories on chemomechanical coupling, and the mechanical properties of Si and lithiated Si.

Chapter 3 provides a detailed description of the Multiphysics and their couplings considered in the MRM model, including the electrochemical kinetics, mass transport, charge balance, the Li intercalation induced strain, the mechanical strain, and the stresses in the active particles and other battery components.

The lack of key material properties for Si/Li_xSi, especially the Li diffusivity in Si, has prevented the efficient use of MRM numerical tools in the design of lithium-ion batteries with Si anodes. Therefore, in Chapter 4, a finite element (FE) analysis is used to study the Li diffusivity in a-Si anodes.

Chapter 5 investigates the chemo-mechanical coupling of a-Si through numerical simulations of the rate behavior of two geometries (thin film and sphere). An asymmetric rate behavior has been observed in thin film a-Si anode but not in a-Si anode of other shapes. The results show that the geometry, the constraint of the electrode, the chemo-mechanical coupling, and the prior process influence the rate behavior.

Chapter 6 presents an MRM model for a half cell with a-Si anode. The model is used in a parameter study for LIB with Si nanowalls. The influences of the size and the length/size ratio of the Si nanowalls, the spacing in between, and electrolyte Li⁺ concentration on the specific and volumetric capacities of the cell are investigated.

Final conclusions, contributions and proposed future work are presented in Chapter 7.

Chapter 2 Literature Review

This chapter provides a literature review on the current understandings, the problems and the research development relevant to simulating Si in Li-ion batteries with MRM model.

2.1 Lithiation of Silicon

2.1.1 Two-Phase and Single-Phase Lithiation

Si can assume one of the three phases at room temperature: amorphous Si (a-Si), monocrystalline Si (c-Si) and polycrystalline Si. In Li-ion battery applications, a-Si and c-Si are commonly used.

During the first lithiation, a-Si exhibits isotropic swelling whereas c-Si suffers anisotropic swelling[44,45]. The shape and volume changes are reversible for a-Si but not for c-Si. Moreover, the phase transformation is observed during the first lithiation. The equilibrium Li-Si phase diagram[46] shows that, when reacting with Li, c-Si goes through a series of phase changes at high temperature. In Li-ion batteries at room temperature, the phase changes were not observed. It has been proven that upon lithiation, both c-Si and a-Si transform to metastable amorphous Si-Li alloys (a-Li_xSi). Anodes made of c-Si quickly become disordered. This phenomenon was referred to as electrochemically-driven solid-state amorphization (ESA)[47]. Towards the fully lithiated stage, a-Li_xSi crystallizes to either Li₁₅Si₄ (Li_{3.75}Si) or Li₂₂Si₅ (Li_{4.4}Si)[34]. Crystalline Si eventually transformed into a-Si after the first cycle[48].

To understand the lithiation mechanism and stress evolution of Si anodes, the morphology evolutions of various Si nanostructures have been investigated experimentally inside the transmission electron microscopes (TEM) with ongoing electrochemical reactions[41,42,49–53]. TEM images revealed a sharp phase boundary instead of a diffused band between the reactant (c-Si) and the product (a-Li_xSi), indicating that the first lithiation occurs via a two-phase

mechanism[42]. The sharp phase boundary is called reaction front. It was observed experimentally and confirmed by the first principle simulation that a group of Li atoms collectively weaken the Si-Si covalent bonding near the edge of {111} atomic facets at the reaction front first and caused easy break of other Si-Si bonds after to form Li_xSi[54]. This result has important consequences for mechanical stress evolution during lithiation[41,42]. The sharp phase boundary between the c-Si core and a-Li_xSi shell coupled with anisotropic swelling has been related to crack formation in c-Si NWs[51].

The two-phase phenomenon was also observed in the TEM images of a-Si anodes at the first lithiation[42]. Since a-Si network is continuous random, the Si-Si bond breaking by Li atom is isotropic[54]. The phase front was not visible in the delithiation and second lithiation as long as Li_xSi did not crystallize into Li_{3.75}Si at the end of lithiation[42,50], the so-called single-phase lithiation. The lithiation of both c-Si and a-Si is shown in Fig. 2.1. Si anodes with an initial amorphous structure have shown to improve the cycle life over crystalline Si[26–28]. Therefore, this work will focus on study a-Si structure in Li-ion battery.

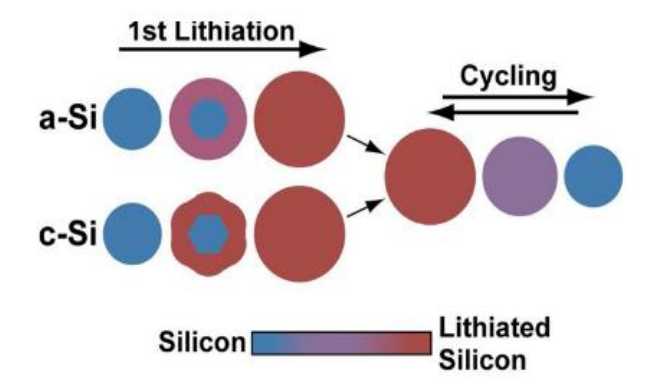


Figure 2.1 Summary of the first lithiation and subsequent cycling of a-Si and c-Si[42].

2.1.2 Lithiation Induced Volume Expansion

As mentioned earlier, Si experiences volume change about 300% when it is fully lithiated. To simulate this process, the finite deformation theory[55,56] is invoked to consider the large deformation. In experimental observation reviewed in 2.1.1, the lithiation in a-Si always introduces isotropic volume expansion and its reversible, while the c-Si experiences anisotropic volume expansion in its first lithiation and this process is not reversible. Since we are only interested in the a-Si structure in this study, the finite deformation theory for isotropic expansion[57,58] will be discussed.

Freestanding Si geometries, such as nanospheres and nanowires, do not experience constraint imposed by other battery components. Therefore, the Si particle undergoes free expansion. The total deformation includes elastic deformation, plastic deformation and lithiation induced deformation [57].

To describe the behavior of solids with large deformation, such as elastomers, the stretch ratio instead of strain is often used. This treatment has also been used for Si anode[57,58]. The stretch ratio is defined as[55,59]

$$\lambda = \frac{\text{length in current state}}{\text{length in reference state}} = \frac{l}{L}$$
 (2.1)

The volume change induced by elastic deformation $V_{\scriptscriptstyle e}/V_{\scriptscriptstyle 0}$ is

$$\frac{V_e}{V_0} = \lambda_1^e \lambda_2^e \lambda_3^e \tag{2.2}$$

where the subscripts 1, 2, 3 correspond to the three material directions; the subscript/superscript e donates the change induced by elastic deformation.

Plastic deformation is volume preserving [56], therefore,

$$\frac{V_p}{V_0} = \lambda_1^p \lambda_2^p \lambda_3^p = 1 \tag{2.3}$$

where subscript/superscript p donates the change induced by plastic deformation

The lithiation induced volume change V_{Li}/V_0 is proportional to the change in the Li concentration[57,58],

$$\frac{V_{Li}}{V_0} = 1 + \Omega \Delta c \tag{2.4}$$

where Ω is the partial molar volume of Li, which defines the volume increase due to one mole of Li guest atom insertion in the Si host material, and Δc is the lithium concentration increment.

Since the deformation is isotropic in a-Si, the lithiation induced stretches λ_1^{Li} , λ_2^{Li} and λ_3^{Li} along all directions are assumed to be equal in the stress-free Si network

$$\frac{V_{Li}}{V_0} = 1 + \Omega \Delta c = \lambda_1^{Li} \lambda_2^{Li} \lambda_3^{Li} \stackrel{\text{isotropic}}{=} \left(\lambda^{Li}\right)^3$$
(2.5)

The total volume change should be

$$\frac{V}{V_0} = \left(\lambda_1^e \lambda_2^e \lambda_3^e \right) \left(\lambda_1^p \lambda_2^p \lambda_3^p \right) \left(\lambda^{Li}\right)^3 \tag{2.6}$$

2.2 Chemical-Mechanical Two Way Coupling

2.2.1 Experimental Observations

Lithium insertion can induce high stresses in the host material. The stress accumulation during electrochemical lithiation and delithiation has been measured in situ for a-Si thin film [60], as shown in Fig. 2.2. The measurement was based on the Stoney equation which determined the stress in a thin film on a thick substrate by measuring its curvature using a Multi-beam Optical Sensor (MOS) system [60]. In literature, this is the only method to measure the in situ stress in Si electrode.

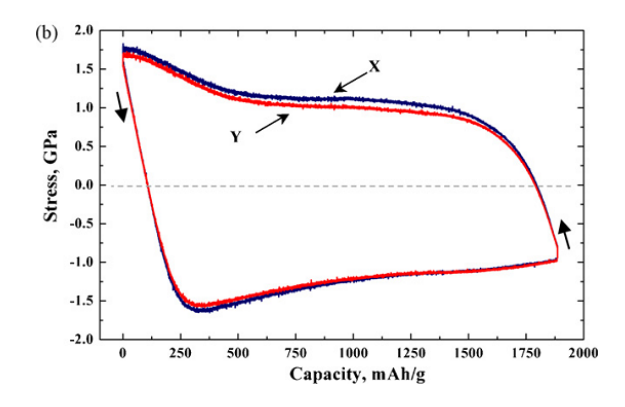


Figure 2.2 Stress history during cycling of a-Si thin film along X and Y direction in thin film plane [60].

The Li diffusion process is also influenced by stress. This has been observed in lithiation process of c-Si nanospheres [61,62]. As shown in Fig. 2.3, the lithiated thickness (thickness of Li_xSi shell) growth rate reduced after the Si has been lithiated for some time. It was observed that the sharp interface between c-Si and a- Li_xSi could not proceed towards nanospheres center as fast as the beginning of lithiation [61]. The lithiation in small and large particles slowed on a similar time scale. c-Si cores remained in the smaller particles even after much thicker regions have been lithiated in larger particles. This indicated that the slowing of the reaction was not due to diffusion limitation [61,62]. The phenomenon was attributed to the high compressive stress at the reaction front that eventually prohibited Li further from insertion [61].

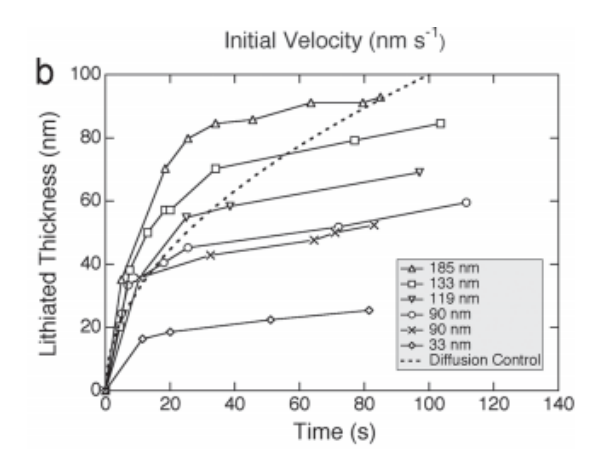


Figure 2.3 Lithiation of c-Si nanoparticles showed in lithiated thickness changes vs. time plot of multiple nanoparticles[61].

2.2.2 Theories for Diffusion Induced Stress

The stress associated with the lithiation process is diffusion induced stress (DIS). It arises inside Si due to compositional inhomogeneity during ion insertion and removal processes, similar to the stresses caused by non-homogenous expansion in a solid particle subjected to a non-uniform temperature field. Accompanied by lithiation, both elastic and inelastic stresses could be generated. The elastic stress was generally calculated using Hooke's Law[63]. The plastic stress may be calculated by considering the process as plastic[64] and viscoplastic[63]. Recent studies showed that stress generated inside Li_xSi in experiment is much lower than yield strength calculated in first principle simulated based on density functional theory (DFT) for Li_xSi[65], as shown in Fig. 2.4. Therefore, purely mechanical plasticity/viscoplasticity consideration may not be enough to capture the lithiation-induced stress because that the lithiation process is driven by both chemical potential of Li and by the stress (hydrostatic and non-hydrostatic stresses) generated during Li insertion[65], as shown in Fig. 2.5(a).

Subsequently, a chemo-mechanical yield function based on chemical potential and deviatoric stress was defined, as shown in Fig. 2.5(b)[65].

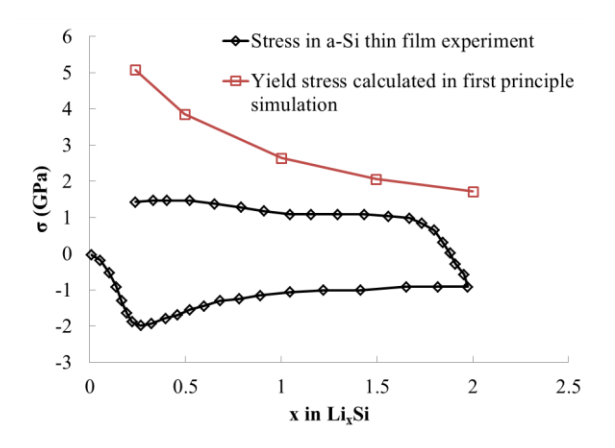


Figure 2.4 Comparison of stress in a-Si thin film during lithiation and delithiation cycle and DFT calculation of yield stresses for $Li_xSi[65]$.

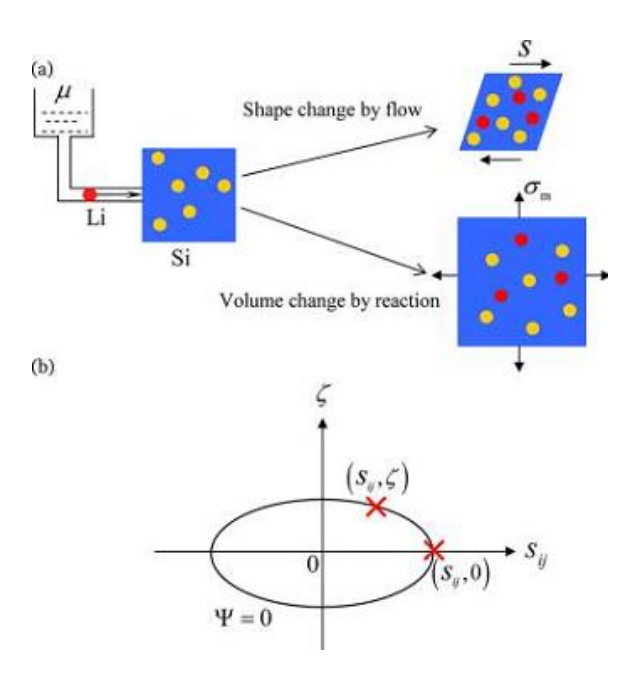


Figure 2.5 (a) Inelastic deformation of Si during lithiation; (b) yield function Ψ defined in the space of deviatoric stress S_{ij} and driving force ζ from chemical potential[65].

Furthermore, the experimentally measured ultimate tensile strengths for Si/Li_xSi[66] was also much lower than the yield stresses calculated[65]. The ultimate tensile strength measured in a nanowire with initial diameter of 130 nm[66] was 3.6GPa for pure c-Si and 0.72GPa for Li_{3.75}Si, which were in a similar range with the yield stresses measured in the thin film experiment[60,65]. This confirms that the yield strength predicted in DFT simulation was indeed higher than the real yield strength.

The abovementioned theories[63,65,67] were proposed based on the observation of experimentally measured stress from a-Si thin film electrode under lithiation[63,65].

2.2.3 Theories for Stress Influenced Li Diffusion

The Li diffusion influences the stresses generated inside Si, and vice versa.

Fick's laws are usually adopted when considering the diffusion problem in ideal mixture [68]:

$$\frac{\partial c}{\partial t} + \nabla \cdot \mathbf{J} = 0 \tag{2.7}$$

where J is the Li flux.

However, in solid-state diffusion problems, the Fick's laws in Eq. 2.11 and 2.12 do not always hold because the local flux considered through Fick's first law may be influenced by other factors, such as stress[63,64,69,70] and temperature[71,72]. Since the heat generation inside Si during lithiation is not considered at this stage, we focus on the stress effect on diffusion of Li in Si. Even without externally applied stresses, such as freestanding silicon, the diffusion induced stress may affect the lithiation of Si. So the general Fick's laws using chemical potential as the driving force are used to consider the non-Fickian behavior introduced by stress[73]:

$$\frac{\partial c}{\partial t} = -\nabla \cdot \mathbf{J} = -\nabla \cdot \left(-\frac{D}{RT} c \nabla \mu \right) \tag{2.8}$$

where R is gas constant, with a value at 8.314 $J/(\text{mol} \cdot K)$; T is temperature; μ is chemical potential; D is Li diffusivity in Si.

In literature, two theories have been proposed for the diffusion of guest atoms into a host material under the stress effect related to the free energy diagram in Fig. 2.6: (a) Diffusivity is modulated by the stress induced activation energy barrier shift[69,74,75]. The rate of reaction depends on a free energy between the ground state and transition state (i.e. activation energy). (b) The chemical potential of Li in Si changes because the free energy difference between substrate and product is altered by stress[63,64,76–79]. This free energy difference is the driving force for reaction. Therefore, both effects should be considered for Li diffusion in stress Si.

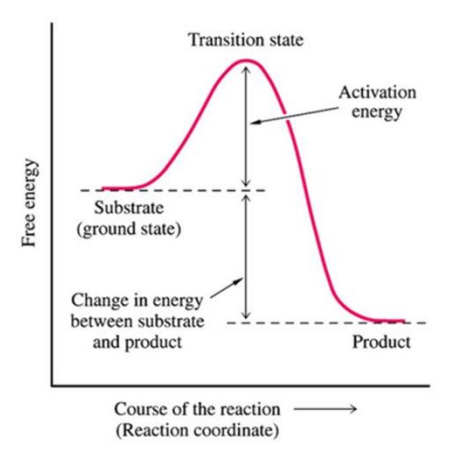


Figure 2.6 Free energy diagram[80]. Diffusion process is influenced by (a) free energy differences between the ground state and product, and (b) activation energy.

2.2.3.1 Stress Effect on Li Diffusivity

Stress is found to influence the diffusivity through the activation energy. The activation energy is stress dependent[81]. The Arrhenius equation has been used to calculate the diffusivity with the consideration of the changes on activation energy by stress[69,74,75]:

$$D = D_0 \exp\left(\frac{-E_A + \kappa \Omega \sigma}{RT}\right) = D_0^{Li} \exp\left(\frac{\kappa \Omega \sigma}{RT}\right)$$
 (2.9)

where $D_0^{Li}=D_0\exp\left(\frac{-E_A}{RT}\right)$ is the diffusivity of Li in Si under zero stress; E_A is the activation energy barrier; Ω is the partial molar volume of Li in Si; σ is the hydrostatic stress[69,74,75,82] calculated by $\frac{\sigma_1+\sigma_2+\sigma_3}{3}$, which involves only pure tension or compression; κ is a positive dimensionless constant.

Theories proposed had been used to study both freestanding electrode geometry [69,74] and constrained thin film electrode [75,82] in Li-ion battery. However, since the lack of experiments and theoretical studies, the only validation was made through results comparison with atomistic model [82]. Moreover, the determination of κ is still an open question.

2.2.3.2 Stress Effect on Li Chemical Potential

The chemical potential change during lithiation is still argumentative given multiple different treatments in literature. One of the treatments is to consider the system as an ideal solid solution under hydrostatic stress only[57,64,82–84]. The chemical potential can be written as

$$\mu = \mu_0 + RT \ln C - \sigma_h \Omega = \mu_{SF}^{Li} - \sigma_h \Omega$$
 (2.10)

where μ_{SF}^{Li} is the chemical potential of Li atoms in Li-Si alloy under zero stress; Ω is the Li partial molar volume and σ_h is the hydrostatic stress. The assumption is that Li in lithiated Si could be viewed as a mobile component in a stressed solid. This could be reasoned based on MD

simulation showing that Li mobility is 3-4 orders higher than Si mobility in Li_xSi[85]. Therefore, this equation considers the solid solution as homogeneous and the only stress applied here is hydrostatic. Up to now, Eq. 2.15 was only used for qualitative analysis of the stress effect on diffusion process[57,64,82–84].

Another treatment involved an expression of the chemical potential in multicomponent solid under non-hydrostatic stress to reach equilibrium. This was originally developed by Larché and Cahn[86–88] and was used to study solid-state diffusion problem in geology[89] and metallurgy[90].

It was recently adopted to consider Li diffusion in Li-ion battery electrode[60,63,91] in the form of:

$$\mu = \mu_{SF}^{Li} - \frac{\Omega_{Si}\eta}{3}\sigma_{kk} - \frac{\Omega_{Si}B_{ijkl}}{2}\sigma_{ij}\sigma_{ij}$$
(2.11)

where Ω_{Si} is the molar volume of silicon, η is the rate of volumetric strain change due to lithiation and $B_{ijkl} = ds_{ijkl}/dc$ where s_{ijkl} is the elastic compliance tensor. It was used for a-Si thin film electrode[63,92] in the form of:

$$\mu = \mu_{SF}^{Li} - \frac{2\Omega_{Si}\Omega_{Li}}{3(1 + \Omega_{Li}c)}\sigma - \Omega_{Si}\sigma^2 \frac{\partial}{\partial c} \left(\frac{1}{M}\right)$$
(2.12)

where $\sigma = \sigma_{yy} = \sigma_{zz}$ is the Cauchy stress in a-Si thin film and M is the biaxial modulus. Eq. 2.12 was used to predict the stress effect on Li diffusion in Si thin film and is validated with in situ stress-strain curve [60], as shown in Fig. 2.7.

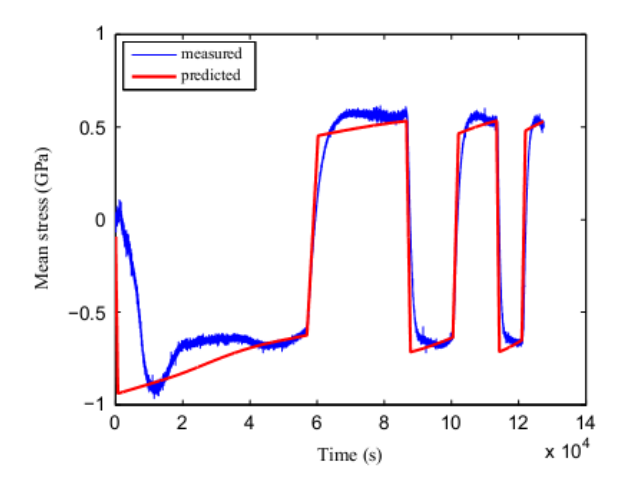


Figure 2.7 Experimental measurement and simulation prediction of variation of stress with time during cycles with a-Si thin film electrode[60]

Since Larché and Cahn theory was developed based on the small strain framework under an elastic field, whether it is valid under finite deformation and yield of Si or not remains unclear. Recent theories were developed to consider driving force change under finite deformation framework[77–79]. These theories are yet to be validated.

Moreover, the stress free term of chemical potential (first term) in Eq. 2.12 was also based on dilute solution in Larché and Cahn theory. The chemical potential in Li_xSi concentrated solution must be determined through correlation of experiments [63,93].

2.3 Material Property Variations during Si Lithiation

The structural change in Si during lithiation results in changes in the material properties, including those important to the performance and durability of the anode such as the Li diffusivity and the mechanical properties. One of the major obstacles in the modeling of Si anode is the uncertainty in these material properties. The reported ranges for the key material properties are reviewed as follows.

2.3.1 Li Diffusivity in Si

The Li diffusivity in Si is a key parameter determining the lithiation time and Li concentration gradient, the latter in turns influences the intercalation stresses. The literature data on Li diffusivity in Si varies over a wide range [63,85,94–99].

2.3.2 Electrochemical Kinetics with Si Anode

The electrochemical reaction at the Si-electrolyte interface is determined by the Butler-Volmer equation. Without knowing the reaction parameters, such as the reaction rate constant and the apparent transfer coefficient, the electrochemical reactions happen in cell with Si anode could not be correctly studied.

2.3.3 Mechanical Properties

Mechanical properties involves here are Young's modulus, Poisson's ratio and yield strength of Si/Li_xSi. The evolution of the above properties along with lithiation has been studied through experiments[100–104] and the first principle simulations[85,105–107].

The Young's modulus of the a-Si is 94 GPa. The c-Si has a modulus of 130-185 GPa depending on crystallographic directions. The Young's modulus of Li_xSi as a function of Li fraction has been investigated using ex situ[103,104] and in situ[100–102] experimental methods. The Young's modulus of the Li_xSi phase was reported to decrease with increasing Li concentration, as shown in Fig. 2.8(a). The reported Young's modulus decreased from 95 GPa for a-Si to 10 GPa for Li_{3,75}Si[102].

The first principle simulations[85,105–107] have been used to calculate the mechanical properties of the Li_xSi phase. The stress-strain response of the a- Li_xSi has been calculated[105]. The elastic modulus, Poisson's ratio and yield stress were found to decrease with Li concentration, as shown in Fig. 2.8.

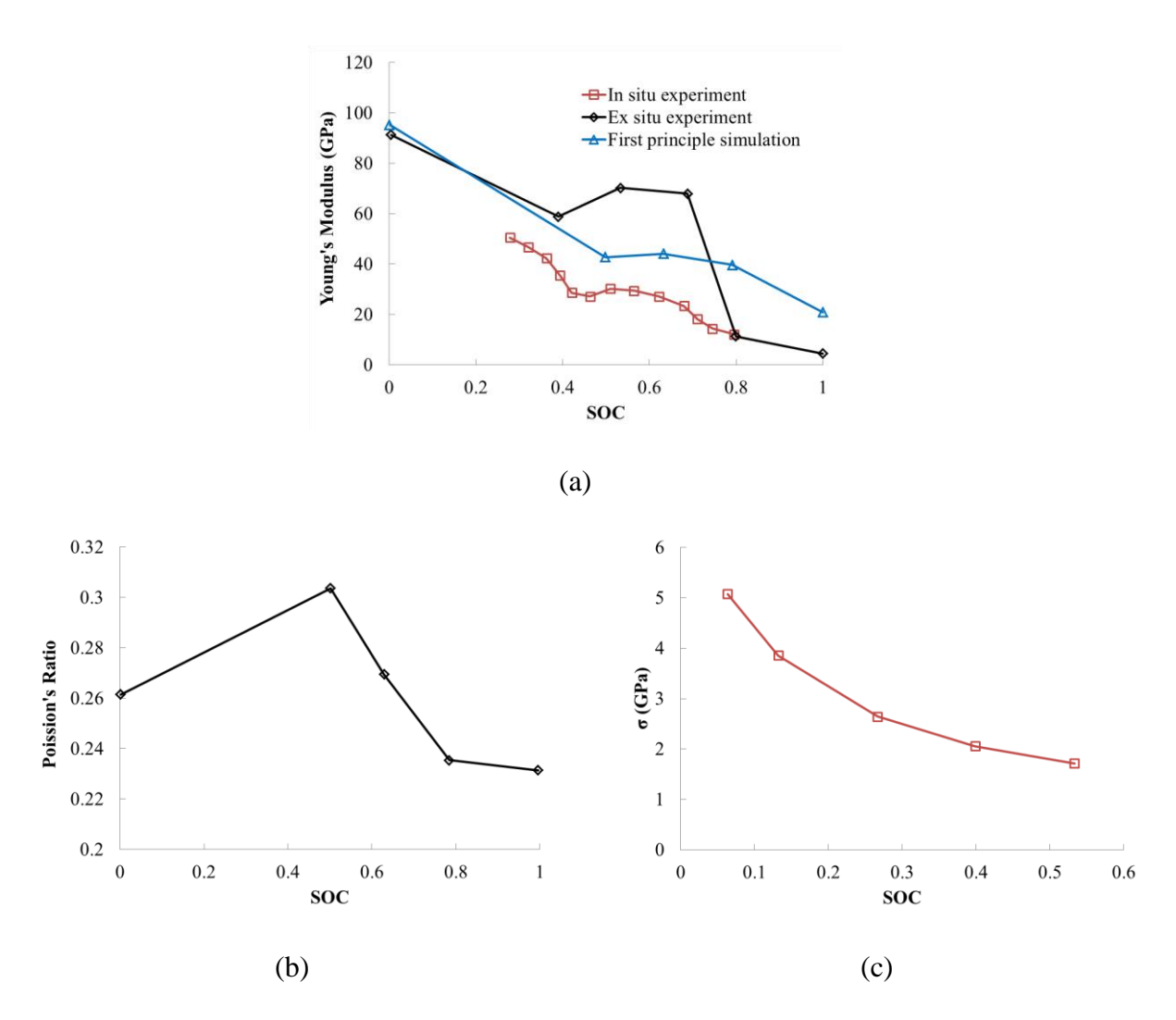


Figure 2.8 Mechanical properties generally decreases with Li concentration (state of charge): (a) Young's modulus measured in in situ[102] and ex situ[103] experiments, and calculated in first principle simulation[108]; (b) Poisson's Ratio calculated in first principle simulation[108]; and (c) yield stress calculated in first principle simulation[105].

2.4 Simulation of Si Particles and Li-Ion Cells

It always involves multiple scales in modeling the Li-ion batteries. As shown in Fig. 2.9, the scale of modeling tools in literature ranges from microscopic level to macroscopic level depending on the problems and system studied.

Given the focus of this work, two levels are reviewed: modeling of Si particle and Li-ion cells models.

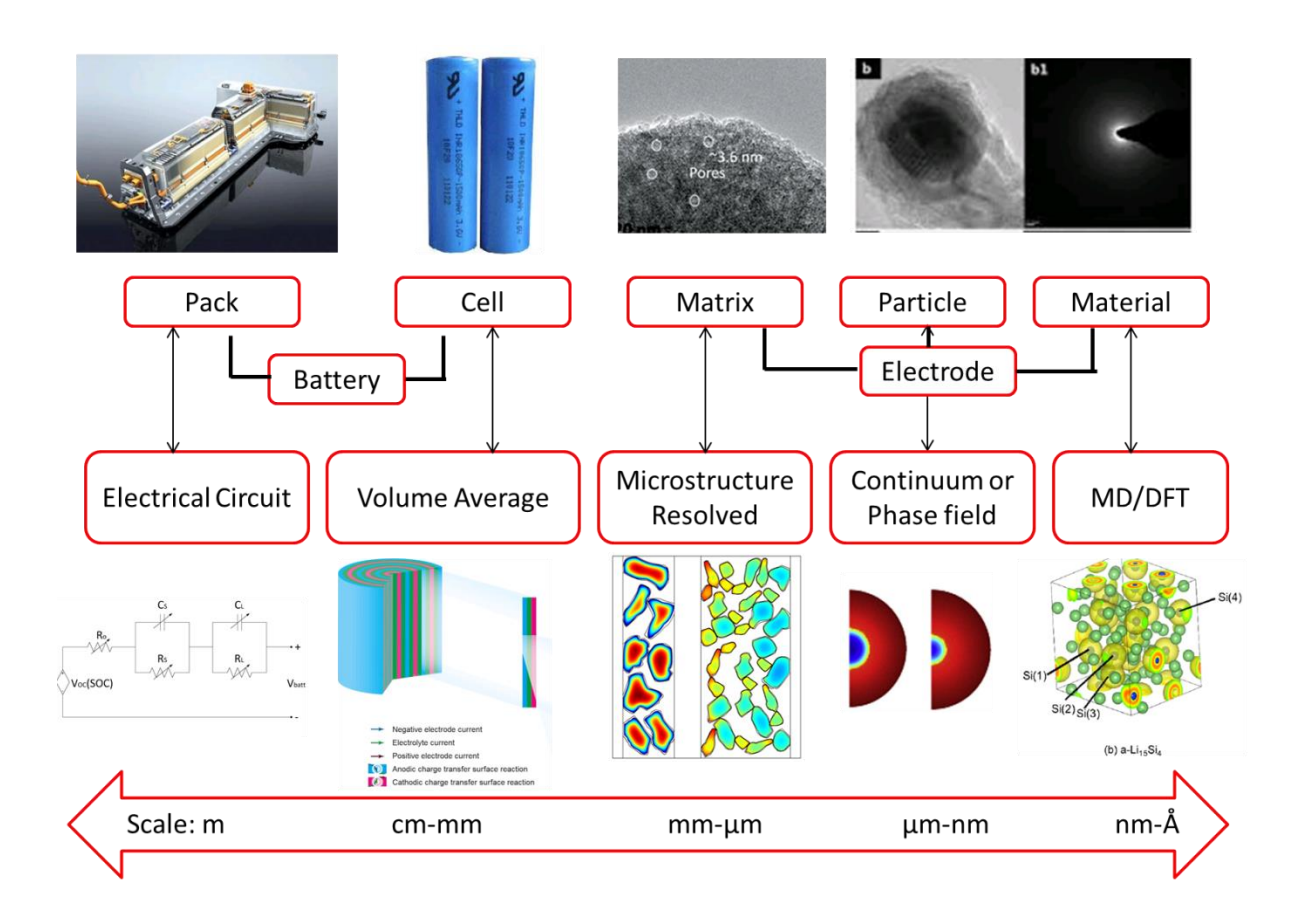


Figure 2.9 Multiscale studies of Li-ion battery and their corresponding simulation technique[108–115].

2.4.1 Si Anode

In literature, there are some works investigated the deformation and stress in single Si particles using analytical[53,116–121] or numerical models[51,63,100,103,105,122–127] by the coupled diffusion-stress approach.

The analytical analysis was done on Si with various forms, like nanowires[53,116], thin film[118,121] and spheres[58]. For example, diffusion-induced stress with[116] or without[105] consideration of the change in mechanical properties based on either small deformation theory[116,119,120] or large deformation theory[105]. The analytical studies guided the further continuum modeling of Si using FEA codes like COMSOL and ABAQUS.

The continuum modeling of Si on multiple problems were investigated, usually involves one of the following topics: the anisotropic growth of crystalline Si[51]; the crack propagation in Si[123]; the interaction with other cell components like binder[124], and current collector[128]; the chemo-mechanical coupling relationship[64,127,129]; the electrochemistry involved in cell with Si anode in 1D[63] and in 3D[128]. The questions that interest researcher the most were targeted and resolved, respectively.

2.4.2 Li-Ion Cell

To simulate and predict performance of the Li-ion battery cell, multiple works has been published on graphite system since 1993. Doyle et al. first developed the Li|polymer|composite cathode cell[130] and further to polymer Li_xC₆|Li_yMn₂O₄ cell[131] in 1D, considering the mass/charge transport and the electrochemical reactions inside the cell. This model was further developed to a 3D model with porous cathode matrix was constructed by Wang and Sastry[132]. By considering the porous structural of cathode, they investigated the influence of particle size on cell performance. The model demonstrates that the microstructure-resolved model was a good design tool for prediction of electrochemical cell performance.

Furthermore, the basic electrochemical cell was further developed to incorporate physics other than pure electrochemistry, including: (1) the coupled thermal-electrochemical model[133–135], which was used to understand the temperature influence on cell potential and predict the

heat generation under various cell design; (2) the coupled electrochemical-stress model[136,137], which was used to predict the structural changes inside the cell during operation, and the DIS generated in electrode and the stresses in other cell components due to the change in electrode.

Si as the emerging potential high energy density anode material to Li-ion cell and thus many simulation works has been done for Si as in Section 2.4.1. However, rarely any cell model was developed for Li-ion cell with Si. In 2011, Chandrasekaran and Fuller[138] developed a 1D electrochemical cell model with silicon composite electrode in reference to Li counter electrode. Effective parameters were used to take account of the electrode porosity. They showed that porosity of the electrode vary a great deal during cycling and may severely affect the battery performance. This work demonstrated the importance of the model of the cell with Si anode and posed the requirement of development of the MRM model.

2.4.3 Modeling of Li Transport

The prediction of Li transport in Li-ion cell is one of the most important parts in simulation the Li-ion cell. The Li/Li⁺ transport inside the Li-ion cell models should be considered for both electrode and the electrolyte. Here is how they are considered in literature.

The Li⁺ transport in electrolyte solution is determined by the electrochemical potential difference between the two electrodes, which in turns depends on the conditions such as solution composition and the electrical state, etc. Li⁺ transport in electrolyte is often described by the Nernst-Planck equation[131,132,138,139]. The electrochemical reaction is considered as happening at the electrode-electrolyte interface, where Li⁺+e⁻=Li. Li then transports further into the electrode. The electrochemical potential includes both the chemical potential and the electric potential. In the solid-state electrode, the driving force for Li transport is commonly considered through concentration gradient[130–132,138] or chemical potential gradient[63,128,140]. With

the assumption of neutral charge of Li, the electric potential contribution is not considered in the solid-state electrode.

This work follows the same assumptions as stated above.

Chapter 3 Microstructural-Resolved Multiphysics Model for Li-ion Battery

The model framework of the MRM model for Si anode in Li-ion battery is introduced in this chapter. The model is composed of two sub-models: a "battery" sub-model and a "stress" sub-model. The "battery" computes electrochemical kinetics, mass transport, and charge balance. The "stress" sub-model computes the Li intercalation induced strain, the mechanical strain, and the stresses in the active particles and other battery components. The two sub-models share the same FE mesh and are coupled through Li concentration field and deformation/stress field.

Most of the available experiments for Si anodes are in a half cell configuration with Li metal as the reference electrode. Therefore, the model was developed for Li_xSi|fluid electrolyte|Li cell. It includes the current collector, the Si anode, the fluid electrolyte, and the Li metal counter electrode. Fig. 3.1(a) and (b) present the schematics of the half cell model with the governing equations and boundary conditions for the "battery" and "stress" sub-models, respectively. The details of each sub-model are listed in the following sections.

No flux and electric insulation

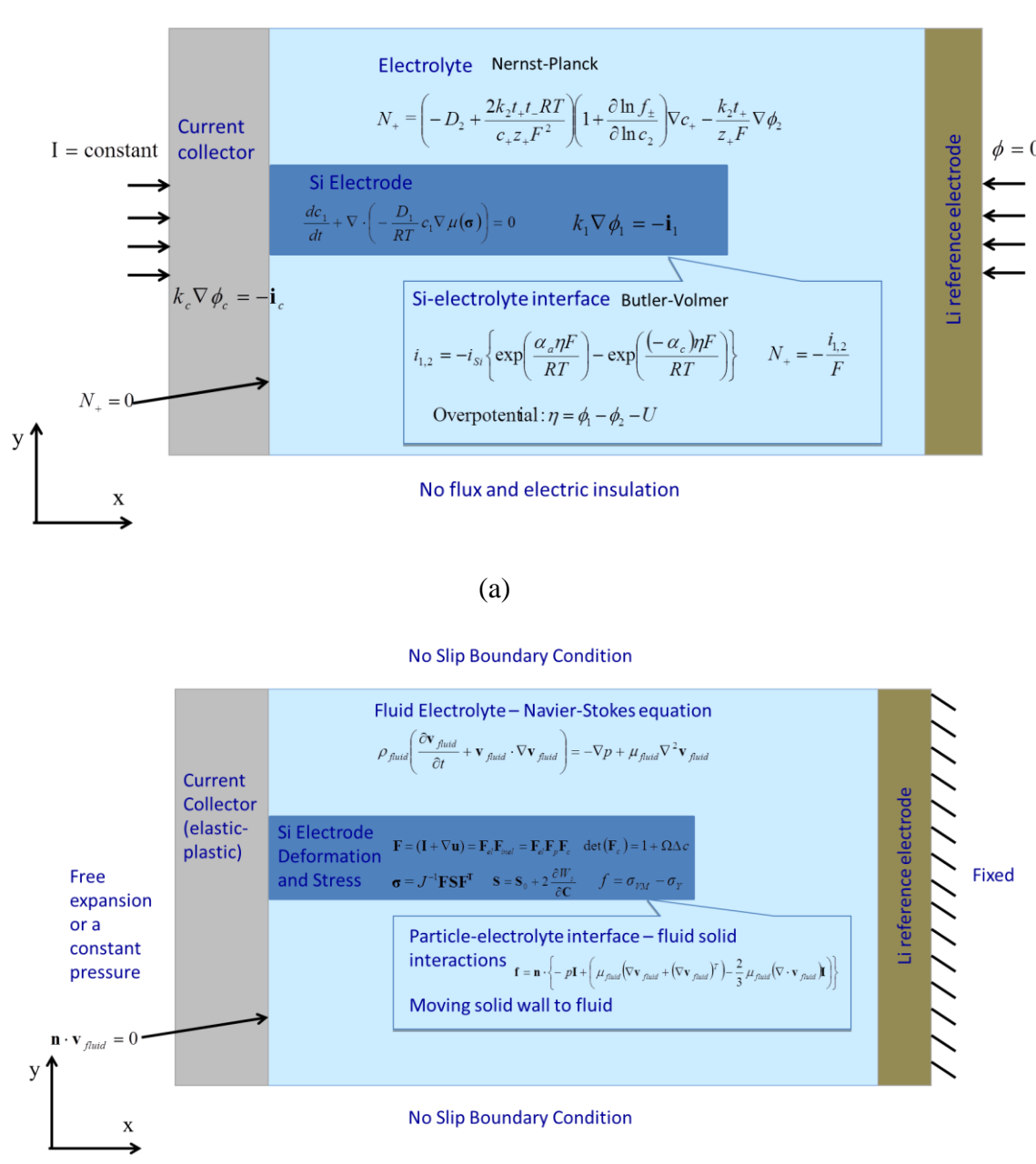


Figure 3.1 A schematic presentation of the FE model, the governing equations and boundary conditions for a half cell with Si anode and Li reference electrode. (a) "Battery" sub-model, and (b) "stress" sub-model. The schematics were not drawn to scale.

(b)

3.1 "Battery" Sub-Model

In "battery" sub-model, the mass transport, charge balance and electrochemical reaction kinetics are considered.

3.1.1 Mass Transport

The mass transport includes the Li transport in Si anode and the electrolyte.

The Li transport in Si is considered through either Fick's second law in Eq. 3.1 with concentration gradient as lithiation driving force

$$\frac{\partial c_1}{\partial t} + \nabla \cdot (-D\nabla c_1) = 0 \tag{3.1}$$

or considered through general form diffusion equation in Eq. 3.2 with the chemical potential gradient as driving force[141,142]

$$\frac{\partial c_1}{\partial t} + \nabla \cdot \left(-\frac{D_1}{RT} c_1 \nabla \mu_{Li_x Si}(\mathbf{\sigma}) \right) = 0 \tag{3.2}$$

where c_1 is Li concentration in Si, D is the apparent Li diffusivity and D_1 is the chemical diffusivity of Li in Li_xSi, $\mu_{Li_xSi}(\sigma)$ is the chemical potential of Li_xSi under stress influence, R is gas constant, and T is the temperature.

The chemical potential under stress $\mu_{Li_xSi}(\sigma)$ is defined as [141,142]

$$\mu_{Li_{x}Si}(\boldsymbol{\sigma}) = \mu_{Li_{x}Si} + \Delta\mu_{Li_{x}Si}(\boldsymbol{\sigma})$$
(3.3)

where μ_{Li_xSi} is the chemical potential in Li_xSi under zero stress, $\Delta\mu_{Li_xSi}(\sigma)$ is the change in chemical potential due to stress.

 μ_{Li_xSi} in Eq. 3.3 can be mathematically determined under various assumptions, such as the ideal solution assumption[57,83,138,143,144], where the driving force for Li-Si mixing is the entropy with zero enthalpy so that it allows components miscibility in all proportions; the regular solution assumption[145–147], which includes both the entropic and enthalpic contributions to

Li-Si mixing; and the non-ideal solid solution assumption[63,82,148,149], where Li occupies the interstitial or substitutional lattice sites with a saturation limit in the host material. Moreover, it could be extrapolated from the experimental measurement of the open circuit potential.

Depending on the different focuses and needs in each study presented in this work, various theories for Li diffusion in Si is adopted in Chapter 4-6.

For example, when investigating the range of Li diffusivity in Chapter 4, the Eq. 3.1 is used with a simplification of constant *D* neglecting the contribution from stress.

When studying the chemo-mechanical coupling relationship in Chapter 5, as the focus was on the stress effect on Si lithiation rather than Li-Si mixing theories, as the first step, the ideal solution assumption was adopted[57,83,150]. Therefore, Eq. 3.3 became

$$\mu_{Li_xSi}(\mathbf{\sigma}) = \mu_{Li_xSi}^0 + RT \ln \chi_{Li} + \Delta \mu_{Li_xSi}(\mathbf{\sigma})$$
 (3.4)

where χ_{Li} is the mole fraction of Li in Li_xSi, and $\mu_{Li_xSi}^0$ is a constant corresponding to the chemical potential of Li in Si at its standard state. The value of $\mu_{Li_xSi}^0$ is unknown. Since the interests here are the change of chemical potential $\mu_{Li_xSi}(\sigma) - \mu_{Li}^0$, and the gradient $\nabla \mu_{Li_xSi}(\sigma)$, the exact value of $\mu_{Li_xSi}^0$ is not needed.

For $\Delta \mu_{Li_xSi}(\sigma)$, as the first step, a simple form of chemo-mechanical coupling relationship was adopted based on [57,83,150]

$$\Delta\mu_{Li_{x}Si}(\mathbf{\sigma}) = \alpha \Omega \sigma_{h} \tag{3.5}$$

where σ_h is the hydrostatic stress, i.e., the average of principal stresses $\sigma_h = (\sigma_1 + \sigma_2 + \sigma_3)/3$; α is the coefficient for the influence of hydrostatic stress on chemical potential; Ω is the partial molar volume of Li defining the volume change due to one mole of guest atom insertion into the host material. For Li in Si, $\Omega = 9 \times 10^{-6} \, \text{m}^3/\text{mol}[151]$.

When the MRM model was used to investigate the cell performance in Chapter 6, μ_{Li_xSi} in Eq. 3.3 is then mathematically determined by fitting the open-circuit potential (OCP) U using Eq. 3.6[152,153]. Thus, the change of Li composition is related to chemical potential and, in turns, to the cell potential

$$\mu_{Li_xSi} - \mu_{Li} = -nFU \tag{3.6}$$

where μ_{Li} is the chemical potential of the Li metal, which is set as μ_{Li} =0; n is the number of charge Li⁺ carries, which equals to 1; F is the Faraday constant, and F=96485 C/mol.

To describe the Li⁺ diffusion and charge balance in the electrolyte, Nernst-Planck equations based on the concentrated solution theory[139] are adopted. As an initial step, the influence of convective flow on Li⁺ transport in the fluid electrolyte is not considered. The fluxes of the binary ionic species are described by[130]

$$N_{+} = \left(-D_{2} + \frac{2k_{2}t_{+}t_{-}RT}{c_{+}z_{+}F^{2}}\right)\left(1 + \frac{\partial \ln f_{\pm}}{\partial \ln c_{2}}\right)\nabla c_{+} - \frac{k_{2}t_{+}}{z_{+}F}\nabla\phi_{2}$$
(3.7)

$$N_{-} = \left(-D_{2} + \frac{2k_{2}t_{-}^{2}RT}{c_{-}z_{-}F^{2}}\right)\left(1 + \frac{\partial \ln f_{\pm}}{\partial \ln c_{2}}\right)\nabla c_{-} - \frac{k_{2}t_{-}}{z_{-}F}\nabla\phi_{2}$$
(3.8)

where N_+ and N_- are the positive and negative ion molar fluxes; t_+ and t_- are the transport numbers of the positive and negative ions; z_+ and z_- are the charge numbers of the positive and negative ions; c_+ and c_- are the positive and negative ion concentrations; c_2 is the Li⁺ concentration in electrolyte; D_2 is the Li⁺ diffusivity in electrolyte; k_2 is the ionic conductivity; f_\pm is the average molar activity coefficient; ϕ_2 is the electrical potential of the electrolyte.

The electrolyte current density can be expressed as [130]

$$\mathbf{i}_{2} = -k_{2} \nabla \phi_{2} + \frac{2RTk_{2}}{c_{2}F} \left(1 + \frac{\partial \ln f_{\pm}}{\partial \ln c_{2}} \right) (1 - t_{\pm}) \nabla c_{2}$$
(3.9)

3.1.2 Electron Transport

The electron transport in the cell is considered in the Si electrode and current collector through Ohm's law. In Si electrode, the current \mathbf{i}_1 is calculated as

$$k_1 \nabla \phi_1 = -\mathbf{i}_1 \tag{3.10}$$

where k_1 is the electrical conductivity of Si, $\nabla \phi_1$ is the electrical potential, and \mathbf{i}_1 is the current density in Si.

Similarly, the electron transport inside the current collector is calculated as

$$k_c \nabla \phi_c = -\mathbf{i}_c \tag{3.11}$$

where k_c is the electrical conductivity of the current collector; and \mathbf{i}_c is the current density inside the current collector.

The relationship between \mathbf{i}_1 and \mathbf{i}_2 at the Si-electrolyte interface is

$$\mathbf{i}_1 = -\mathbf{i}_2 \tag{3.12}$$

3.1.3 Electrochemical Kinetics

The electrochemical reactions occurring in the cell are:

Si electrode:
$$xLi^+ + Si + xe^- = Li_xSi$$
, $(0 \le x \le 3.75)$ (3.13)

Li electrode:
$$Li^+ + e^- = Li$$
 (3.14)

The electrochemical reaction is considered though the Butler-Volmer equation [130,138], which describes the relationship among the reaction kinetics, lithium concentration, and electrical potential at the electrochemical interface

Si side:
$$i_{1,2} = -i_{Si} \left\{ \exp\left(\frac{\alpha_a \eta F}{RT}\right) - \exp\left(\frac{(-\alpha_c)\eta F}{RT}\right) \right\}$$
 (3.15)

Li side:
$$i_{0,2} = -i_{Li} \left\{ \exp\left(\frac{\alpha_a \left(-\phi_2\right)F}{RT}\right) - \exp\left(\frac{\alpha_c \phi_2 F}{RT}\right) \right\}$$
 (3.16)

where $i_{1,2}$ and $i_{0,2}$ are the transfer current density at the Si-electrolyte and Li-electrolyte interface, respectively; η is the surface overpotential; and α_a and α_c are the negative and positive charge transfer coefficients, respectively. For LIBs, since n=1, $\alpha_a=1-\alpha_c$ [139]. $i_{Li}=12.6$ A/m² is the exchange current density at Li-electrolyte interface; i_{Si} is the exchange current density at the Si-electrolyte interface

$$i_{Si} = Fk_0 c_2^{\alpha_a} \left(c_{theory} - c_{surf} \right)^{\alpha_a} c_{surf}^{\alpha_c}$$
(3.17)

In Eq. 3.17, k_0 is the reaction rate constant; c_2 is the Li⁺ concentration in the electrolyte; c_{theory} is the theoretical maximum Li concentration in Si, and c_{surf} is the Li concentration at Si surface. Both c_{surf} and c_{theory} are in reference volume V₀ to represent the Li_xSi composition in Butler-Volmer equation [139].

The overpotential η in Eq. 3.15 is defined as

$$\eta = \phi_1 - \phi_2 - U \tag{3.18}$$

where ϕ_1 and ϕ_2 are the local electrical potential of Si and electrolyte, respectively. The overpotential in Eq. 3.16 is reduced to $-\phi_2$ because the potential of Li is kept as 0V, and the OCP of Li is also 0V [138,139].

The Li⁺ mass flux N_+ into the Si is related to $i_{1,2}$ such that

$$N_{+} = -i_{1,2} / F \tag{3.19}$$

3.1.4 Boundary Conditions

Fig. 3.1(a) presents the boundary conditions for the "battery" sub-model, which corresponds to the conditions experienced by a basic cell. Because the charged mobile species in the electrolyte cannot diffuse into the current collectors or beyond the upper and lower boundaries, and there is no Li flux between Si and the current collector. At these boundaries, the flux of Li and the charged mobile species was set as

$$N_{\perp} = N_{-} = 0$$
 (3.20)

A zero potential is assigned for the Li reference electrode and a constant current is applied to the current collector at Si electrode side. As the electrons do not enter the electrolyte, all boundaries and interfaces of the electrolyte are treated as electrically insulated. The interfacial resistance is not considered at the Si-current collector interface at this time.

3.2 "Stress" Sub-Model

3.2.1 Deformation of Si

To model the large deformation of Si electrode, the finite deformation theory[31], also called finite strain theory, is used. Similar approaches have been used for lithiation of Si in other works[57,58,63,67,76,77,79]. The deformation of a-Si anode during battery cycling includes the deformation due to mechanical constraint and those induced by Li concentration and temperature variations[133,136,154]. At this stage, the heat generation and the thermal effect are not considered and hence the thermal deformation is neglected.

The deformation gradient \mathbf{F} can be calculated as [77]

$$\mathbf{F} = (\mathbf{I} + \nabla \mathbf{u}_{solid}) \tag{3.21}$$

where I is the identity matrix, u_{solid} is the displacement vector.

The deformation gradient is composed of an elastic deformation gradient \mathbf{F}_{el} and an inelastic deformation gradient \mathbf{F}_{inel} . In a Si anode, the inelastic deformation includes the plastic deformation gradient \mathbf{F}_p and the Li concentration induced deformation gradient \mathbf{F}_c such that [57,67]

$$\mathbf{F} = \mathbf{F}_{el}\mathbf{F}_{inel} = \mathbf{F}_{el}\mathbf{F}_{p}\mathbf{F}_{c} \tag{3.22}$$

Li insertion causes Si anode to increase its volume. The ratio of the current volume V to the initial volume V_0 is proportional to the change in Li concentration[79]. In a stress-free Si network

$$\frac{V}{V_0} = \det(\mathbf{F}_c) = 1 + \Omega \Delta c \tag{3.23}$$

where Δc is the Li concentration increment calculated by using the initial volume V_0 .

To describe the large deformation, the stretch ratio λ instead of strain is often used. It is defined as [55,59]

$$\lambda = \frac{\text{length in current state}}{\text{length in reference state}} = \frac{l}{L}$$
 (3.24)

For a-Si, the deformation is isotropic. The lithiation induced stretches λ_1 , λ_2 and λ_3 , therefore, are assumed to be equal[79]

$$\det(\mathbf{F}_c) = 1 + \Omega \Delta c = \lambda_1 \lambda_2 \lambda_3 = \lambda^3$$
 (3.25)

The lithiation induced deformation is determined through the deformation gradient as

$$F_{c,ij} = \sqrt[3]{1 + \Omega \Delta c} \delta_{ij} \tag{3.26}$$

where δ_{ij} is the Kronecker delta.

3.2.2 Coupling between Li Transport inside Si and Volume Expansion

The volume expansion of a-Si during lithiation was computed in COMSOL FSI module through the thermal-mass diffusion analogy. The thermal strain is calculated as

$$\varepsilon_{ij}^T = \beta \Delta T \delta_{ij} \tag{3.27}$$

where ΔT is the temperature increment, which is equivalent to the effective concentration increment Δc_{eff} ; β is the thermal expansion coefficient. Comparing Eq. 3.27 to Eq. 3.26, the mass expansion coefficient for the analogy is derived as

$$\beta(c_1) = \frac{\sqrt[3]{1 + \Omega \Delta c} - 1}{\Delta c_1}$$
(3.28)

where c_1 is the effective Li concentration calculated based on the current Li_xSi volume V. It should be noted that c_1 differs from the Li concentration c calculated with the unlithiated Si volume V_0 , $c_1/c = V_0/V$, as discussed in Ref. [155]. Therefore, SOC is determined by

$$SOC = \frac{cV_0}{c_{theory}V_0} = \frac{c_1V}{c_{theory}V_0}$$
(3.29)

where c_{theory} is the value corresponding to V_0 , which is 3.11×10^5 mol/m³[138]. The relationship between c and c_1 is shown in Fig. 3.2.

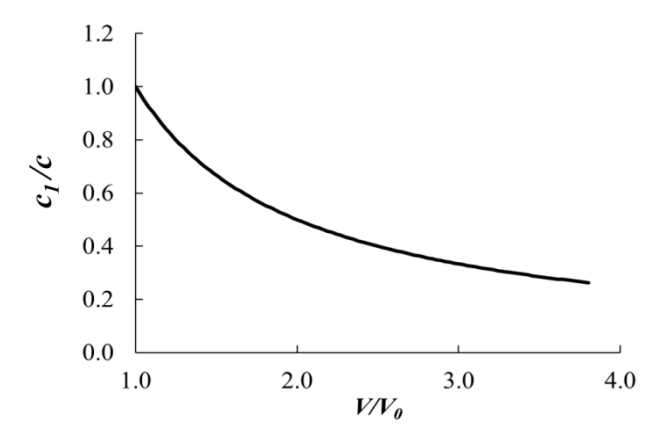


Figure 3.2 The ratio of c_1 to c as functions of volume ratio V/V_0 .

In this work, the Li diffusion equation was formulated in PDE module in the spatial coordinate system. The large deformation of Li_xSi was considered in FSI module in the material coordinate system. In simulations, the Li transport was bi-directionally coupled with Li_xSi large deformation through the Thermal Expansion node within FSI module (i.e. through the time derivative of the Li concentration that depends on the deformation). However, the mass conservation was not automatically satisfied[156]. In simulations in spatial coordinates, the Li flux applied at the Si boundary does not account for its dependency on the deformation. As a result, a constant flux would result in an increase in the total number of Li entering the Si host if the surface area increases. To account for this effect, a mass correction coefficient m_c was introduced at the boundary with Li source such that $m_c = V/V_0$ [155].

The mass conservation in the coupled analysis was examined using two electrodes, a sphere (Fig. 3.3(a)) and a thin film on a substrate (Fig. 3.3(b)). The simulations were carried first using $m_c = 1$, i.e. without the correction. Fig. 3.3(c) plots the mass rate ratio between the mass increasing rate of Li inside the Si calculated with $\frac{dM^*}{dt} = \frac{d(\int cdV)}{dt}$ to that entered the Si electrode

through the surface. The results showed that $m_c = V/V_0$ was valid for the two examined cases with a variety of model representations. Simulations were then carried out for both thin film and sphere geometries with correction $m_c = V/V_0$ with a Li diffusivity, $D = 5.0 \times 10^{-16}$ m²/s. The error in mass conservation was within 3%, Fig. 3.3(d).

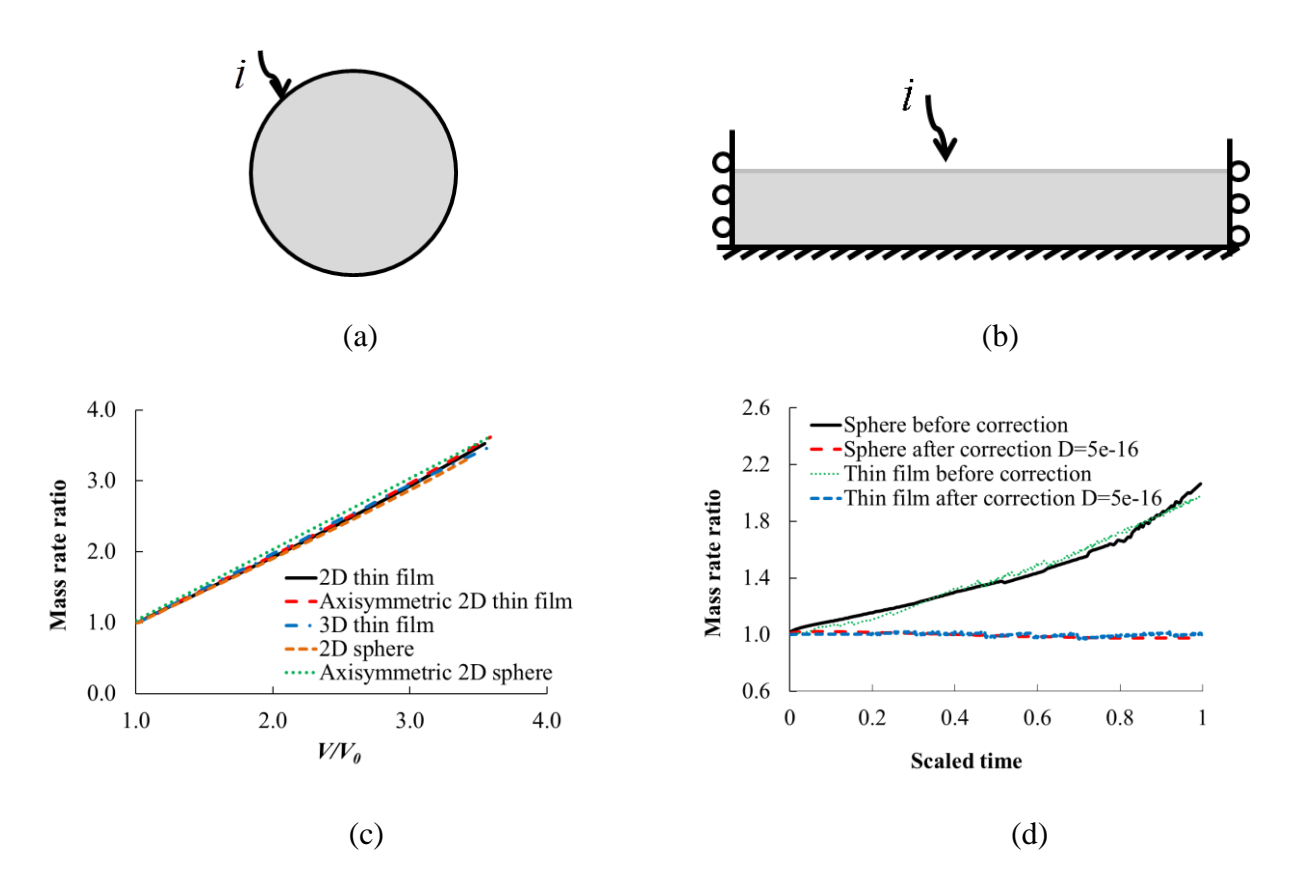


Figure 3.3 Verification of the mass correction coefficient with (a) a free expanding Si sphere and (b) a constrained thin film Si on a substrate, expanding only in the through thickness direction. (c) The mass rate ratio as a function of volume ratio V/V_0 . The results showed that the mass correction coefficient follows the relation of $m_c = V/V_0$. (d) The mass conservation was maintained for both thin film and sphere geometries.

3.2.3 Stress Generation in Si

The Cauchy stress tensor σ is related to the elastic strains in Si by Eq. 3.30 to 3.32

$$\sigma = J^{-1} \mathbf{F} \mathbf{S} \mathbf{F}^{\mathsf{T}} \tag{3.30}$$

where \mathbf{F} is the deformation gradient tensor, J is the determinant of \mathbf{F} , \mathbf{S} is the second Piola-Kirchhoff stress tensor which can be derived from the relation

$$\mathbf{S} = \mathbf{S_0} + 2\frac{\partial W_s}{\partial \mathbf{C}} \tag{3.31}$$

where \mathbf{C} is the elastic right Cauchy-Green deformation tensor, $\mathbf{C} = \mathbf{F}_{el}^T \mathbf{F}_{el}$. The Cauchy stresses refer to the current configuration, whereas the second Piola-Kirchhoff stresses refer to the reference configuration. W_s is the strain energy density calculated based on the elastic Lagrange strain tensor \mathbf{E} as

$$W_{\rm s} = \Lambda \text{tr}(\mathbf{E})^2 + M \text{tr}(\mathbf{E}^2) \tag{3.32}$$

where $\mathbf{E} = (\mathbf{C} - \mathbf{I})/2$; The Λ and M are the Lamé constants which are giving in terms of Young's modulus E and Poisson's ratio ν , $\Lambda = \nu E/((1+\nu)(1-2\nu))$, $M = E/(2(1+\nu))$.

The non-homogeneous volume expansion in a solid results in stresses. The high stress may lead to the yielding of the Si anode. The yield function f is defined as

$$f = \sigma_{VM} - \sigma_Y \tag{3.33}$$

where σ_{VM} is the Von Mises stress; σ_{Y} is the yield stress, which is a function of the Li concentration. The post yielding response was assumed to be perfect plastic.

3.2.4 Fluid Electrolyte

The fluid flow is described by the Navier-Stokes equation

$$\rho_{fluid} \left(\frac{\partial \mathbf{v}_{fluid}}{\partial t} + \mathbf{v}_{fluid} \cdot \nabla \mathbf{v}_{fluid} \right) = -\nabla p + \mu_{fluid} \nabla^2 \mathbf{v}_{fluid}$$
(3.34)

where $\mathbf{v}_{\textit{fluid}}$ is the electrolyte fluid velocity; $\rho_{\textit{fluid}}$ is the density of electrolyte; p is atmosphere pressure at 1atm and $\mu_{\textit{fluid}}$ is the electrolyte dynamic viscosity.

3.2.5 Current Collector

In literature, both Cu[157] and stainless steel[158] have been used as the current collector for Si anode. The Cu and stainless steel are modeled by piece-wise linear elastic-plastic models. Their stress-strain curves are given in Fig. 3.4.

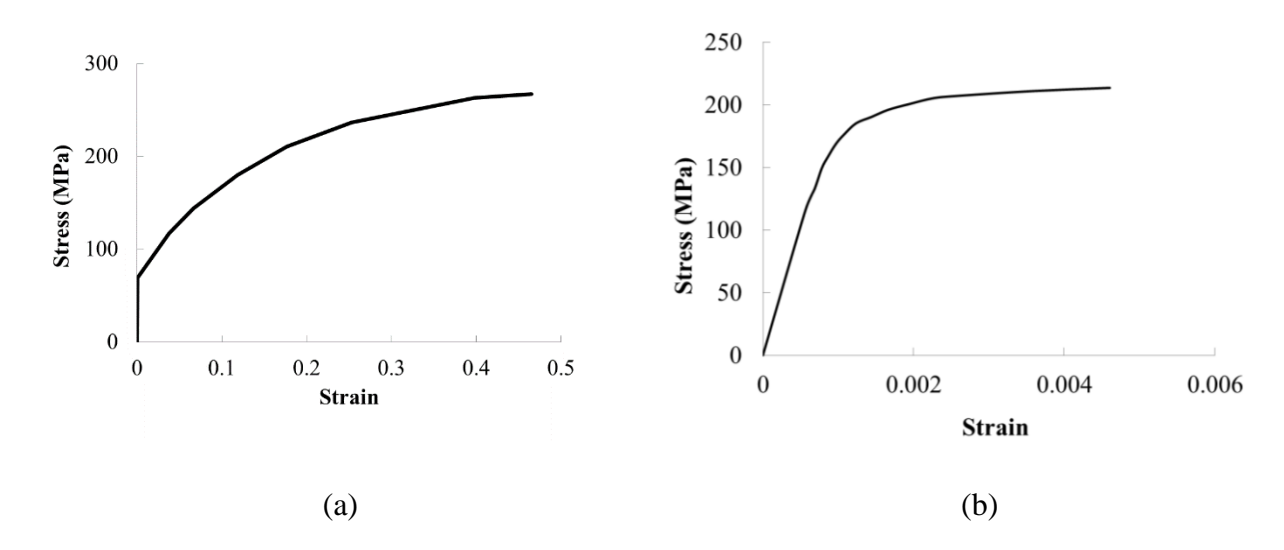


Figure 3.4 The stress-strain curve for (a) Cu substrate[157], and (b) stainless steel substrates[158]

3.2.6 Boundary Conditions

The fluid/solid interaction at the Si-electrolyte interface is considered by a force ${\bf f}$ exerted on Si boundary by the fluid, which is calculated as

$$\mathbf{f} = \mathbf{n} \cdot \left\{ -p\mathbf{I} + \left(\mu_{fluid} \left(\nabla \mathbf{v}_{fluid} + \left(\nabla \mathbf{v}_{fluid} \right)^T \right) - \frac{2}{3} \mu_{fluid} \left(\nabla \cdot \mathbf{v}_{fluid} \right) \mathbf{I} \right) \right\}$$
(3.35)

Both the Si electrode and the current collector can be viewed as a wall for the fluid electrolyte. Therefore,

$$\mathbf{n} \cdot \mathbf{v}_{fluid} = 0 \tag{3.36}$$

For fluid phase, the upper and lower boundaries are treated as no-slip boundary condition, so that

$$\mathbf{v}_{fluid} = 0 \tag{3.37}$$

For solid phase (Si electrode, current collector and Li reference electrode), the upper and lower boundaries are treated as roller boundaries, so that

$$\mathbf{n} \cdot \mathbf{u}_{solid} = 0 \tag{3.38}$$

3.3 Modeling Parameters

3.3.1 Parameters in "Battery" Sub-Model

3.3.1.1 Electrode Properties

Besides the uncertainty in Li diffusivity as mentioned earlier, the electronic conductivity of Li_xSi was also reported to vary with lithiation of Si. McDowell et al.[107] measured the electronic conductivity of Li-Si alloy in amorphous Si thin film. The results from three different tests were presented in Fig. 3.5. As shown, the conductivity ranges widely from 10^{-3} to 10^{2} S/cm. On the other hand, the Chandrasekaran and Fuller modeled the 1D Li-ion cell with Si composites[138] using the conductivity value (k_{I} in Eq. 3.10) of 33 S/m. Comparing the changing range in experiments to the simulation data, we found that the 33 S/m could be used as a reasonable electronic conductivity value in the MRM model. The influence of k_{I} to the cell performance is also investigated and discussed in Appendix C.

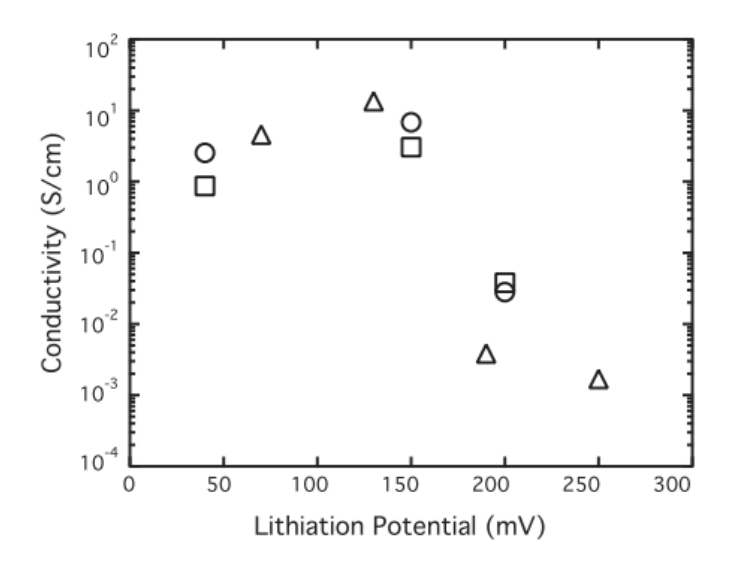


Figure 3.5 Measurement of electronic conductivity in amorphous Si thin film held at various potentials between 350 and 0 mV where the Li-Si alloy phase form [107].

3.3.1.2 Electrolyte Properties

The electrolyte was modeled as an incompressible fluid. In literature, the electrolyte density and viscosity have been reported as functions of salt concentration, solvent composition, and temperature, etc.[159,160]. The electrolyte density of LiPF₆/EC/DMC system varies around 1100-1200 kg/m³ and the dynamic viscosity varies around 0.5-2 mPa·s [159,160]. For simplification, the density and viscosity of the fluid electrolyte were assumed to be those of water, i.e. $\rho_{\text{fluid}} = 1000 \text{ kg/m}^3$ and $\mu_{\text{fluid}} = 0.9 \text{ mPa·s}$.

Table 3.1 presents a summary of the parameter values used in the current model. For Si, the Li diffusivity in Si, the apparent transfer coefficient (α_a and α_c) in Butler-Volmer equation (Eq. 3.15) and the reaction rate constant k_0 in Eq. 3.17 and have not been well established. The values of these parameters are labeled as to be determined (TBD) and they will be determined in later chapters.

Table 3.1 Parameters used in the MRM model.

Symbol	Name/Description	Value
α_a, α_c	Apparent transfer coefficient	TBD in Chapter 6
D_1	Li diffusivity in Li _x Si	TBD in Chapter 4
D_2	Diffusion coefficient of LiPF ₆ in organic solvent (EC:DMC=2:1 vol.%) [131]	$1.27 \times 10^{-11} (\text{m}^2/\text{s})$
i_{Li}	Exchange current density for the electrochemical reaction at the lithium foil [138]	$12.6 (A/m^2)$
t ₊	Cation transport number representing the percentage of the current in the electrolyte carried by Li-ion [138]	0.38
k_1	Electronic conductivity of Li _x Si [107,138]	Averaged at 33 (S/m)
k_0	Reaction rate constant	TBD in Chapter 6
c_{theory}	Theoretical maximum Li concentration [151]	$3.11 \times 10^5 (\text{mol/m}^3)$
R	Gas constant	8.314 J/(K mol)
T	Temperature	298 (K)
Ω	Partial molar volume [151]	$9 \times 10^{-6} (\text{m}^3/\text{mol})$
$ ho_{ extit{ iny fluid}}$	Electrolyte density	$1000 (kg/m^3)$
$\mu_{ extit{fluid}}$	Dynamic viscosity of electrolyte	0.9 (mPa s)

3.3.2 Mechanical Properties

The mechanical properties of lithiated Si, including the elastic modulus, the Poisson's ratio and the yield stress, were described with three piecewise linear relationships vs. SOC as shown in Fig. 3.6. The elastic modulus was from the first principle calculation of Li_xSi subjected to a uniaxial tension reported by Zhao et al.[105]. The Poisson's ratio was calculated by Shenoy et al.[108]. For the yield stress, there was a significant discrepancy between the computed values[65] and the experimental results[60,63]. Based on the range reported in literature, a simple linear yielding function verses SOC was used in the current model based on experiments by Sethuraman et al.[60].

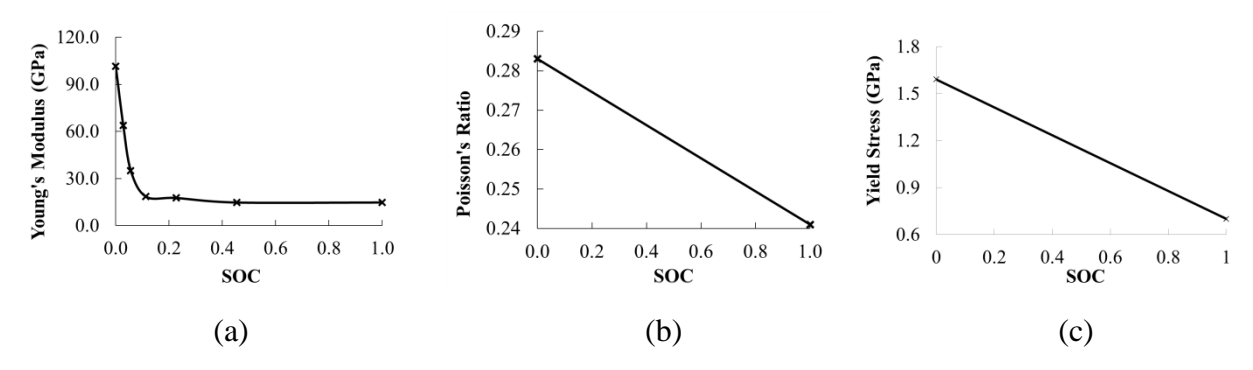


Figure 3.6 Mechanical properties of Li_xSi used: (a) elastic modulus, (b) Poisson's ratio, and (c) yield stress.

3.3.3 Source of Parameter and Form of Si Used

As the interest of this work is focus on a-Si, when the parameter was searched in the literature, only that obtained from a-Si is obtained. Or in some cases where the data for a-Si phase was not available, the parameters from other form of Si, such as c-Si phase or the Si composites were used. Parameters are adopted from both experimental measurement and simulation predictions are adopted. Some may be evaluated from multiple sources. The source of parameter, type of study and the form of Si used is listed in Table 3.2.

Table 3.2 Source of parameter used for Si

Parameter	Source	Type of study	Form of Si used
Partial molar volume	[151]	Experiment	Si composite
m³/mol	[15]	Experiment	a-Si thin film
OCP in Fig. 6.1(a)	[118]	Experiment	a-Si thin film
Elastic modulus	dulus [105] Molecular dynamic Simulation		a-Si
Poisson's ratio of Li _x Si	[108]	Molecular dynamic Simulation	a-Si
Estimated yield stress	[60,63]	Experiment	a-Si thin film
	[138]	Continuum simulation	Si composites, phase
Si conductivity		assumption	not specified
Si conductivity	[107]	Experiment	Si nanowire, phase not
	[10/]	Experiment	specified

Chapter 4 Study of Lithium Diffusivity in Amorphous Silicon via Finite Element Analysis 4.1 Introduction

This chapter studies the key material property for a-Si, the Li diffusivity in Si, which is a key parameter determining the lithiation time and Li concentration gradient, the latter in turns influences the intercalation stresses.

The reported Li diffusivity values, however, vary a great deal, ranging from $10^{-13} m^2/s$ to $10^{-19} m^2/s$ [63,85,94–99]. Furthermore, the experimentally measured diffusivity is based on the initial Si volume. Such values cannot be used directly in analysis with large volume variations.

This chapter investigates the possible range of the Li diffusivity in a-Si through correlations of numerical simulations with the in-situ lithiation experiments by McDowell et al.[42]. To simulate the large deformation of Si, a large strain based formulation for the concentration induced volume expansion is proposed. The problem is solved using COMSOL Multiphysics[®].

4.2 Model Development and Implementation

In literature, McDowell et al.[42] investigated the lithiation of a-Si nanospheres in-situ in a transmission electron microscope (TEM). The experimental setup is shown in Fig. 4.1(a). Li was supplied to a-Si spheres through crystalline silicon (c-Si) pillars. Potentiostatic charge and discharge under 3V were carried out. The images and video clips showed that during lithiation and delithiation, the a-Si spheres expanded and contracted radially and remained a spherical shape. During the first lithiation, a boundary between Li-rich and Li-poor regions (named as reaction front) was clearly visible, Fig. 4.1(b). This phenomenon is known as the two-phase lithiation.

The experiment by McDowell et al.[42] provides a good study case. The spherical growth pattern suggests that the constraint of the Si pillar to the spheres was negligible, the spheres

behaved as free-standing structures; and the sphere grew as having a uniform Li supply at its surface. In addition, since the spheres were not in contact with the electrolyte, there were no solid-electrolyte interface (SEI) layers on the particle surface.

The a-Si sphere was modeled as 2D axisymmetric. Fig. 4.1(c) presents the schematic of the model along with the boundary condition. The potentiostatic charge was simulated by a constant Li concentration boundary condition. The Li concentration corresponding to Li_{3.75}Si was applied during lithiation. To ensure the stability of the simulations, it was introduced with a ramp of 3s. The sphere was allowed to expand freely during lithiation.

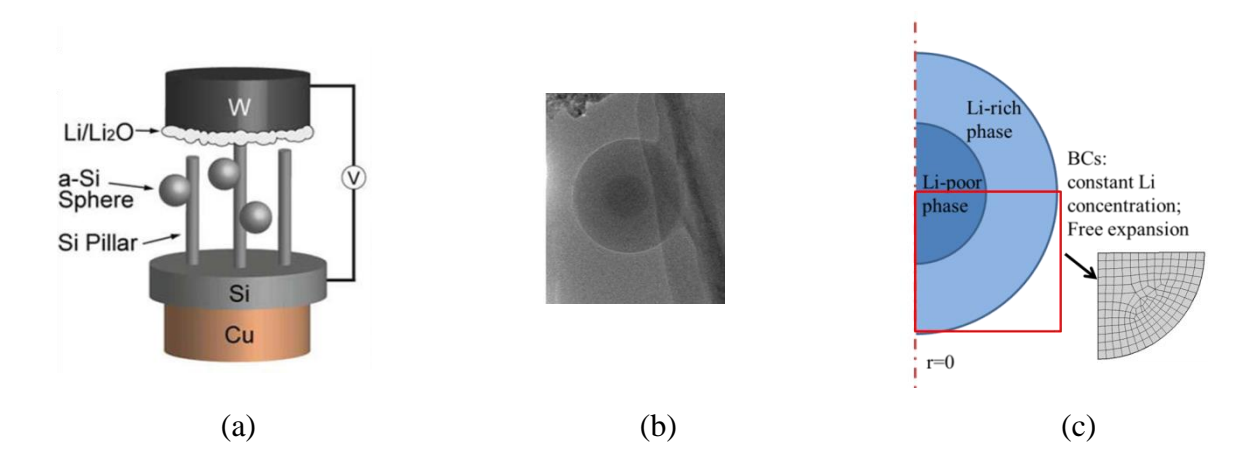


Figure 4.1 Axisymmetric model for modeling lithiation of a-Si nanoparticle. (a)

Experimental setup by McDowell et al.[30]; (b) two-phase lithiation in the first lithiation observed in experiment [30]; and (c) simulating two-phase lithiation of a-Si nanospheres using an axisymmetric 2D model.

In an MRM battery model[161], the Butler-Volmer equation would be used to consider the electrochemical reaction at the electrode/electrolyte interface. In the experiment[30], however, the a-Si spheres were not in direct contact with the electrolyte and they were lithiated with excess

Li supply. Therefore, a simple Li concentration boundary condition was sufficient to approximate the experimental setup.

The physical phenomena involved inside the a-Si sphere are Li diffusion (studied by Eq. 3.1), the diffusion induced elastic-plastic deformation and Li intercalation induced stresses (Section 3.1-3.3). Table. 4.1 summarizes the governing equations for this problem. The problem formulations and their implementation in the model are presented next.

Table 4.1 Governing equations for Si model in Chapter 4 (Symbols are explained in Nomenclature).

Physics	Governing Equations	Eq. No.
Li Diffusion	$\frac{\partial c_1}{\partial t} + \nabla \cdot (-D\nabla c_1) = 0$	(3.1)
Deformation	$\mathbf{F} = \mathbf{F}_{el}\mathbf{F}_{inel} = \mathbf{F}_{el}\mathbf{F}_{p}\mathbf{F}_{c}$	(3.22)
	$\mathbf{F} = \mathbf{F}_{el}\mathbf{F}_{inel} = \mathbf{F}_{el}\mathbf{F}_{p}\mathbf{F}_{c}$ $\frac{V}{V_{0}} = \det(\mathbf{F}_{c}) = 1 + \Omega \Delta c$	(3.23)
Stress	$\sigma = J^{-1} \mathbf{F} \mathbf{S} \mathbf{F}^{\mathrm{T}}$	(3.30)
	$\sigma = J^{-1}\mathbf{F}\mathbf{S}\mathbf{F}^{T}$ $\mathbf{S} = \mathbf{S}_{0} + 2\frac{\partial W_{s}}{\partial \mathbf{C}}$ $W_{s} = \Lambda \operatorname{tr}(\mathbf{E})^{2} + M \operatorname{tr}(\mathbf{E}^{2})$	(3.31)
	$W_{S} = \Lambda \text{tr}(\mathbf{E})^{2} + M \text{tr}(\mathbf{E}^{2})$	(3.32)

4.3 Li Diffusivity in a-Si

The literature data on Li diffusivity in Si varies over a wide range [63,85,94–99]. Table 4.2 provides a summary of reported values for a-Si. For comparison, the representative values for Li in c-Si are also listed in the first three rows. As shown, the Li diffusivity is about one to two orders higher in a-Si than that in c-Si. Furthermore, the values estimated by ab initio molecular dynamics (MD) simulations [85] and potential step chronoamperometry (PSCA) [95], where chemical diffusion took place, appears to be much higher than the values determined by

electrochemical experiments such as the cyclic voltammetry (CV)[99], electrochemical impedance spectroscopy (EIS)[98], galvanostatic intermittent titration technique (GITT)[22], and potentiostatic intermittent titration technique (PITT) [63,97].

The large variation in diffusivity measurement is attributed to the complex physics involved in lithiation of Si. The diffusivity measured with electrochemical experiments may include the effect of interface reaction, stress-diffusion interaction, the contribution of SEI layer, and etc. For instance, Bucci et al.[63] considered the stress-diffusion interaction and chemical interaction of Li with Si host and determined an intrinsic diffusivity of $10^{-19}m^2/s$ based on PITT experiment. Li et al.[97] reported that their samples were cycled four times between 1.0 to 0.3V to form a stable SEI layer before measurement. SEI layer is reported to act as a Li-ion diffusion barrier, limiting Li-ion transport with a high resistivity[63,162]. Furthermore, the diffusivity determined by experiments is an averaged value across the electrode over one or multiple cycles, and may be a function of potential or state-of-charge (SOC)[94,98]. Results may be strongly dependent on Si geometry and size[96]. Finally, the experimentally determined diffusivity is based on the initial volume. Such values cannot be used directly in analysis considering volume changes.

Table 4.2 Literature data on Li diffusivity in Si.

Method	Li Diffusivity in Si (m²/s)	Material	Current density
ab initio MD [85]	$1.67 \times 10^{-14} \sim 4.88 \times 10^{-13}$	c-Si slab	chemical diffusion
CV, EIS, GITT [94]	1×10 ⁻¹⁶	1×10 ⁻¹⁶ nano c-Si	
PSCA [95]	2×10^{-15}	single crystal wafer	chemical diffusion
ab initio MD [85]	$1.25 \times 10^{-13} \sim 3.69 \times 10^{-12}$	a-Si slab	chemical diffusion
PSCA [95]	1×10 ⁻¹³	a-Si thin film	chemical diffusion
PITT [97]	$7.7 \times 10^{-18} \sim 1.0 \times 10^{-17}$	100nm and 1000nm a-Si film	0.07mA/cm^2
EIS [98]	$3\times10^{-17}\sim3\times10^{-16}$	a-Si thin film	$0.4V, 0.0025 \text{ mA/cm}^2$
CV [99]	1.9×10^{-17}	120nm a-Si thin film	0.1 mA/cm^2
PITT [63]	1×10 ⁻¹⁹	104nm a-Si thin film	discharge, 0.395 to 0.39V, Intrinsic value

To estimate the order of Li diffusivity in Si with volume change, a numerical parameter study was conducted for the experiment in Fig. 4.1. Both the two-phase lithiation observed in the first lithiation and the single-phase lithiation observed in the subsequent cycles were investigated.

The two-phase phenomenon in the first lithiation is related to a lower Li diffusivity in pristine Si. In general, the diffusivity in Li-poor phase is about an order lower than that in Lirich phase. In the current investigation, for the first lithiation, the diffusivity values were assigned separately for the Li-poor core and the Li-rich shell with a rapid increase of Li diffusivity at reaction front, as shown in Fig. 4.2. The exact composition of the metastable a-Li_xSi at the reaction front was difficult to determine[163,164]. Based on literature discussions[48,165,166], the composition was assumed as Li₂Si in the current study. Within each phase, the diffusivity was assigned as a constant and the Li composition dependency was not considered. The diffusivity determined for Li-rich phase was then used in simulations of single-

phase lithiation. Considering the uncertainty in Li diffusivity, the stress effect to the diffusivity was ignored in this work.

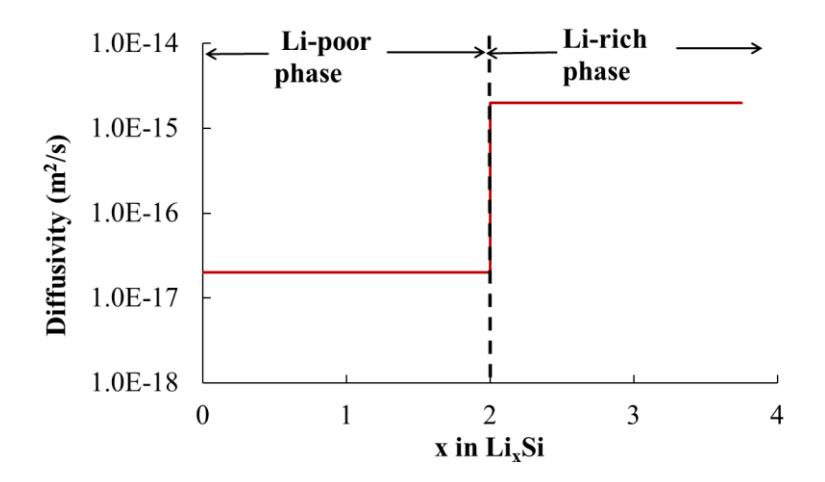


Figure 4.2 Constant diffusivity was assigned separately for Li-rich and Li-poor phases with a small transition at around Li₂Si.

Table 4.3 presents the initial six test cases for diffusivity study. The Li diffusivity in Li-poor and Li-rich phases were denoted as D_{poor} and D_{rich} , respectively. The tests were divided into two sets. The first set (Tests 1 to 3) was used to investigate D_{rich} , where D_{poor} was kept constant while D_{rich} varied from 1.0×10^{-15} m²/s to 1.0×10^{-14} m²/s. The second set (Tests 3 to 5) was used to investigate the D_{poor} , where D_{rich} was kept constant while D_{poor} varied from 1.0×10^{-18} m²/s to 1.0×10^{-16} m²/s. Test 6 was added based on the results of Tests 1-5. Results will be discussed in later session.

Table 4.3 Diffusivity study test cases.

Test label	Li-poor Diffusivity D_{poor} (m ² /s)	Li-rich Diffusivity D_{rich} (m ² /s)
Test 1	1.0×10 ⁻¹⁷	1.0×10^{-15}
Test 2	1.0×10^{-17}	1.0×10^{-14}
Test 3	1.0×10^{-17}	2.5×10^{-15}
Test 4	1.0×10^{-18}	2.5×10^{-15}
Test 5	1.0×10^{-16}	2.5×10^{-15}
Test 6	2.0×10^{-17}	2.0×10^{-15}

4.4 Results and Discussion

4.4.1 Two-Phase Lithiation

TEM images from McDowell et al.[42] showed the lithiation process of an a-Si sphere with diameter about 570 nm at several time frames, as presented in the first row in Table 4.4. An a-Si sphere of the same size was simulated according to the six tests in Table 4.3. The simulation results were compiled in Table 4.4, which compares the Li concentration distributions and the reaction front in the sphere with the experimental result. The scaled bar was normalized to the maximum achieved c_1 (81884 mol/m³).

In the first set simulations (Tests 1 to 3), the results showed that when $D_{rich} \le 1.0 \times 10^{-15} \text{ m}^2/\text{s}$, the two-phase lithiation was still in progress at 129s, which was much longer than the time for Li-poor phase to disappear observed in the experiment. On the other hand, when $D_{rich} \ge 1.0 \times 10^{-14} \text{ m}^2/\text{s}$, the Li-poor phase disappeared at about 60s, which was much shorter than the time in the experiment. Test 3, with $D_{rich} = 2.5 \times 10^{-15} \text{ m}^2/\text{s}$, matched the experiment reasonably well.

Table 4.4 Comparison of simulations with experimental results of two-phase lithiation.

Test label	48s	61s	129s	Comments
Experiment – first lithiation of a-Si[42]	48 s	61 s	129 s a-LixSi sphere	1.0 0.8 0.6 0.4 0.2 0.0 Scale bar for Li concentration in simulatons.
Test 1				$D_{rich} \leq 1.0 \times 10^{-15} \text{ m}^2/\text{s}$, the time for two-phase lithiation was much longer than that in the experiment.
Test 2				$D_{rich} \ge 1.0 \times 10^{-14} \text{ m}^2/\text{s}$, the Lipoor phase disappeared before 60s, which was much shorter than the time in the experiment.
Test 3				$D_{rich} = 2.5 \times 10^{-15} \text{ m}^2/\text{s}$, matched the experiment reasonably well.
Test 4				$D_{poor} \leq 1.0 \times 10^{-18} \mathrm{m^2/s} \qquad ,$ lithiation time increased greatly.

Table 4.4 (cont'd)

Test 5		$D_{poor} \ge 1.0 \times 10^{-16} \text{ m}^2/\text{s} \text{ resulted}$ in a diffused reaction front.
Test 6		Best correlation with experimental results.

The results in the second set of simulations (Tests 3 to 5) showed that D_{poor} , the diffusivity in Li-poor phase, had a significant influence on the lithiation time. When D_{poor} was small (Test 4), the lithiation time greatly increased. When D_{poor} was large (Test 5), the lithiation time reduced but the reaction front was diffused.

The effect of D_{poor} was further examined by comparing the concentration profiles obtained from simulation (Fig. 4.3(b)) with the experimental results (Fig. 4.3(a)). The experimental profiles were established according to the light intensity in TEM images[42]. It should be noted that the light intensity may not have a linear relationship with the Li concentration. The profiles generated this way, therefore, were only qualitative indications. As shown in Fig. 4.3(b), Test 3 and 4 resulted in Li concentration oscillations in the Li-poor phase near the reaction front. This was caused by the relatively steep diffusivity gradient at the reaction front. The smaller D_{poor} in Test 4 caused a larger scale of concentration oscillation. Diffusivity values in both tests were

rejected because they did not match well with the experimental profile in Fig. 4.3(a). Test 5 resulted in a much diffused reaction. Therefore, a new test case, Test 6, was added. The concentration profiles in Test 6 had a distinguishable reaction front at 48s and 61s, resembling those depicted in experiments. Among all test cases, Test 6 appeared to provide the best correlation between simulation and experiment. This yielded the diffusivity values of $D_{poor} = 2.0 \times 10^{-17} \text{ m}^2/\text{s}$ and $D_{rich} = 2.0 \times 10^{-15} \text{ m}^2/\text{s}$.

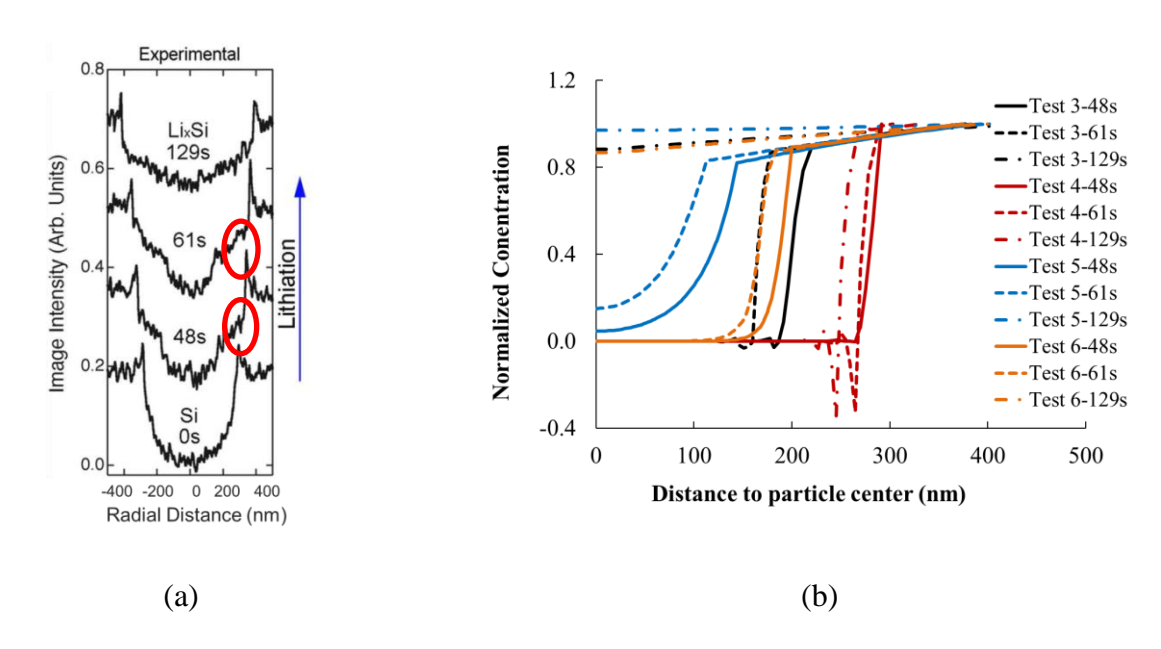


Figure 4.3 Concentration profile comparison: (a) The image intensity during lithiation of the 570 nm diameter sphere during lithiation in experiments [42]. Red circles label the concentration Figure 4.3 (cont'd) drop at the reaction front. (b) Lithiation of Si in Tests 3 to 6 in simulations: concentration profile vs. distance to particle center.

Comparing with the diffusivity values in Table 4.4, the value of $D_{rich} = 2.0 \times 10^{-15} \text{ m}^2/\text{s}$ is one to two orders higher than that measured by electrochemical experiments[97–99] but two orders lower than the value determined by chemical diffusion[85,95]. The electrochemical experiments

include the effect of SEI layer, and the Li diffusivity is determined with the dimension of undeformed Si electrode. Taking these factors into consideration, $D_{rich} = 2.0 \times 10^{-15} \text{ m}^2/\text{s}$ is in a reasonable range.

McDowell et al.[42] also plotted the thickness of the Li-rich phase (lithiated-thickness) versus time, as showed in Fig. 4.4(a). The results showed the thickness increased linearly with time. However, the slopes of these curves varied over a wide range, which may be caused by differences in experimental conditions, such as the particle sizes and quality of electrical/Li⁺ pathway connection. The thickness plot was used to examine the Li diffusivity values established in Test 6. The specific information on the range of sphere sizes was not provided in Ref. [30]. To compare the results, simulations were carried out for spheres with diameter of 570 nm and 400 nm, because these two sizes were mentioned in Ref. [30]. As shown in Fig. 4.4(a), the lithiated thickness growth curves of both spheres obtained from simulations fell within the experimental range. The lithiated thickness increased almost linearly during the two-phase lithiation, as seen in the experiment. These results further confirmed that the Li diffusivity values in Test 6 were reasonable estimations. Finally, in simulations, the slope of the curves reduced to nearly zero when the Li-poor phase was consumed. Further lithiation proceeded in Li-rich phase as the sphere continued to grow.

4.4.2 Single-Phase Lithiation

As reported in Ref. [42], Si undergoes two-phase lithiation only in the first lithiation. The subsequent delithiation and lithiation display as a single-phase process without a visible reaction front. Furthermore, the time for lithiation is greatly reduced. For a-Si sphere of 400 nm, the lithiation time was 122 seconds and 31 seconds for the first and second lithiation, respectively. The disappearance of the two-phase lithiation is likely due to the further amorphization of a-Si.

a-Si may have some short range order in local areas. Li insertion disturbed the ordered structure as in the amorphization of c-Si[165]. Diffusion proceeds fast in amorphous host. Therefore the subsequent lithiation is similar to that in Li-rich phase.

The single-phase lithiation was simulated for a-Si sphere of 400 nm with $D = 2.0 \times 10^{-15} \ m^2/s$, the value for the Li-rich phase in two-phase lithiation. In single-phase lithiation, the reaction front was assumed at Li₂Si, the same as in two-phase lithiation. The location of the reaction front was determined from concentration profile plots at different time intervals. Fig. 4.4(b) showed that the single-phase lithiation of the sphere took about 30 seconds while the two-phase lithiation took more than 70 seconds. The simulation results agreed with the experimental observations quite well, confirming that $D = 2.0 \times 10^{-15} \ m^2/s$ is a reasonable estimation for a-Si single-phase lithiation.

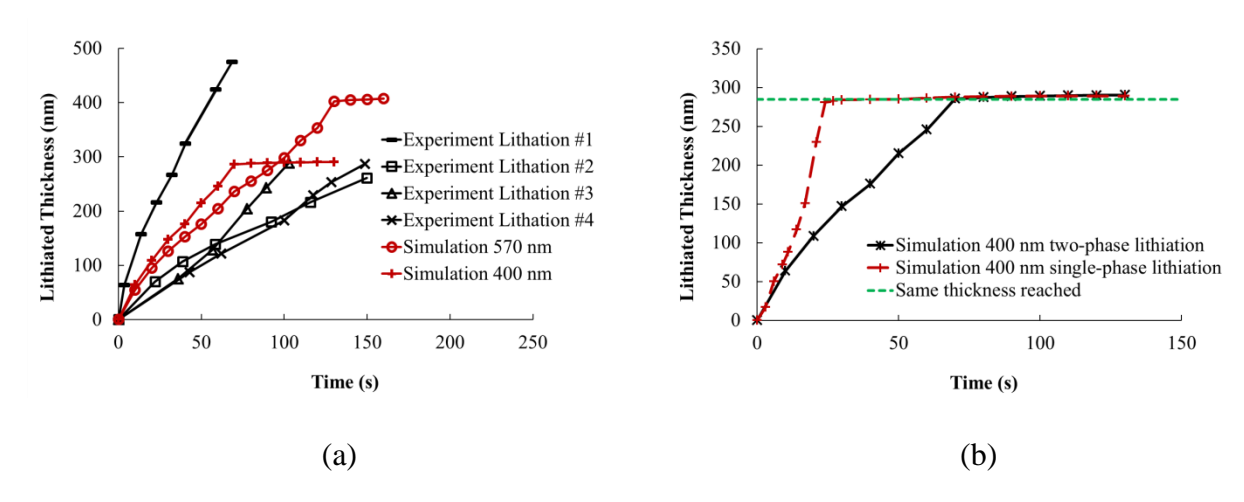


Figure 4.4 Lithiated thickness as a function of time during lithiation of a-Si spheres, including: (a)

Two-phase lithiation comparison between results from experiments and simulations.

Experimental curves (black) #1-#4 are from McDowell et al.[42] out of 26 nanospheres with unspecified diameter range. Simulation curves (red) are a-Si spheres of 400 nm and 570 nm. (b)

Comparing lithiation speed between single-phase lithiation and two-phase lithiation.

4.4.3 Concentration Dependency of Diffusivity

Li diffusivity may be a function of Li concentration. Metastable a-Li_xSi phases form during lithiation before a-Si becomes fully lithiated. Therefore, the Li diffusivity may vary when Li_xSi composition and the network structural change. The concentration dependency of the diffusivity, however, is unclear.

To investigate the effect of the concentration dependency of the diffusivity, additional simulations were performed with a relationship proposed by Berla et al.[167]

$$D = (1 - c/c_{\text{max}})^3 D_{poor} + (c/c_{\text{max}})^3 D_{rich}$$
 (4.1)

Two new tests were performed using a diffusivity described by Eq. 4.1. In Test 7, the values used in Ref. [51], $D_{poor} = 1.0 \times 10^{-17} \,\mathrm{m^2/s}$ and $D_{rich} = 1.0 \times 10^{-16} \,\mathrm{m^2/s}$, were adopted. In Test 8, the values established in the current work, $D_{poor} = 2.0 \times 10^{-17} \,\mathrm{m^2/s}$ and $D_{rich} = 2.0 \times 10^{-15} \,\mathrm{m^2/s}$, were used. As shown in Fig. 4.5(a), Eq. 4.1 described a smooth curve instead of a sharp change. As a result, the reaction front between Li-poor and Li-rich was not maintained in Test 7 and 8. As shown in Fig. 4.5(b), the lithiated thickness growth curves predicted by Test 7 and 8 deviated from the nearly linear growth tend observed in experiments. In comparison, the simulation with a simple approximation of constant diffusivity values in Test 6 matched the experimental trend closer.

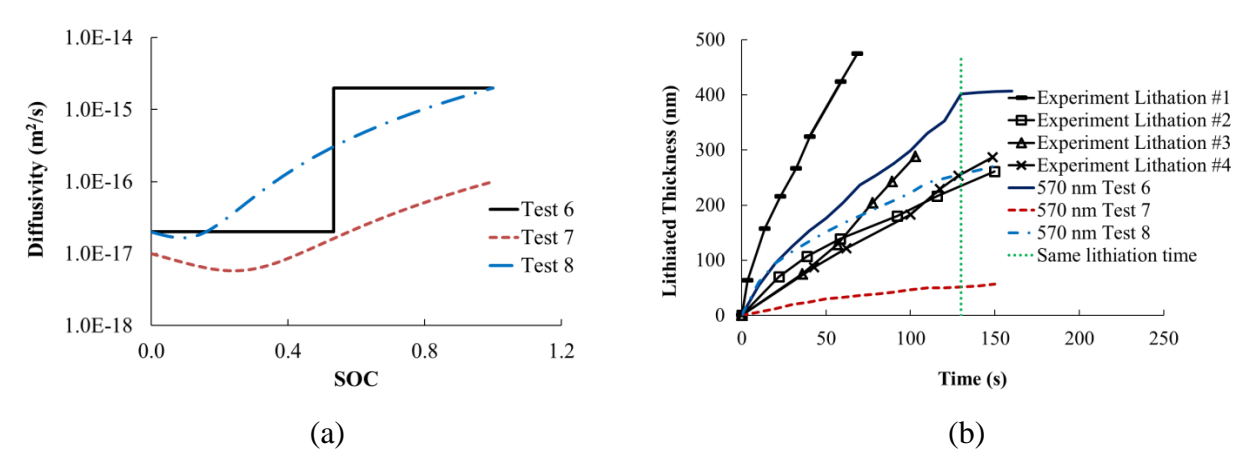


Figure 4.5 Simulations of lithiation of Si sphere of 570 nm diameter with a concentration dependent diffusivity. (a) Diffusivity functions; (b) Lithiated-thickness versus time, comparing to experimental data reported in Ref. [30] as shown in Fig. 4.4(a).

4.5 Conclusion

The Li diffusivity in the two-phase lithiation and the subsequent single-phase lithiation of a-Si was investigated by simulating the in-situ TEM experiments of a-Si nanospheres[42]. To simulate the large deformation of Si, a large strain based formulation for the concentration induced volume expansion was used. The coupled diffusion and deformation problem was solved in COMSOL Multiphysics[®]. The diffusivity of Li in a-Li_xSi was approximated with two distinct diffusivity values for the Li-poor phase and Li-rich phase, respectively. Simulations with Li diffusivity values ranging from 1.0×10^{-18} m²/s to 1.0×10^{-14} m²/s were carried out and the results were compared with experiments for the movement of the reaction front, the lithiated-thickness growth, and the lithiation time. The Li diffusivity was found at the order of 2.0×10^{-15} m²/s for Li-rich phase and 2.0×10^{-17} m²/s for Li-poor phase in the two-phase lithiation. The single-phase lithiation of a-Si after the first cycle was simulated with a Li diffusivity of 2.0×10^{-15} m²/s. The computed lithiation time agreed well with the experimental results.

The Li diffusivity for single-phase lithiation determined in this work is two orders lower than that determined by chemical diffusion process but one to two orders higher than that established in electrochemical experiments. The value reported here is in a reasonable range taking into account that the Li diffusivity is calculated for deformed Li_xSi volume and the analysis is for a case without the limiting effect on Li-ion transport from SEI layer.

Chapter 5 Investigation of the Chemo-Mechanical Coupling in Lithiation of Amorphous Si through Simulations of Si Thin Films and Si Nanospheres

5.1 Introduction

Si anode experiences large volume expansion/contraction (up to 400 %) of Si during lithiation cycles. The large volume variation of Si during lithiation/delithiation cycles can induce high stresses. This presents a great challenge to the structural integrity of LIBs. The high stresses and large volume variation have been cited as a primary cause for rapid capacity fading of LIBs with Si anode. Therefore, understanding the lithiation process, stress evolution and its effect on Si lithiation is of great importance for Si electrode design.

The stress evolution has been measured *in situ* during lithiation/delithiation for amorphous Si (a-Si) thin films[60,63,65,168]. The measured stress can reach as high as 1.5 GPa in both compression and tension. The stress also influences the lithiation process[61,62]. It was reported that, after the crystalline Si (c-Si) nanosphere had been lithiated for some time, the growth rate of lithiated thickness (thickness of Li_xSi shell in the first lithiation) reduced significantly[61]. The phenomenon was primarily attributed to the high compressive stress at the reaction front that eventually prohibited Li from further insertion. However, the mechanism of how the stress interacts with Si lithiation is not clear.

In literature, two categories of chemical-mechanical coupling theories have been proposed for the stress effect on Li diffusion into Si: (I) by influencing Li diffusivity, and (II) by influencing the chemical potential of Li in Si.

In category (I), it assumes that the Li diffusivity is modulated by the stress induced activation free energy barrier shift[69,74,75]. The rate of reaction depends on the activation energy (i.e. free energy between the ground state and transition state). So far, the relationship is qualitative

only. The activation energy is adjusted by either hydrostatic stress[69,169] or biaxial stress (in thin film) [170] with a coefficient which varies in a wide range.

In category (II), it postulates that the chemical potential of Li in Si changes because the free energy difference between Si and Li_xSi is altered by stress[63,64,76–79]. This effect is still quite argumentative given different treatments in literature[63,74,77,82,83,149,171,172]. For example, some proposed that only the hydrostatic stress influenced the chemical potential for ideal solution[83,124] or non-ideal solution[74] whereas others cast the chemical potential as a function of both hydrostatic stress and deviatoric stress components[63,78].

The chemical-mechanical coupling has two facets: 1) the diffusion induced deformation and stress; 2) the stress effect on diffusion process. Because the co-existence of these two facets for any given geometry, it is difficult to determine the coupling relationship with a single geometry. In this work, two geometries will be investigated: a-Si thin film and a-Si nanosphere. In experiments with a-Si thin film, Li et al.[173] has observed a strong asymmetric rate behavior such that the lithiation capacity reduced much faster than that of delithiation with increasing the charging/discharging rates, i.e. the C rates. So far, the asymmetric rate behavior has only been reported for a-Si anodes in the form of thin films, but not for other geometries such as anodes with nanoparticles[174]. Since the stress state developed in a substrate-constrained thin film would be very different from that of a weakly constrained sphere during lithiation/delithiation, these two cases provide a unique opportunity for the investigation of chemical-mechanical coupling. A model with a correct coupling relationship would predict the rate behaviors of both geometries.

It should be noted that, although the abovementioned chemical-mechanical coupling theories have been formulated using both the small strain[63,171,172] and large strain[77,124]

frameworks, the Li transport is commonly considered with the normalized Li concentration calculated using the dimension of unlithiated Si. As a result, the analytical/simulation results could not be compared directly to the dimension/shape changes observed in experiments. In our previous work, a model that considers the lithiation/delithiation of Si with its accompanied volume change has been developed and used to determine the Li diffusivity in a-Si[115]. The current work extends the model to include chemo-mechanical coupling by considering the stress effect on chemical potential[142].

5.2 Model Setup

5.3 FE Models and Simulation Conditions

The physical phenomena involved inside a-Si electrodes are the diffusion of Li, diffusion induced deformations and stresses, and the coupling among them. Table 5.1 summarized the governing equations. This section presents the problem formulations and their implementation in the model.

Table 5.1 Governing equations for Si model in Chapter 5 (Symbols are given in Nomenclature).

Physics	Governing Equations	Eq. No.
Li Diffusion	$\left \frac{\partial c_1}{\partial t} + \nabla \cdot \left(-\frac{D_1}{RT} c_1 \nabla \mu_{Li_{x}Si}(\boldsymbol{\sigma}) \right) = 0 \right $	(3.1)
	$\mu_{Li_xSi}(\mathbf{\sigma}) = \mu_{Li_xSi}^0 + RT \ln \chi_{Li} + \Delta \mu_{Li_xSi}(\mathbf{\sigma})$	(3.4)
	$\Delta\mu_{Li_{x}Si}(\mathbf{\sigma}) = \alpha \Omega \sigma_{h}$	(3.5)
Deformation	$\mathbf{F} = \mathbf{F}_{el}\mathbf{F}_{inel} = \mathbf{F}_{el}\mathbf{F}_{p}\mathbf{F}_{c}$	(3.22)
	$\frac{V}{V_0} = \det(\mathbf{F}_c) = 1 + \Omega \Delta c$	(3.23)
Stress	$\sigma = J^{-1} \mathbf{F} \mathbf{S} \mathbf{F}^{\mathbf{T}}$	(3.30)
	$\mathbf{S} = \mathbf{S_0} + 2 \frac{\partial W_s}{\partial \mathbf{C}}$ $W_s = \Lambda \text{tr}(\mathbf{E})^2 + M \text{tr}(\mathbf{E}^2)$	(3.31)
	$W_{S} = \Lambda \operatorname{tr}(\mathbf{E})^{2} + M \operatorname{tr}(\mathbf{E}^{2})$	(3.32)

Two experiments with distinct geometries were selected to study the stress effect on Si lithiation: the first was the cycling experiment of a-Si thin film conducted by Li et al.[173]; the second was that of Si nanospheres by Liu et al.[174].

These two experiments were carried out galvanostatically but with two different conditions. In Ref. [173], the thin film was evaluated independently for single-phase lithiation and delithiation, i.e., a slow lithiation/delithiation at C/10 was performed to reach the same SOC before each delithiation/lithiation measurement at the desired rate. In Ref. [174], the anode with nanospheres was lithiated and delithiated under the same rate for at least ten cycles before moving to the next rate. These are simulated as Condition 1 and Condition 2 as shown in Table 5.2. Simulations for the two geometries were performed with both conditions.

Table 5.2 Two conditions used in simulations.

Condition 1	A slow lithiation/delithiation at C/10 is conducted before each			
	delithiation/ lithiation measurement at the desired rate			
Condition 2	The lithiation/delithiation measurement is conducted following a			
	delithiation/ lithiation at the same rate			

5.3.1 Amorphous Si Thin Film Model

Li et al.[173] galvanostatically cycled the a-Si thin film of 70 nm thickness in a Li-ion cell over a wide range of rates between 0.05 V and 2.0 V. The rate performance was evaluated following Condition 1. The cells were cycled a few times in advance to minimize the effect of solid-electrolyte interface (SEI)[173]. Their results are reproduced in Fig. 5.1, which shows that the reduction of capacity with C rate was much faster in lithiation than in delithiation. This was referred as the asymmetric rate behavior. It was attributed to the voltage shift introduced by the electrode Ohmic resistance at higher C rates, as the capacity is highly dependent on the voltage

at the end of lithiation but not so much at the end of delithiation. Although the authors suspected that the stress may be a contributing factor, it effect was not investigated in Ref. [173].

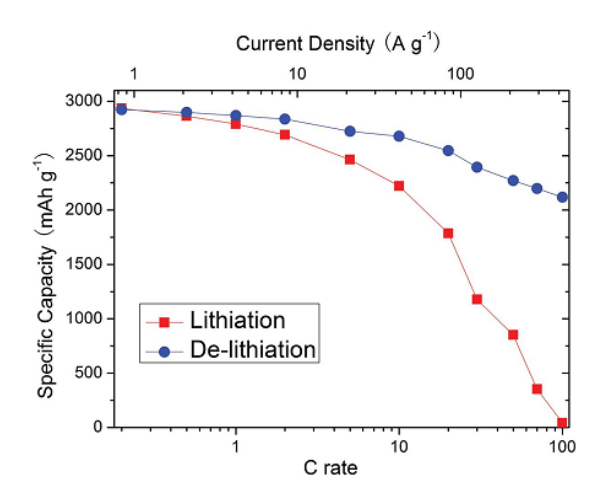


Figure 5.1 Asymmetric rate performance of 70nm a-Si thin film observed in experiment[173].

To simulate this experiment, a two-dimensional (2D) plane strain FE model was built, as shown schematically in Fig. 5.2. Since the experimental setup was not elaborated in detail in Ref. [173], the boundary conditions for the model were defined based on other Si thin film cycling experiments[60,175]. The Si thin film is usually deposited on a rigid substrate which restricts the in-plane expansion of the thin film. This boundary condition is often referred as substrate-constrained in literature. In the FE model, this boundary condition was simulated by constraining all degrees of freedom of the nodes at the bottom of the film. The thickness of the film was 70nm, the same as in Ref. [173]. In experiments, the width of the thin film is usually in the range of micrometers, which results in a large aspect ratio (width/thickness) of several hundred. In the FE model, the large aspect ratio was simulated with a film with a width/thickness ratio of 10 constrained by a symmetric (roller) boundary condition at the left and right hand sides. The upper surface of the film was allowed to expand freely. The Li flux was applied to the upper

surface according to the C rate used in Ref. [173]. The thin film was meshed with 5400 quadrilateral elements with an average size about 3 nm. The mesh is shown in Fig. 5.2.

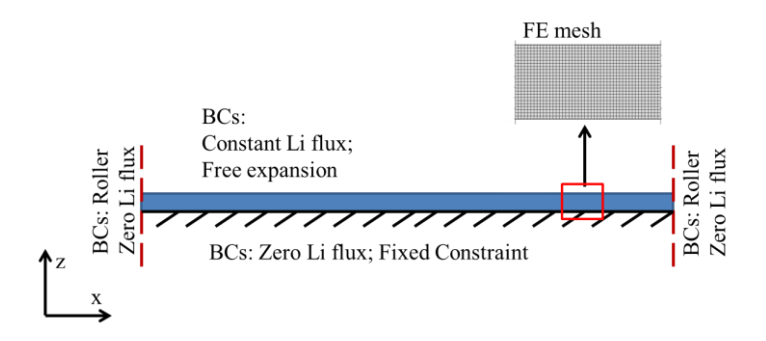


Figure 5.2 Schematic illustration of the 2D model for a-Si thin film with boundary conditions (BCs), and the FE mesh. The schematic is not drawn to scale.

The model for the thin film was first verified with the experiment of Sethuraman et al.[60], which measured the curvature change of substrate-constrained Si thin film during lithiation and delithiation. The *in-situ* stress variation was then determined using the Stoney equation[176,177]. The results were reported in terms of biaxial stress σ_b , which equals to the averaged in-plane stress in isotropic Li_xSi such that $\sigma_b = \sigma_{xx}^{ave} = \sigma_{yy}^{ave}$. Fig. 5.3(a) compares the model prediction with the experimental result for biaxial stress variation during cycling of a film of 250 nm thickness under C/4 rate. The chemo-mechanical coupling effect was not considered in the model because of the low rate. As seen, the film undergoes compression (up to -1.5 GPa) during lithiation, and reverses to tension (up to 1.5 GPa) upon delithiation. The predicted stress was in good agreement with the experiment both in the trend and the range. The stress profiles in thin film at various SOC under lithiation were showed in Fig. 5.3(b). This showed that, as the cycling rate was small, the Li concentration variation through the thickness was small and the stress distribution was almost uniform in the film.

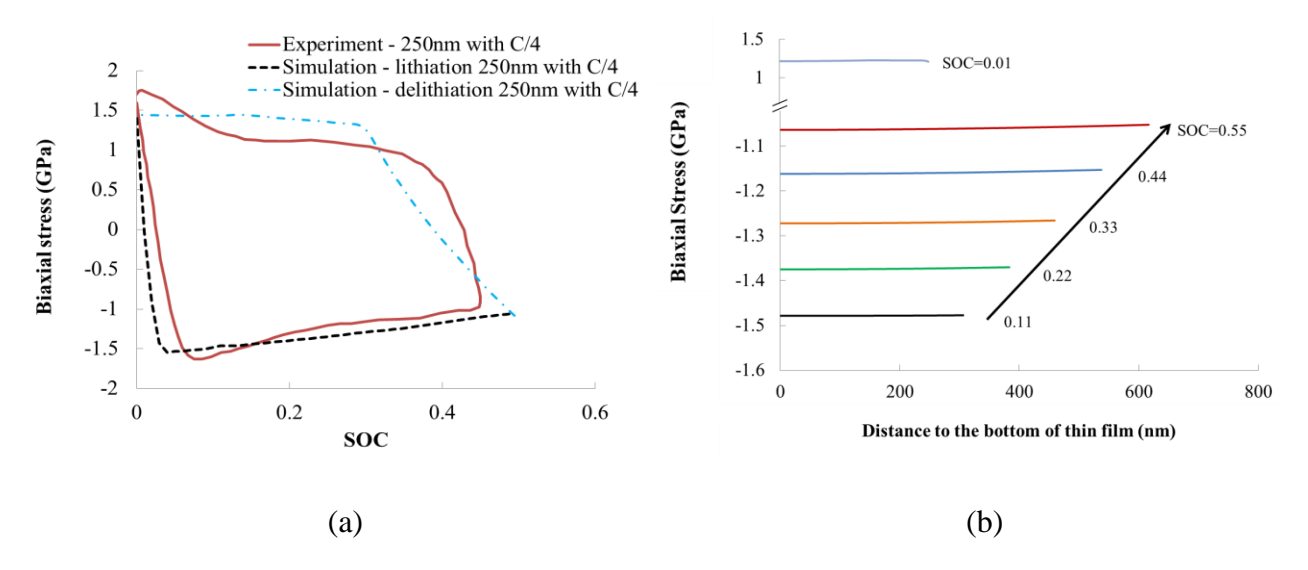


Figure 5.3 Biaxial stress in thin film during cycling of a-Si thin film of 250 nm thickness under C/4 rate were plotted, (a) the stress history vs. SOC was compared with the experimental result was from Sethuraman et al.[60]. In simulations, the lithiation started with a residual stress from delithiation at the same rate; (b) the stress profiles inside the thin film showed that the stress distribution was almost uniform in the film during lithiation.

5.3.2 Si Nanosphere Model

Besides a-Si thin films, the asymmetric rate behavior has not been reported in Si anodes of other geometries, like Si nanosphere[174], hollowed sphere[36], and nanotube[178].

The experiment with Si nanospheres by Liu et al.[174] was investigated here. In Ref. [174], the spheres were encapsulated inside graphite shells. The graphite shells were then bonded with alginate binder to form the anode, as shown in Fig. 5.4(a). Since Si was not in direct contact with an electrolyte, there was no SEI formation on Si surface. The cell with this anode was galvanostatically lithiated and delithiated under the same rate ranging from C/10 to 4C, i.e. following Condition 2. The measured lithiation and delithiation capacities were almost the same,

i.e. symmetric (Fig. 5.4(b)), although the cycling capacity decreased about 80% from C/10 to 4C due to the poor ionic conductivity of the alginate binder[174].

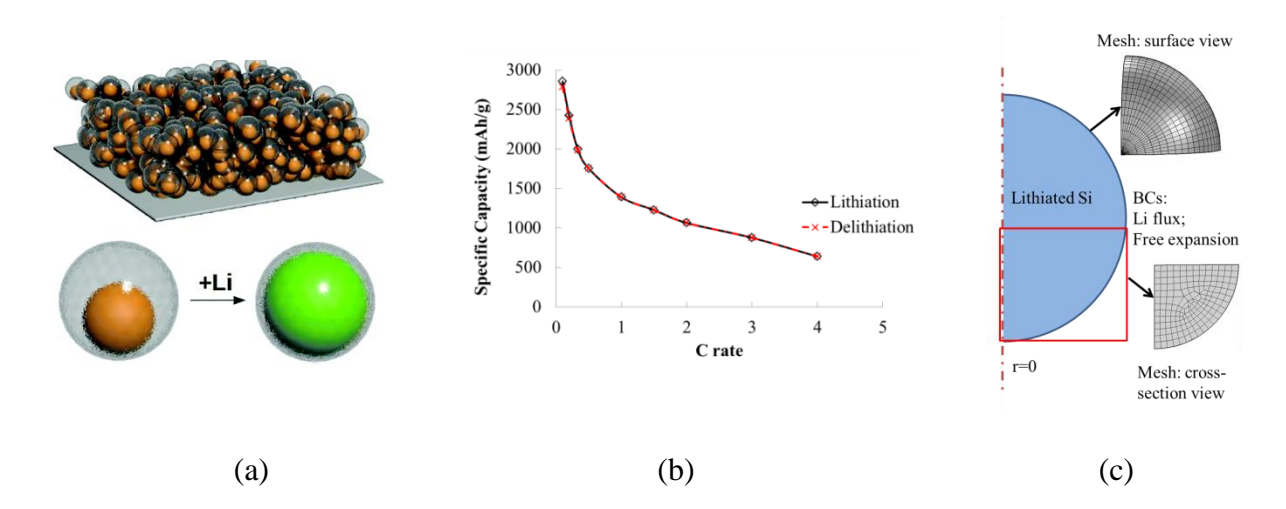


Figure 5.4 (a) The anode with Si nanospheres encapsulated inside graphite shells[174] and (b) its capacity measured under various cycling rates, reproduced from Fig. S8 in Ref. [174]. (c) The FE model and its boundary conditions used in simulations.

In Ref. [174], the average diameter of the spheres was around 100 nm. The void between Si sphere and graphite shell allowed enough room for Si expansion. The *in-situ* transmission electron microscopy (TEM) characterization[174] suggested that the constraint of the graphite shell to the spheres was negligible. The spheres behaved as freestanding structures and grew as having a uniform Li supply at their surface.

Liu's experiment can be simplified as a free-standing single Si nanosphere. The 100 nm sphere was simulated using a 3D model. The sphere was meshed with nearly 20000 elements (for half sphere), with a mix of both hexahedral and tetrahedral elements. The average element size was about 3nm. Fig. 5.4(c) presents a 2D cross section of the 3D model with the boundary conditions and local meshes. A constant current for the corresponding rate was applied to the

particle surface. The sphere was allowed to freely expand upon lithiation/delithiation. In Ref. [174], the initial nanosphere was c-Si but the measurement was performed over a wide range of rates from 0.1C to 4C with more than 10 cycles at each rate. Since c-Si will turn into amorphous phase after the first few cycles[42], the responses in Fig. 5.4(b) can be considered as that of a-Si. Therefore, the Si sphere was modeled as the same material as for the a-Si thin film.

5.4 Results and Discussion

5.4.1 The Rate Behaviors

The simulations for Si thin film and nanosphere were carried out for charging and discharging at C rate between C/10 to 100C under the two conditions. The chemo-mechanical coupling was investigated by varying the coefficient α in Eq. 3.5: α =0 for the case of without the stress effect; and α =0.01 for with the stress effect. To mimic the cut-off voltage in galvanostatic cycling experiment, the lithiation was terminated when the SOC at the geometry surface reached to about 0.83 in lithiation and 0 in delithiation.

To compare with the experimental trends, the predicted specific capacities were plotted vs. C rate for the thin film and nanosphere in Fig. 5.5. In these plots, the solid lines are the results with α =0, and the dashed lines are that with α =0.01. The lithiation and delithiation are represented by triangle and round symbols, respectively. Table 5.3 provides a summary of the remaining capacities at 100C under various conditions in respect to the capacity at 0.1C. In this investigation, 100% capacity is equivalent to SOC=0.83.

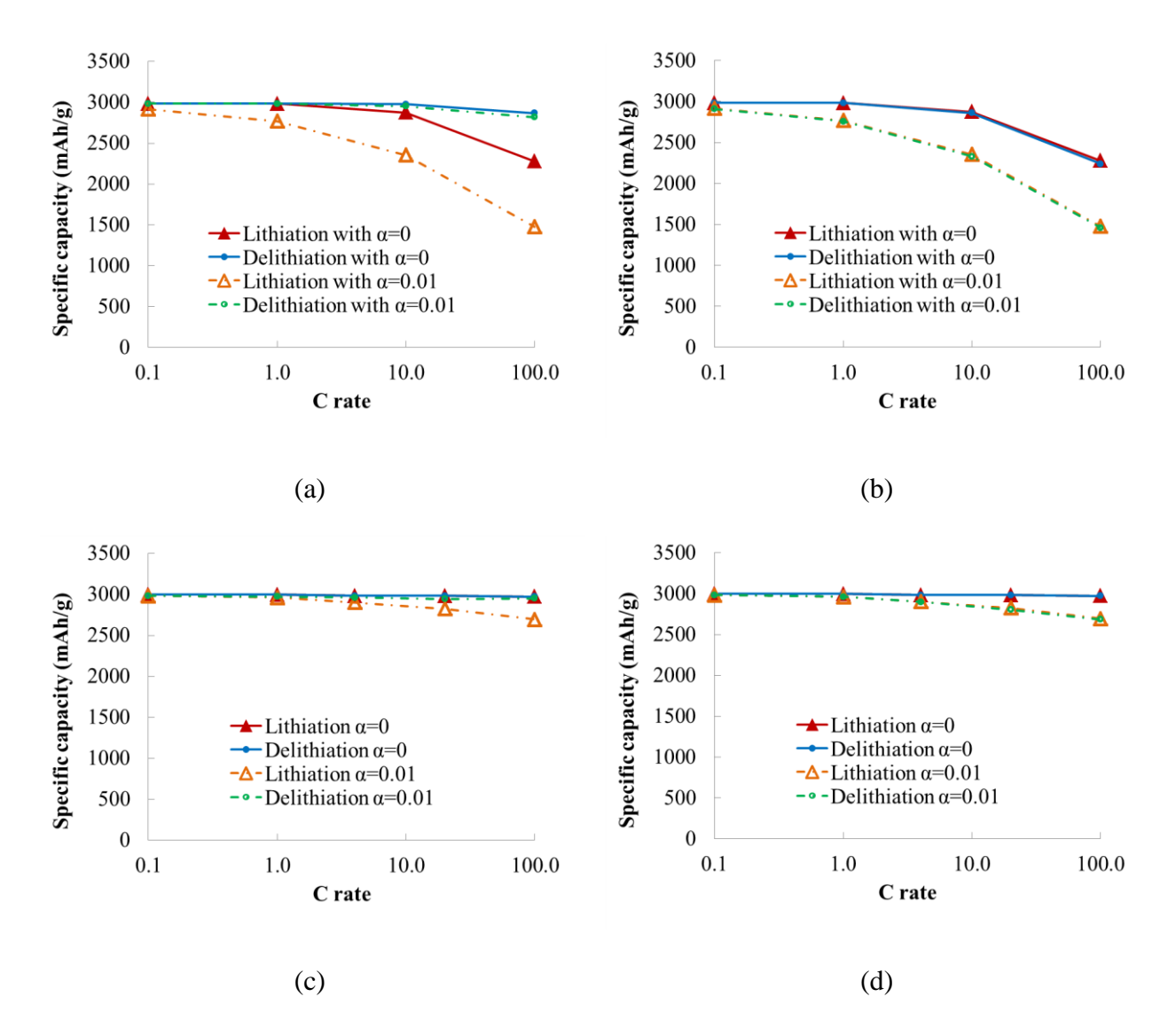


Figure 5.5 The predicted specific capacities vs. C rate for both 70nm a-Si thin film and a single a-Si nanosphere with (α =0.01) and without (α =0) the stress effect (a) thin film under Condition 1; (b) thin film under Condition 2; (c) nanosphere under Condition 1 and (d) nanosphere under Condition 2.

Table 5.3 The specific lithiation/delithiation capacity at 100C in respect of the capacity at 0.1C for the thin film and nanosphere under Conditions 1 and 2.

		100C Lithiation		100C Delithiation	
	α	Condition 1	Condition 2	Condition 1	Condition 2
Thin film	0	76.4%	74.6%	96.1%	74.6%
	0.01	49.5%	47.8%	94.4%	47.3%
Sphere	0	99.7%	99.1%	99.7%	99.1%
	0.01	90.7%	90.2%	99.0%	89.9%

Fig. 5.5 reveals that the asymmetric rate behavior occurs only under Condition 1. For the thin film, the asymmetric rate behavior was pronounced. Over the range of 0.1C to 100C, when α =0, the decrease in capacity was about 23.6% for lithiation and 3.9% for delithiation. With α =0.01, the decrease was 50.5% for lithiation and 5.6% for delithiation. Under Condition 2, both the lithiation and delithiation capacities reduced at a similar pace which resulted in a symmetric rate behavior.

The Si nanosphere displayed a symmetric rate behavior under Condition 1 and under Condition 2 when α =0. However, it showed a small asymmetric rate behavior under Condition 1 with α =0.01. The capacity decreased about 9.3% for lithiation and 1.0% for delithiation.

For Si nanosphere, the predicted decrease in capacity is not as dramatic as that in the experiment as shown in Fig. 5.4(b). This is due to the fact that only one Si nanosphere was simulated and the effect of the binder was not included.

The simulations with chemical-mechanical coupling correctly captured the trends of the rate behavior of these two geometries. To understand why the two geometries displayed distinctly different rate behaviors, the simulation results were analyzed further. Three aspects were investigated: the electrode geometry, the chemo-mechanical coupling and the effect of the prior process.

5.4.2 Electrode Geometry

Under Condition 1, with α =0, the asymmetric rate behavior was observed in the thin film but not in the nanosphere. This result is not related to the chemo-mechanical coupling. A close inspection indicates that the surface limitation associated with the electrode geometry and its boundary constraint is a likely cause, as explained below and Appendix A.

Let us compare a substrate-constrained thin film with a free-standing sphere. In lithiation, the surface area would remain the same for the thin film but increase to $(r/r_0)^2$ times for the sphere $(r \text{ and } r_0 \text{ correspond to the radius of the deformed sphere and the original sphere})$. Under galvanostatic charging, the rate of Li insertion into the electrode remains constant. Furthermore, a sphere has the highest surface/volume ratio among all geometries. As a result, the Li concentration at the surface layer of the nanosphere is much lower than that in the thin film. The lithiation terminates when Li reaching the maximum concentration at the surface layer. This will happen at a much lower charging rate in a thin film than that in a nanosphere if the thickness and the radius of the two are comparable.

5.4.3 Chemo-Mechanical Coupling

Under Condition 1, with α =0.01, the asymmetric rate behavior was much pronounced in the thin film. A small asymmetry was also observed in nanosphere. The results indicate that the chemo-mechanical coupling played a role in the rate behavior.

To understand this process, the profiles of Li concentration (c_1) , hydrostatic stress and the Li flux obtained with α =0 and α =0.01 are compared. Fig. 5.6 and 5.7 present the results at 100C during lithiation/delithiation for the thin film and nanosphere, respectively. For the thin film, the profiles were plotted against the instantaneous thickness measured from the substrate to the top surface of the film at selected time intervals. For the sphere, they were plotted against the

instantaneous radial distance from the center to the surface. The solid lines are for α =0 and the dash lines for α =0.01. The Li flux was calculated according to Fick's first law as $\mathbf{N} = -D_1 c_1 \nabla \mu_{Li_xSi}(\mathbf{\sigma})/RT$.

5.4.3.1 Thin film

During lithiation, the hydrostatic stress in the thin film changed quickly from a tensile residual stress resulted from the prior slow delithiation to a large compressive stress, as in Fig. 5.6(c). The Li concentration profiles at different time had similar shapes and the curves moved up steadily with time (Fig. 5.6(a)). The compressive stress suppressed the Li diffusion. With the stress effect, the driving force for Li diffusion and the flux reduced, the Li concentration gradient increased. With the progress of lithiation, the difference between α =0 and α =0.01 increased. The process terminated when the maximum SOC was reached at the surface of the film. The predicted termination time was 27.5s and 17.8s, corresponding to a capacity retention of 76.4% and 49.5% for α =0 and α =0.01, respectively.

In delithiation, the hydrostatic stress changed from compression to tension, in Fig. 5.6(d). Unlike in lithiation where the stress transition took less than 2s, the transition in delithiation took about 10s and 15s to propagate through the thickness of the film for α =0 and α =0.01, respectively. With α =0.01, the stress profiles had a steeper slope, and the Li flux had a steep step over the transition region. A stress profile that was tensile at the surface and compressive at interior resulted in a large Li concentration gradient in the film. When the stress in the film fully converted to tensile, the Li concentration gradient reduced, as seen in Fig. 5.6(b). Towards the end of delithiation, the Li concentration profiles for the two cases were very close. The process terminated at 34.6s and 34.0s, corresponding to a capacity retention of 96.1% and 94.4% for α =0

and α =0.01, respectively. The results show that although the profiles differed significantly, the chemo-mechanical coupling had a relatively small effect on the overall delithiation capacity.

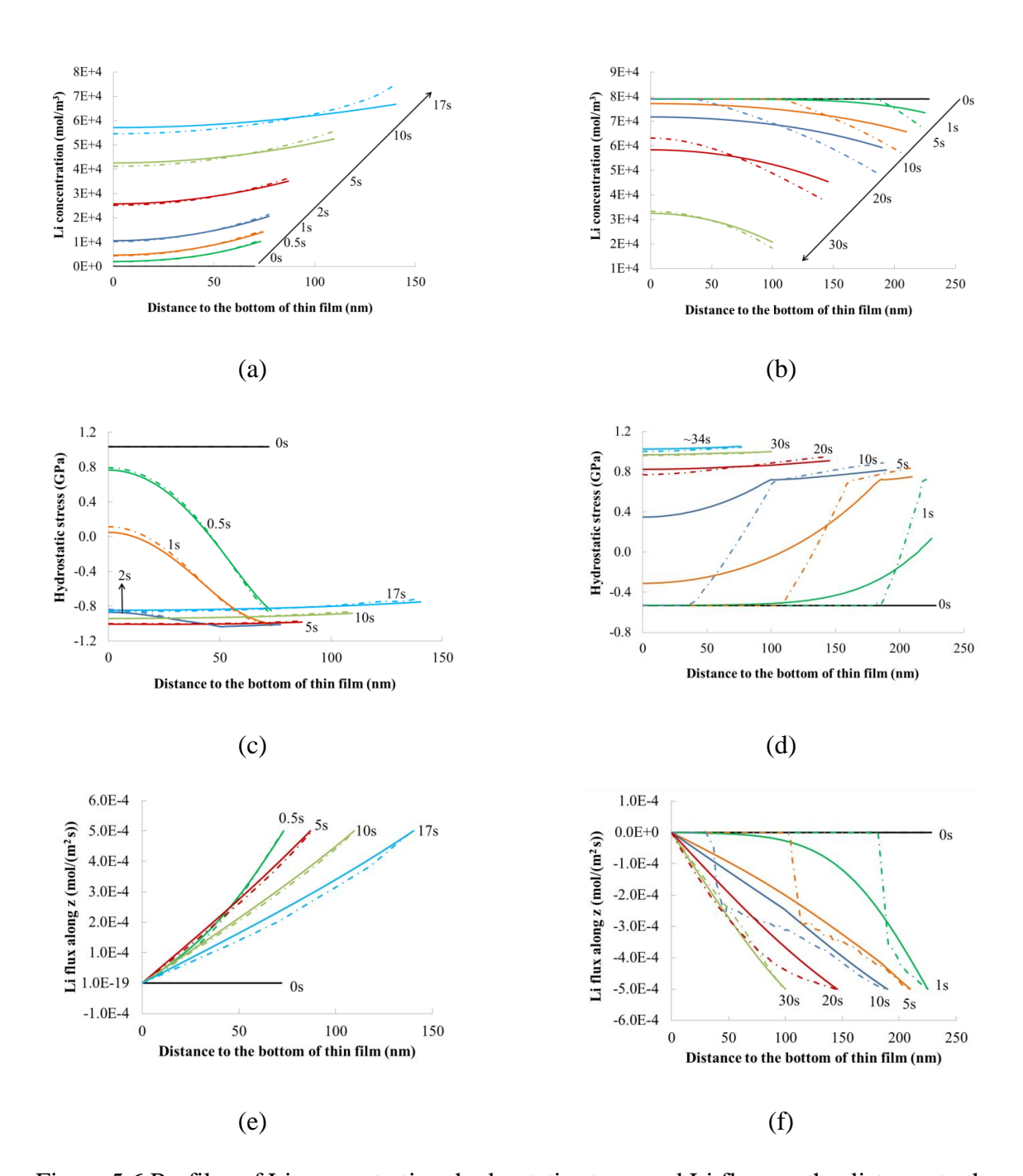


Figure 5.6 Profiles of Li concentration, hydrostatic stress and Li flux vs. the distance to the bottom of the thin film at 100C under Condition 1. Solid line for without (α =0) and dash line for

Figure 5.6 (cont'd): with the stress effect (α =0.01). (a) and (b) plot the Li concentration; (c) and (d) plot the hydrostatic stress; (e) and (f) plot the Li flux N_z . (a)(c)(e) are under 100C lithiation and (b)(d)(f) are under 100C delithiation.

5.4.3.2 Nanosphere

The Li concentration, hydrostatic stress and Li flux profiles in the nanosphere were quite different from those in the thin film. The tensile and compressive hydrostatic stress always co-existed in the sphere. During lithiation, it was compression at the surface and gradually changed to tensile at the core (Fig. 5.7(c)). It was vice versa for delithiation (Fig. 5.7(d)). The stress profile in lithiation suppresses the Li transport at the surface layer but enhances it in the core area. It is vice versa in delithiation. As a result, the Li distribution was much more uniform across the sphere as compared to that in thin film, as in Fig. 5.7(a) and (b). Furthermore, the Li flux at the surface of the sphere was not a constant. It reduced with lithiation and increased with delithiation as the surface area varied, as discussed in section 4.2 and presented in Fig. 5.7(e) and (f).

Comparing the cases of α =0 and α =0.01, the stress and Li flux profiles differed but the Li concentration profiles were almost identical with the exception towards the end of lithiation and at the beginning of delithiation where the profiles for α =0.01 were steeper. As shown in the case of thin film, a steeper Li distribution towards the end of a process reduced the capacity. The lithiation capacity was affected. The value was 99.7% and 90.7% for α =0 and α =0.01, respectively. The delithiation capacity was almost unaffected. The values were 99.7% and 99%, respectively.

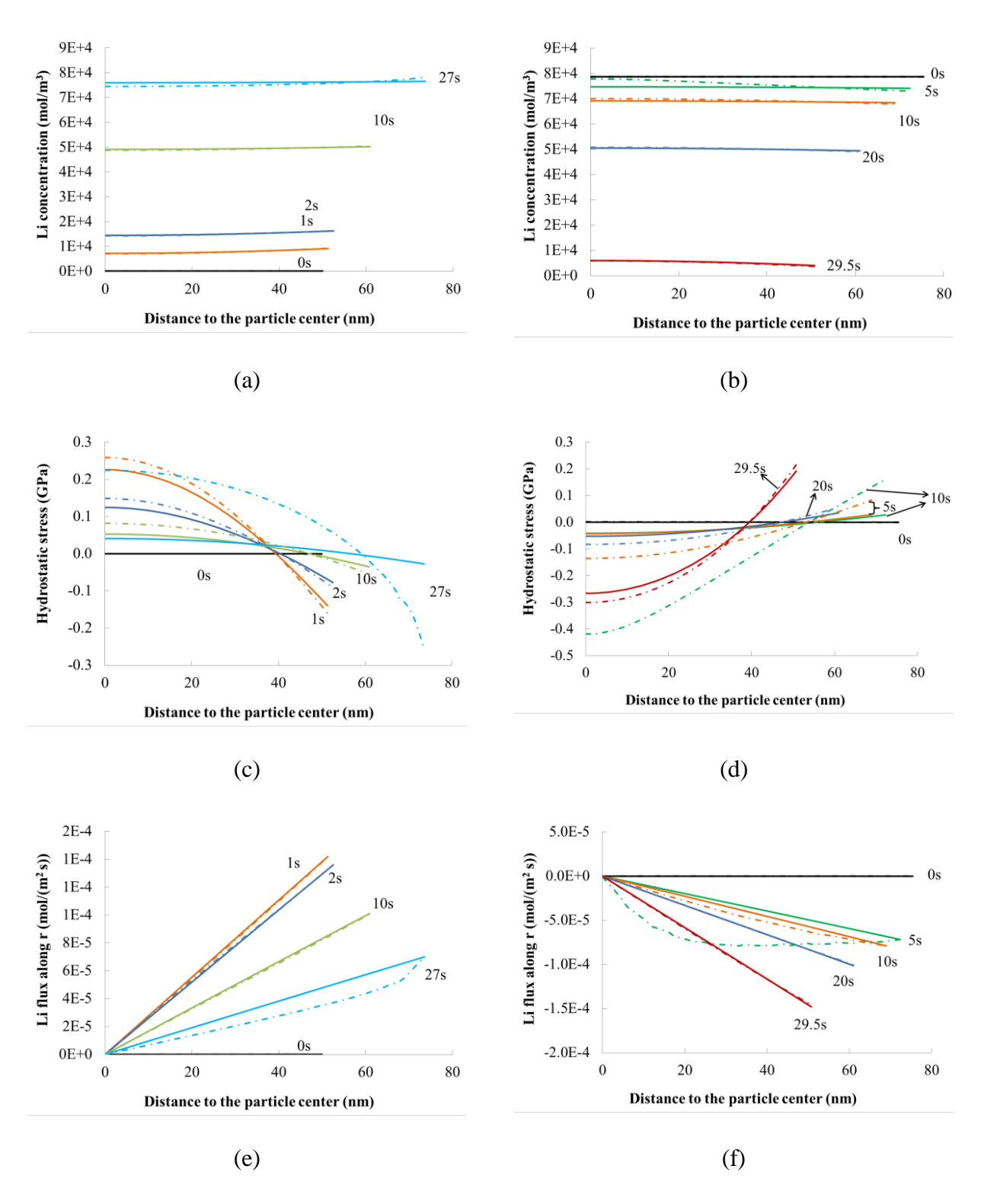


Figure 5.7 Profiles of Li concentration, hydrostatic stress and Li flux vs. the radial distance for the sphere at 100C under Condition 1. Solid line for without (α =0) and dash line for with the

Figure 5.7 (cont'd): stress effect (α =0.01). (a) and (b) plot the Li concentration; (c) and (d) plot the hydrostatic stress; (e) and (f) plot the Li flux N_z . (a)(c)(e) are under 100C lithiation and (b)(d)(f) are under 100C delithiation.

The above results show that the stress profiles in the two geometries play an important role in their rate behavior. During lithiation, a compressive hydrostatic stress exists throughout the thin film. In a sphere, it is only in the surface layer. Although Li transport was suppressed at the surface for both cases, the stress profile in the sphere promoted a more uniform Li distribution. The stress profile together with the electrode geometry discussed in section 5.4.2 provided a better lithiation capacity for a Si nanosphere than that for a Si thin film.

During delithiation, the stress profiles were vice versa to that of lithiation. A tensile hydrostatic stress promotes the Li transport. As shown in Fig. 5.6 and 5.7, under Condition 1, the chemo-mechanical coupling had a very small effect on the delithiation capacity of the two geometries. Again, the stress profile in the sphere favored a more uniform Li distribution. The condition that resulted in a larger nonuniform Li distribution towards the end of the process reduced the overall capacity.

5.4.4 Effect of Prior Process

The asymmetric rate behavior occurred only under Condition 1. The results indicate that the prior process has an effect on the capacity of the electrode in the next step. It was suspected that the residual stress from the prior process might have played a role. To investigate this effect, the Li concentration and the hydrostatic stress profiles for the thin film at 100C with α =0.01 under the two conditions were compared in Fig.5.8.

As seen from the profiles at t=0s, Condition 1, a slow process, resulted in a nearly uniform Li distribution, whereas Condition 2, a fast process, resulted in a nonuniform Li distribution through the thickness of the thin film.

For lithiation, the stress profiles at t=0s by the two conditions were very close, both were tensile and had a uniform distribution. During lithiation, although the stress gradient for Condition 2 was higher initially, the stress profiles of the two conditions became indistinguishable after 5s. As the lithiation progressed, the Li profiles of the two conditions became closer. As discussed above, the Li profile toward the end of a process appears to determine the lithiation capacity. The retaining capacity was 49.5% and 47.8% for Conditions 1 and 2, respectively.

For delithiation, the stress profiles of the two conditions differed significantly. At t=0s, although both were compressive, the one for Condition 1 was uniform whereas the other had a gradient. At later time intervals, the shapes of the profiles between the two conditions had some similarity but the curves remained apart. Nevertheless, a closer inspection reveals that the difference in the delithiation capacity between the two conditions was originated from their initial SOC, rather than the residual stress. The Condition 1 resulted in a complete charged state (SOC=0.83) whereas Condition 2 resulted in a partially charged electrode (SOC=0.41), corresponding to 100% and 47.8% of the capacity, respectively. The delithiation capacities for the two conditions were 94.4% and 47.3%. These values correlated well with the amount of Li initially in the electrodes. The same phenomenon was observed for the nanosphere. The delithiation capacity 89.9% at 100C under Condition 2 can be traced back to its initial SOC which was at 90.2% of the capacity.

Based on these results, we conclude that the reduction in delithiation capacity under cyclic charge/discharge is related to the lower SOC in the electrode.

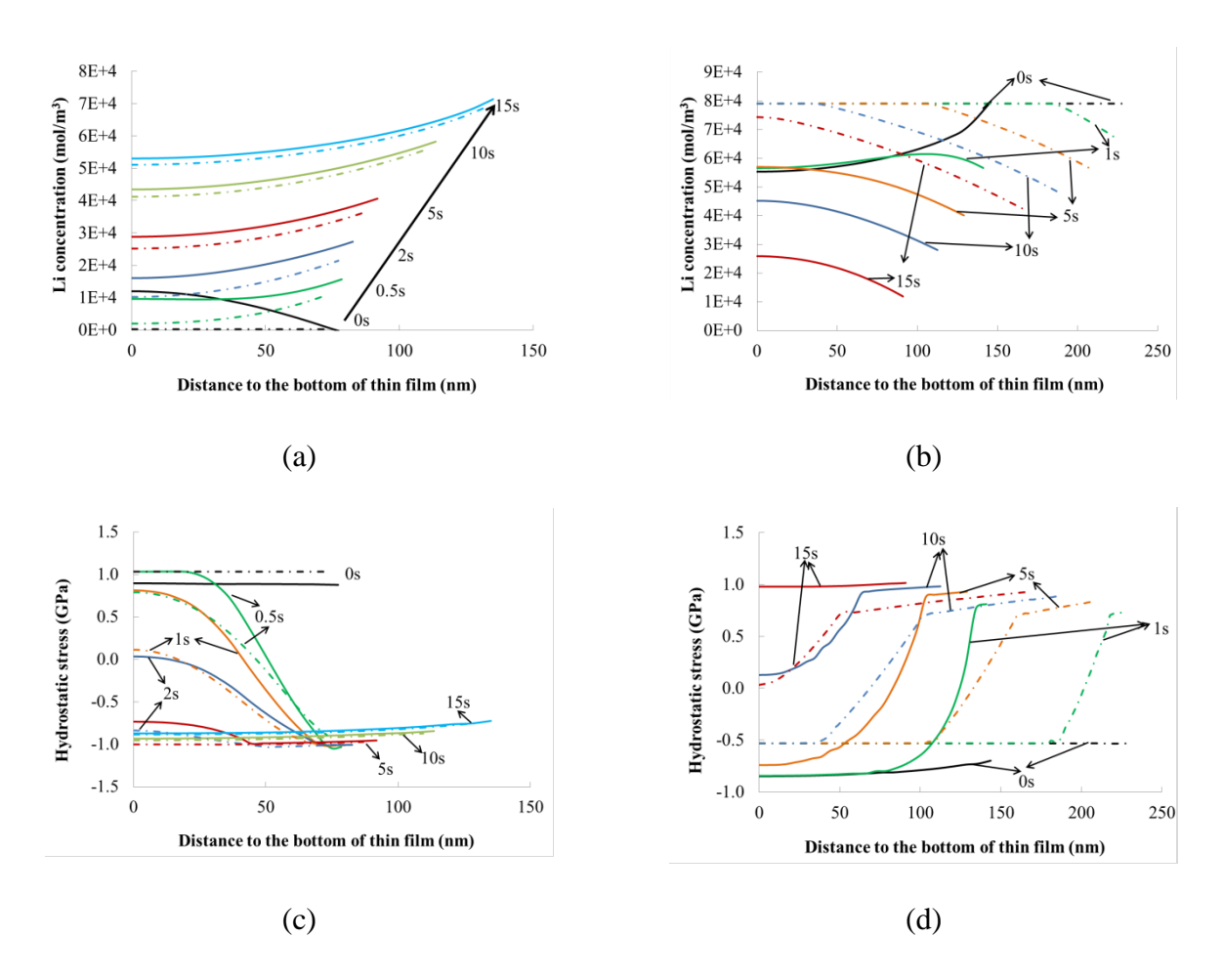


Figure 5.8 Profiles of Li concentration and hydrostatic stress vs. the distance to the bottom of the thin film at 100C with α =0.01 under Condition 1 (dashed line) and Condition 2 (solid line). (a) and (b) are Li concentration; (c) and (d) are hydrostatic stress. (a) and (c) are under 100C lithiation; (b) and (d) under 100C delithiation.

Besides the voltage shift introduced by the Ohmic resistance, Li et al.[173] pointed out that the stress may also contribute to the asymmetric rate behavior of the thin film by affecting the Li diffusivity. The current study confirms that the stress is indeed an important factor contributing

to the asymmetric rate behavior. In future work, the chemo-mechanical coupling will be incorporated into a multiphysics battery model to consider other effects such as electrochemistry, kinetics, temperature, charge transport in other battery components, and etc.[133,154,161].

It is worth pointing out that, although we only model the amorphous Si structures as the crystalline Si is usually amorphized in the first lithiation and remains as amorphous phase in later cycles[42], this model could be developed to consider the two-phase lithiation of crystalline Si in the first lithiation, and also could be revised to study other high capacity electrodes which inherent high deformations under lithiation, such as sulfur cathode and tin anode, etc.

5.5 Conclusion

The chemo-mechanical coupling of Si lithiation was investigated using finite element analysis with a model that incorporates the stress effect into the diffusion equation through influencing the chemical potential of Li in Si. The coupled diffusion and deformation problem was solved in COMSOL Multiphysics[®].

The model was examined in the simulations of two geometries: a-Si thin film and a-Si nanosphere. In experiments, a strong asymmetric rate behavior has been observed in a-Si thin film such that the decrease in capacity with increasing the C rate was much faster in lithiation than that in delithiation. However, such a behavior has not been reported for other geometries. FEA simulations captured the asymmetric rate behavior of a-Si thin film and the symmetric rate behavior of Si nanospheres. The simulation results revealed that both the electrode geometry and the chemo-mechanical coupling played important roles in the asymmetric rate behavior.

The lithiation of a substrate-constrained Si film is more likely to become surface limited than other geometries due to its low surface/volume ratio and constant surface area. Furthermore, such a thin film is mostly under compression during lithiation. The compressive hydrostatic

stress suppresses the Li diffusion. The two factors result in a significantly lower lithiation capacity. In delithiation, the stress reverses to tension which promotes Li diffusion. The simulations show that the delithiation capacity was almost unaffected by the discharging rate. The large differential rate dependence in charge and discharge contributes to the strong asymmetric rate behavior of the thin film.

A free standing nanosphere has an increasing surface area with volume expansion and hence is less likely to become surface limited in lithiation. In a sphere, the tensile and compression stresses always co-existed. The stress suppressed and enhanced diffusion happened simultaneously at different radial distances across a sphere. This profile promotes a uniform Li distribution. The nanosphere is less likely to suffer capacity reduction with increasing the rate.

The delithiation capacity of the two geometries is affected very little by the electrode geometry and the chemo-mechanical coupling. However, the delithiation capacity is limited by the amount of Li available in the electrode. Therefore, under cyclic charging/discharging condition, the delithiation capacity decreased at the same pace as that of lithiation. The asymmetric rate behavior was absent. On the other hand, a slow lithiation process will lead to a better retained delithiation capacity at higher rates.

Chapter 6 A Microstructure-Resolved Multiphysics Model for Li-ion Battery Si Anode 6.1 Introduction

Although with an ultra-high theoretical capacity, the capacity of the a-Si anode that can be actually realized in a LIB is related to its shape, packing, electrical pathway, and Li transport in the electrolyte and in the active materials. The design options are numerous, as discussed in 1.1. A composite Si anode will bring in additional flexibility and another level of complexity. The ability to find the best combinations through computation-guided optimization can drastically accelerate the process of bringing a promising novel nanostructure into products. Such optimizations require a multiphysics microstructure-resolved model (MRM) for LIB cell. The model should include the electrochemical reaction, Li transport in electrolyte and electrodes, electrical connectivity, dimensional changes, stresses, and the coupling relationships.

Multiphysics numerical models have been used in LIB research, such as coupled thermal-electrochemical model for the investigation of thermal response[133–135], coupled electrochemical-mechanical model for the study of stress and deformation of the electrode particles and battery components[136], microstructure resolved multiphysics models[132,137,140,179–181] and multiscale coupled electrical/electrochemical-thermal-mechanical models for the prediction of mechanical crush introduced short circuit and thermal responses of LIBs[182,183]. All these models were for LIBs with graphite anodes.

The objective of the current work is to incorporate Si anodes in these models. Si anode presents new challenges for numerical models, including the numerical issues in considering mass balance with finite deformation[23], the uncertainty in some key properties for Si anodes[23,24], and the modeling of electrolyte and its interaction with other cell components. In previous Chapters, we have investigated the modeling of Li diffusivity in amorphous Si (a-

Si)[115], chemo-mechanical coupling[155] of Li_xSi, and the mass balance with finite deformation[115,155] separately using models that only consist of a-Si anode. The current work is focused on a LIB cell.

This chapter presents a model for a half cell configuration consisting of a-Si anode and Li metal reference electrode. The model has been implemented in COMSOL, a Multiphysics Finite Element (FE) package. This paper is organized as follows. In section 6.2-6.3, the model setup and model parameters are presented. Key properties (reaction rate constant and apparent transfer coefficient) are investigated by correlating with experiments with Si nanowire anode at various C rates. In section 6.4, the model is used to examine a-Si thin film anode for validation. In section 6.5, a parameter study is performed for half cell with Si nanowalls anode.

6.2 Model Description

The model development is described in detail in Chapter 3 previously. The governing equation was categorized in Table 6.1 for MRM model for both "battery" and "stress" submodels. For computational efficiency, a two-dimensional (2D) MRM model has been developed first. The methodology developed for 2D model can be extended to a three-dimensional (3D) model. The model described below is for implementation in COMSOL. The model used the following COMSOL modules: General Form Partial Differential Equation (PDE) module, Nernst-Planck (CHNP) module, Electric Currents (DC) module and Fluid-Structure Interaction (FSI) module.

Table 6.1 Governing equations for cell model in Chapter 6 (Symbols are in Nomenclature).

Physics	Governing Equations				
"Battery" sub-model	S 1				
Mass Balance					
(1) Li Diffusion in Si	$\frac{\partial c_1}{\partial t} + \nabla \cdot \left(-\frac{D_1}{RT} c_1 \nabla \mu_{Li_x Si}(\boldsymbol{\sigma}) \right) = 0$	(3.1)			
	$\mu_{Li_xSi}(\mathbf{\sigma}) = \mu_{Li_xSi} + \Delta\mu_{Li_xSi}(\mathbf{\sigma})$	(3.3)			
	$\mu_{Li_xSi} - \mu_{Li} = -nFU$	(3.6)			
	$\Delta\mu_{Li_xSi}(\boldsymbol{\sigma}) = \alpha \Omega \sigma_h$	(3.5)			
(2) Ionic Transport in Electrolyte	$N_{+} = \left(-D_{2} + \frac{2k_{2}t_{+}t_{-}RT}{c_{+}z_{+}F^{2}}\right)\left(1 + \frac{\partial \ln f_{+}}{\partial \ln c_{2}}\right)\nabla c_{+} - \frac{k_{2}t_{+}}{z_{+}F}\nabla \phi_{2}$	(3.7)			
·	$N_{-} = \left(-D_{2} + \frac{2k_{2}t_{-}^{2}RT}{c_{-}z_{-}F^{2}}\right)\left(1 + \frac{\partial \ln f_{\pm}}{\partial \ln c_{2}}\right)\nabla c_{-} - \frac{k_{2}t_{-}}{z_{-}F}\nabla \phi_{2}$	(3.8)			
Change Palance					
Charge Balance (1) Fluid	$2PTh \left(\begin{array}{c} \partial \ln f \end{array} \right)$				
Electrolyte	$\mathbf{i}_2 = -k_2 \nabla \phi_2 + \frac{2RTk_2}{c_2 F} \left(1 + \frac{\partial \ln f_{\pm}}{\partial \ln c_2} \right) (1 - t_{\pm}) \nabla c_2$	(3.9)			
(2) Si anode	$k_1 \nabla \phi_1 = -\mathbf{i}_1$	(3.10)			
(3) Current	$k_c \nabla \phi_c = -\mathbf{i}_c$	` ′			
Collector		(3.11)			
Electrochemical Interface	$i_{1,2} = -i_{Si} \left\{ \exp \left(\frac{\alpha_a \eta F}{RT} \right) - \exp \left(\frac{(-\alpha_c) \eta F}{RT} \right) \right\}$	(3.15)			
	$i_{Si} = Fk_0c_2^{\alpha_a}(c_{theory} - c_{surf})^{\alpha_a}c_{surf}^{\alpha_c}$	(3.17)			
	$\eta = \phi_1 - \phi_2 - U$	(3.18)			
	$N_{_{+}}=-i_{1,2}/F$	(3.19)			
		, ,			
"Stress" Sub-model					
Si Deformation	$\mathbf{F} = \mathbf{F}_{el}\mathbf{F}_{inel} = \mathbf{F}_{el}\mathbf{F}_{p}\mathbf{F}_{c}$	(3.22)			
	$\frac{V}{V_0} = \det(\mathbf{F}_c) = 1 + \Omega \Delta c$	(3.23)			
Stress in Si	$\mathbf{\sigma} = J^{-1}\mathbf{F}\mathbf{S}\mathbf{F}^{\mathbf{T}}$	(3.30)			
	$\mathbf{S} = \mathbf{S_0} + 2\frac{\partial W_s}{\partial \mathbf{C}}$	(3.31)			
		(3.32)			
Fluid Electrolyte	$W_s = \Lambda \operatorname{tr}(\mathbf{E})^2 + M \operatorname{tr}(\mathbf{E}^2)$	(3.34)			
Motion Electrosyste	$\rho_{\text{fluid}} \left(\frac{\partial \mathbf{v}_{\text{fluid}}}{\partial t} + \mathbf{v}_{\text{fluid}} \cdot \nabla \mathbf{v}_{\text{fluid}} \right) = -\nabla p + \mu_{\text{fluid}} \nabla^2 \mathbf{v}_{\text{fluid}}$	(3.34)			

6.3 Model Parameters

In addition to the model parameters listed in section 3.3, there are more parameters that should be determined based on the target system and theories adopted. Therefore, the following parameters needed in the MRM model are described below.

6.3.1 Chemical Potential

The OCP has been measured by Sethuraman et al. through a series of ten-hour relaxation experiments performed on a 140 nm porous a-Si thin film[118]. The results are replotted in Fig. 6.2(a), where the red dots were from lithiation and blue dots were from delithiation of Si with the state of charge (SOC) changing from 0.03 to 0.8. The OCP value at SOC=0 equals to the theoretical potential difference between Li and Si, and the value reduces to 0V when SOC=1[184]. Based on these observations, the OCP as a function of the SOC is established, as shown by the black curve in the Fig. 6.1(a). Based on Eq. 3.6, the chemical potential μ_{Li_xSi} as a function of SOC is calculated, as presented in Fig. 6.1(b).

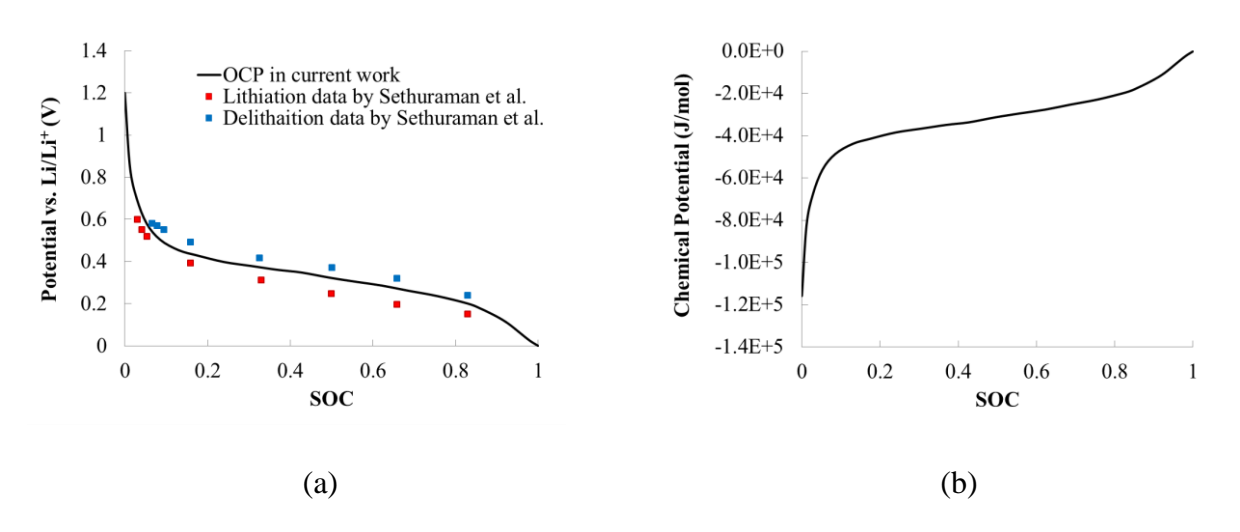


Figure 6.1 (a) The relaxation potential of lithiated Si during lithiation and delithiation from Sethuraman et al.[118] and the OCP curve used in the current work. (b) The chemical potential derived from extrapolated OCP curve using Eq. 3.6.

6.3.2 Li Diffusivity in a-Si

The Li diffusivity in Si was determined through correlating numerical simulations with the *in-situ* lithiation experiments of Si nanospheres by McDowell et al.[42], as presented in Ref. [115]. The Li diffusivity in single phase lithiation of Si is found to be in the range of 3×10^{-16} m²/s with the chemical potential as the driving force for lithiation (Eq. 3.2 and 3.6) instead of the concentration gradient in Ref. [115] (Eq. 3.1). It is an averaged value without the consideration of Li concentration-dependency and stress effect. In this study, $D_1 = 3\times10^{-16}$ m²/s is used in Eq. 3.2 for single phase lithiation.

6.3.3 Electrolyte Properties

The experiments to be simulated in this work used two electrolyte systems, as listed in Table 6.1. Literature data showed that the ionic conductivity of different electrolyte system varies in a similar range[131,133,185–187], and the solvent ratio had a negligible impact on the performance of the cell[188,189]. Since the ionic conductivity k_2 for the two systems in Table 6.2 were not available, k_2 was assumed to follow the relationship for 1 M LiPF₆ in EC/DMC (2:1 vol.%)[137], as shown in Fig. 6.2.

Table 6.2 Electrolyte systems used in chosen experiments

Experiments	Electrolyte system
Nanowire [30]	1 M LiPF ₆ in 1:1 (vol%) EC:DEC
Thin film [60]	1.2 M LiPF ₆ in 1:2 (vol%) EC:DEC with 10% FEC additive

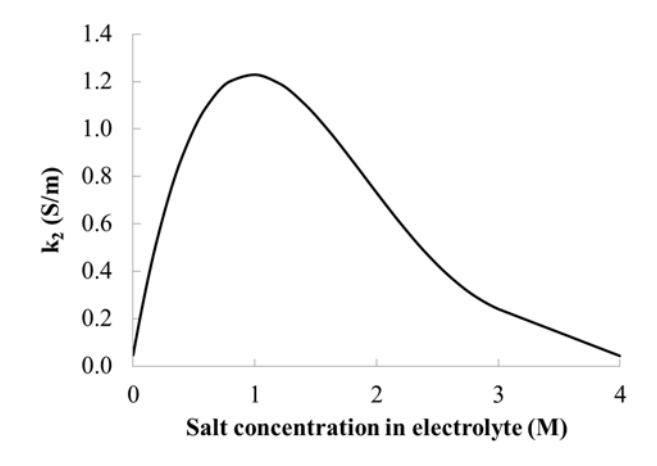


Figure 6.2 The ionic conductivity k_2 as a function of the salt concentration of LiPF₆ in EC:DMC (2:1 vol.%)[131].

Table 3.1 presents a summary of the parameter values used in the current model. For Si, the apparent transfer coefficient (α_a and α_c) in Butler-Volmer equation (Eq. 3.15) and reaction rate constant k_0 in Eq. 3.17 and have not been well established. The values of these parameters are labeled as to be determined (TBD) in Table 3.1, and they will be determined by simulating a Liion cell with Si nanowires experiment of Zhang et al.[30] to be presented next.

6.3.4 Determine the Reaction Rate Constant and Apparent Transfer Coefficient

The current density at the Si-electrolyte interface is determined by the Butler-Volmer equation, Eq. 3.15-3.17, where the key parameters are k_0 , α_a and α_c . For systems with a charge transfer number n=1, $\alpha_a + \alpha_c = 1[139]$. Table 6.3 provides a summary of the values of these parameters reported in literature, where they were determined by fitting the experimental data with Si continuum models[63,138,190] or analytical solution[118,191] for various Si anodes, like a-Si thin film[63,118,192], polycrystalline Si thin film[191,193], and Si composite[138,190]. As shown in Table 6.3, these values varied a great deal. This may be due to the wide range of

experimental techniques and conditions used in these investigations. There is a need for standardization in these measurements.

Table 6.3 Comparison of reaction rate constant, exchange current density and apparent transfer coefficient between literature and current work.

Reference	Reaction rate constant (m/s)(mol/m ³)- ^{αa}	Exchange current density (A/m²)	Apparent transfer coefficient	System used	Experiment technique
Baggetto et al. [191,193]	-	10	$\alpha_a = 0.26; \ \alpha_c = 0.74$	70 nm polycrystalline Si thin film; LiPON solid-state electrolyte	Butler-Volmer fitted GITT
Li et al. [192]	-	1.3	-	100 nm a-Si thin film; 1M LiPF ₆ in EC/DMC (1:1)	Analytical solution fitted PITT
Swamy et al.[194]	-	1	-	500 μm c-Si wafer; 1M LiPF ₆ in EC/DMC (1/1 wt%) + FEC (10 wt %) + VC (2 wt%)	EIS
Sethuraman et al. [118]	1×10 ⁻¹⁴ (estimated)	10 ⁻⁹ (in OCP relaxation)	$\alpha_a = 1.77 \text{SOC} + 1.65$ $\alpha_c = 0.63 \text{SOC} + 1.52$	Porous 300 nm c-Si thin film; 1.2M LiPF ₆ in 1:2 (vol.%) EC/DEC	A Tafel equation fitted OCP relaxation
Bucci et al. [63]	$2.5-10\times10^{-8}$	10^{5}	$0 < \alpha < 1$, values were not provided	100 nm a-Si thin film; 1M LiPF ₆ in EC/DEC/DMC (1:1:1)	1D electrochemical model fitted cell voltage
Chandrasekara n et al. [190]	1×10 ⁻¹⁰ - 2.5×10 ⁻⁹	10-2	$\alpha_a = 0.5 - 0.8$ $\alpha_c = 0.5 - 0.2$ $\alpha_c + \alpha_a = 1$	silicon composite electrode; 1M LiPF ₆ in EC/DEC/DMC (1:1:1)	Single Si particle model fitted GITT
Chandrasekara n et al. [138]	10 ⁻¹³ (assumed)	10 ⁻²	$\alpha_c = \alpha_a = 0.5$	Si composite electrode; no certain electrolyte system used	1D cell continuum model fitted cell voltage
Pal et al. [128]	1.5-60×10 ⁻¹³	-	$\alpha_c = \alpha_a = 0.5$	250 nm a-Si thin film; No electrolyte given	2D electrochemical model fitted cell voltage
This work	8×10 ⁻¹⁵	10 ⁻³	$\alpha_a = 0.7; \ \alpha_c = 0.3$	Si nanowires; LiPF ₆ in EC:DMC (2:1 vol.%)	2D MRM model fitted cell voltage

In the current work, k_0 , α_a and α_c were determined by correlating simulations with the experiment by Zhang et al. [30]. In Ref. [30], half cells with Si nanowires were galvanostatically cycled under C rates ranging from C/20 to 1C and the cell voltage against cell capacity was measured for cycles after the first cycle. Each C-rate was measured with a different cell. To compare with simulations, the measured cell capacity was converted to SOC and plotted in Fig. 6.3(b). The SOC decreased about 40% when the C rate increased from C/20 to 1C. The SEM observation showed that individual nanowire is a standalone structure with minimal contact with other cell components, in good contact with the stainless steel current collector, and remain intact without fracture during cycling. Therefore, the decrease of capacity with C rate was not due to mechanical failure but the characteristic response of the cell. This experiment serves as a good study case.

To simulate this experiment, a 2D plane strain FE model was built, as shown schematically in Fig. 6.3(a). In experiments, the nominal diameter of the nanowire is 90 nm and the length is in the range of micrometers, which results in a large aspect ratio (length/diameter). In the FE model, the nanowire was simulated with an aspect ratio of 30. Besides the constraint by the current collector at the bottom, the nanowire was surrounded by a large amount of fluid electrolyte which provides sufficient supply of Li. The model geometry is set as in Table 6.4.

Table 6.4 Model dimensions used in the Si nanowire model

Quantity	Si Nanowire	Current Collector	Li Electrode	Electrolyte
Height (µm)	2.7	2	1	5.3 ^a
Width (nm)	90	1000	1000	1000

a. Height of electrolyte is measured from top of Si nanowire to bottom of Li electrode

By adjusting the value of the parameters and correlating the cell voltage at various C rates with the experimental curves, the parameter set that produced the best fit to the experimental curves was determined as $k_0 = 8 \times 10^{-15}$ (m/s) (mol/m³)^{-0.7}, α_a =0.7 and α_c =0.3. Fig. 6.3(b) compares the cell voltage vs. SOC plots obtained in the experiment with the simulation results using this set of parameters. As seen, the predicted curves (solid lines) were in reasonable agreement with the experimental data (markers) under C rates from C/5 to 1C. This set of parameters is presented in the last row in Table 6.3. Compared to literature data, the value of k_0 is at the same order as that reported by Sethuraman et al.[118]. The trend of $\alpha_a > \alpha_c$ and the range of the values agreed with that reported by Chandrasekaran et al.[190]. Trial runs with symmetric apparent transfer coefficients $\alpha_a = \alpha_c = 0.5$ have also been tested and the resulted cell voltage locus is always symmetric to the OCP, which differ from the experimental trend.

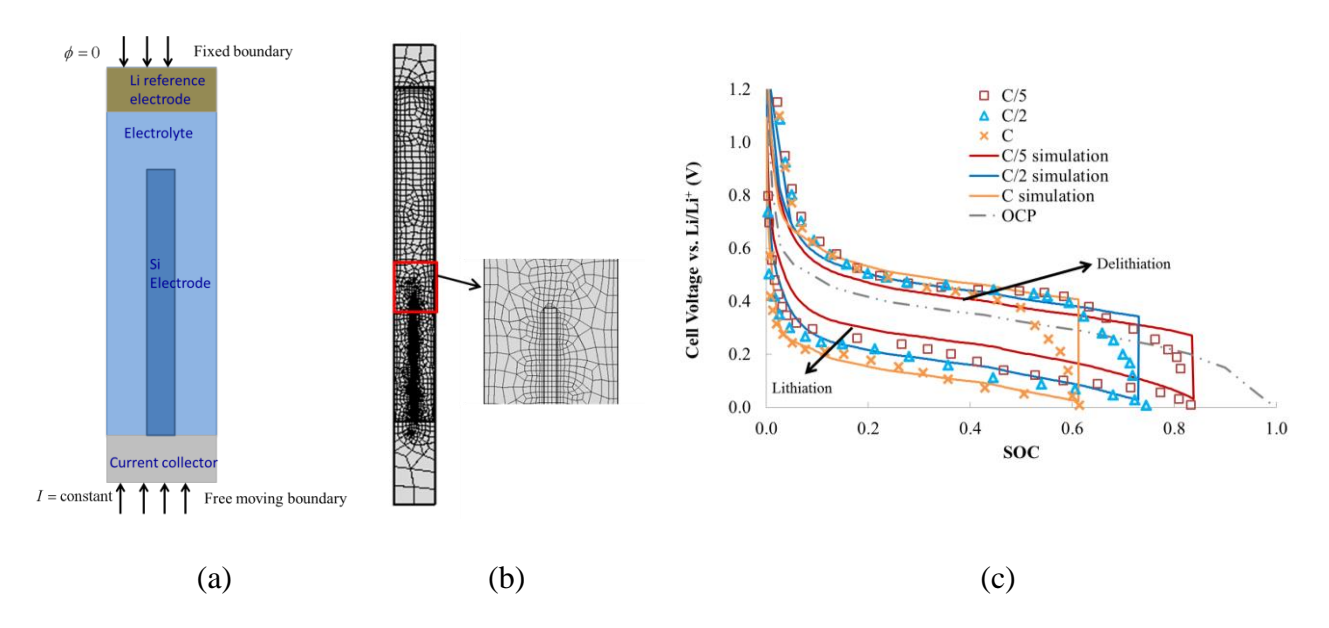


Figure 6.3 (a) The schematic of cell model with Si nanowire and (b) the mesh. (c) Comparisons of the cell voltage vs. SOC curves obtained by simulations with $k_0 = 8 \times 10^{-15}$ (m/s) (mol/m³)^{-0.7}, α_a =0.7 and α_c =0.3 (solid lines) and the experimental results (markers) by Zhang et al.[30].

6.4 Model Validation

For model validation, the experiment reported by Sethuraman et al. [60] was simulated. In Ref.[60], the a-Si thin film of 250 nm thick was cycled galvanostatically at C/4 rate. The available results include the cell voltage and the in-situ biaxial stress variation with SOC for cycles after the first cycle. The biaxial stress was determined through the Stoney equation based on the substrate curvature measurement[176,177].

The FE model for the thin film experiment is shown schematically in Fig. 6.4(a). The dimensions of model is listed in Table 6.5. The simulations were performed with parameter values reported in Table 3.1 and k_0 , α_a and α_c values determined in this work. The predicted cell voltage and biaxial stress are compared with the experimental results in Fig. 6.4(b) and 6.6(c), respectively. As seen, the predicted stress variation with SOC was in good agreement with the experiment. The cell voltage prediction, although less accurate, agrees with the experimental trend. The simulation was also performed with $\alpha_a = \alpha_c = 0.5$ and $k_0 = 8 \times 10^{-15}$, and the results are plotted in Fig. 6.4(b). As shown, the predicted cell voltage locus during delithiation deviated further from the experimental curve with $\alpha_a = \alpha_c = 0.5$.

Table 6.5 Model dimensions used in the Si thin film model

Quantity	Si Nanowire	Current Collector	Li Electrode	Electrolyte
Height (nm)	250	200	100	250
Width (μm)	1	1	1	1

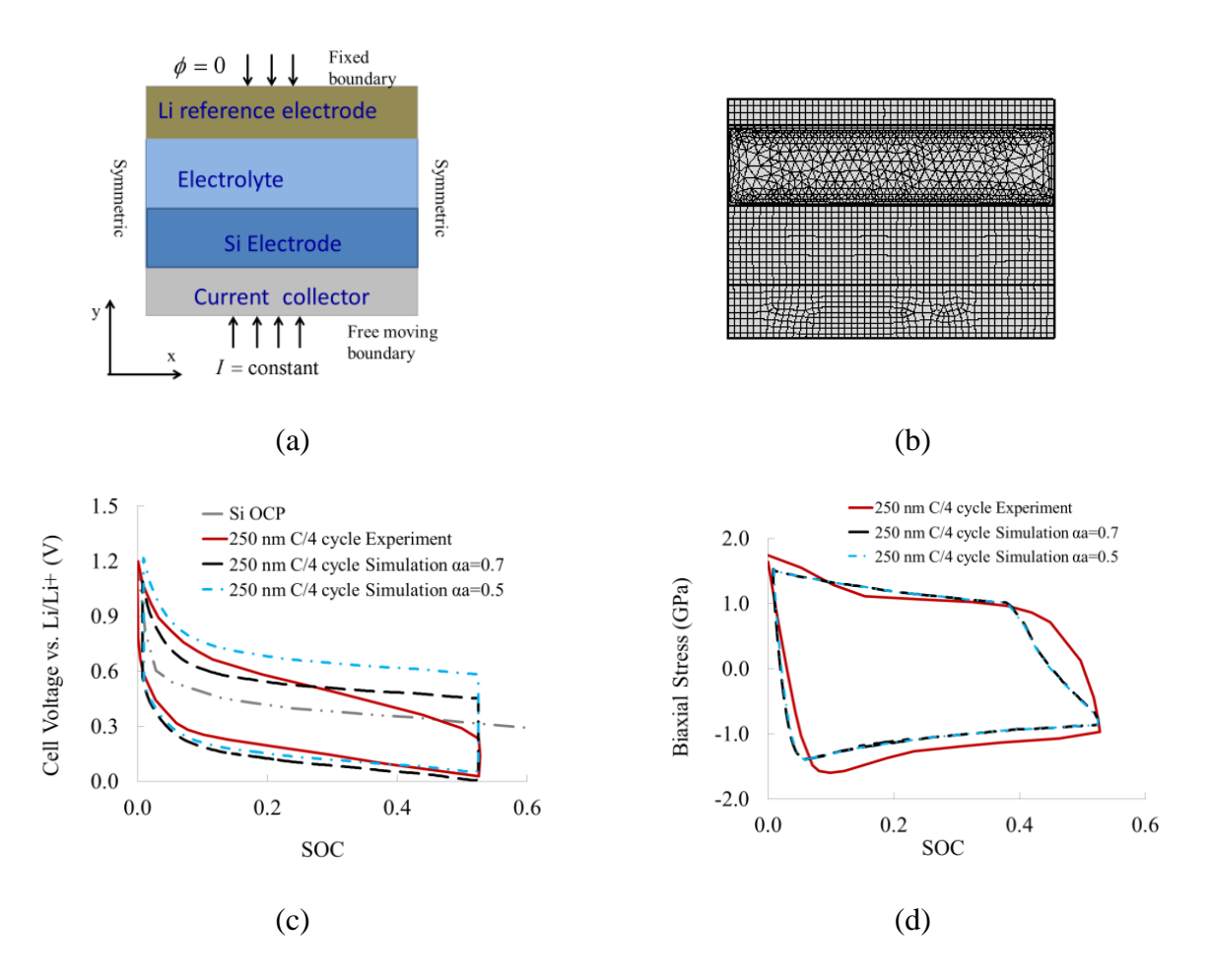


Figure 6.4 Simulation of the experiment of the thin film a-Si electrode by Sethuraman et al. [60]. The FE model used was depicted in (a) and the mesh used in (b). The comparison between simulations and experiments were given for both (c) cell voltage and (d) biaxial stress vs. SOC during cycling at C/4 rate.

6.5 Cell Design with Si Nanowalls

In order to achieve a high volumetric/specific cell capacity, the Si should be packed as densely as possible in the electrode. On the other hand, the electrode should have sufficient Li supply within the designed charging range. The overall efficiency of the cell depends on a number of design parameters such as the shape and the size of Si nanostructures, the packing density, and the Li⁺ salt concentration in the electrolyte. The MRM model is a useful tool in the

investigation of design options and in design optimization. The use of MRM model is demonstrated by a parameter study for a half cell with Si nanowalls (SiNWs) anode.

6.5.1 Design Parameter Study

Fig. 6.5 shows the FE model for this investigation. Considering the symmetry, the model is simplified by including two half SiNWs with fluid electrolyte filling the space between them. The model also contains a current collector at the Si side and a Li counter electrode.

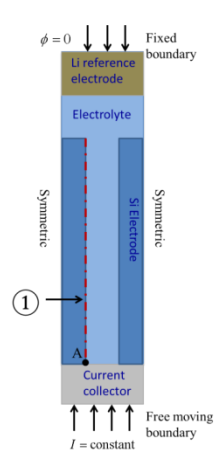


Figure 6.5 Schematic of the model used for the parameter study for Si half cell. Line ① and Point A are for the data analysis in later discussion.

The parameters studied include the wall thickness; the aspect ratio (AR) - the ratio of the length to thickness of the wall; the spacing ratio (SR) - the ratio of the space between the wall to the wall thickness; and the initial Li⁺ concentration in the electrolyte. The baseline was for 200 nm SiNWs, with AR=45, SR=1, and in 1M LiPF₆ in EC/DMC. The dimensions used for baseline test was listed in Table 6.6. The design parameter was changed one at a time in respect to the baseline. Table 6.7 provides a summary of the cases studied and the maximum SOC achieved under 1C charging rate. Since the amount of Si varies in cells of different designs, to keep the

same rate, the applied current has to vary accordingly. As a result, the current density at the Sielectrolyte interface remained the same for the cases with 200 nm SiNWs but almost doubled for 400 nm SiNWs.

Table 6.6 Model dimensions used in the baseline model

Quantity	Si Nanowire	Current Collector	Li Electrode	Electrolyte
Height (µm)	9	1	1	2
Width (nm)	200	400	400	400
Initial concentration (mol m ⁻³)	0	/	/	1000
Maximum concentration (mol m ⁻³) 311307.4/V		/	/	/

Table 6.7 Half cells with SiNWs of different design parameters and the maximum SOC at 1C

	Aspect Ratio	Spacing Ratio	LiPF ₆ in electrolyte (Mole)	Nanowall thickness (nm)	Maximum SOC
	Katio	Katio	electrolyte (Mole)	unckness (IIII)	
Baseline Test	45	1	1	200	0.17
AR=15	15	-	-	-	0.42
AR=90	90	-	-	-	0.050
SR=0.5	-	0.5	-	-	0.089
SR=2	ı	2	-	-	0.31
2M LiPF ₆	-	-	2	-	0.34
3M LiPF ₆	-	-	3	-	0.43
Thickness=400 nm	-	-	-	400	0.032

[&]quot;-" = the same as the baseline

Fig. 6.6 examines the effect of electrode design parameters. Fig. 6.6(a) plots the cell voltage vs. SOC. In simulations, the cell voltage was measured at the bottom of the current collector with respect to the Li electrode. The lithiation terminates when the cell voltage reaches 0V and hence the SOC at 0V represents the maximum SOC for the cell. These values are also listed in Table 6.7. As shown, the maximum SOC increases with increasing the SR and Li⁺ concentration in the electrolyte, and decreases with increasing the AR and nanowall thickness.

6.5.2 Concentration Polarization

The maximum SOC that a cell can achieve appears to relate to the level of Li⁺ and the concentration polarization in the cell. Fig. 6.6(b) examines the Li⁺ concentration in the electrolyte along the Si-electrolyte interface (line ① in Fig. 6.5) at the end of lithiation. As shown, the cell with a lower Li⁺ and a steeper Li⁺ profile corresponds to a lower maximum SOC. For the cases of AR=90 and Thickness=400 nm, the concentration polarization has led to Li⁺ depletion near the current collector, and the lowest SOC. For all other cases, ample supply of Li⁺ was still available at the Si-electrolyte interface when the lithiation stopped.

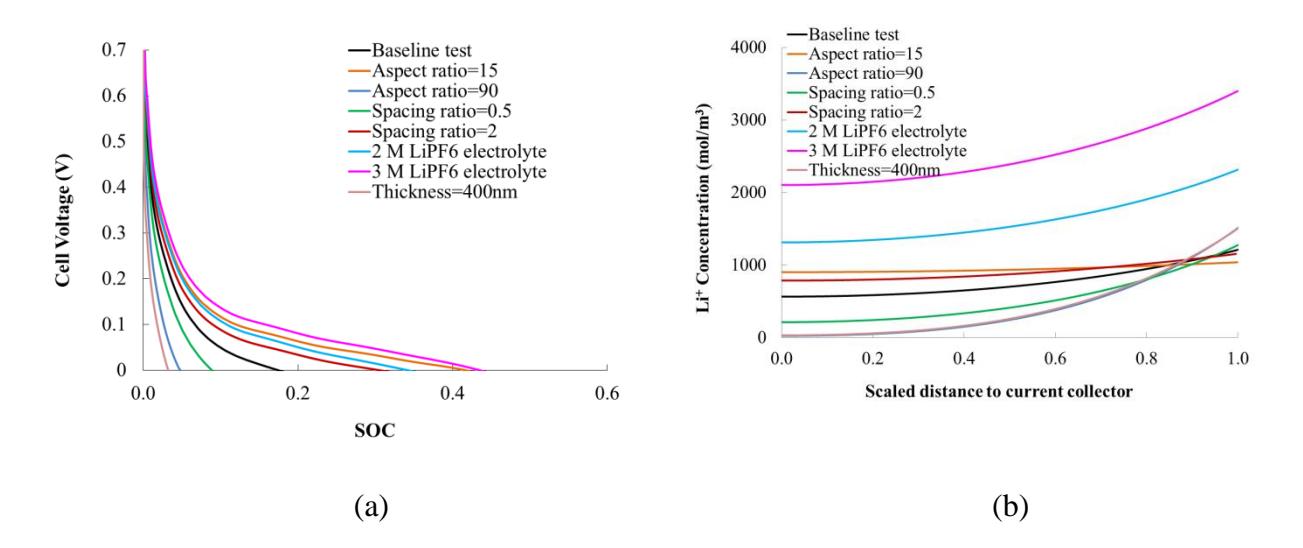


Figure 6.6 (a) The cell voltage changes with SOC at various test cases, and (b) the Li⁺ concentration along the Si-electrolyte interface (line 1) in Fig. 6.5) at the end of lithiation in each test case.

6.5.3 Potential Evolution

Since the lithiation process is driven by the potential difference between the two electrodes, the evolution of the potentials was examined. Four potentials are involved in this process: the Si

potential ϕ_1 , OCP U, electrolyte potential ϕ_2 , and overpotential η . These potentials are related by Eq. 3.18 as $\phi_1 = \eta + \phi_2 + U$. While U is determined by the local SOC as shown in Fig. 6.2(a), ϕ_1 , ϕ_2 and η are governed by the local currents.

Fig. 6.7 examines the evolution of four potentials for the baseline case at point A (in Fig. 6.5), which is on the Si-electrolyte interface and at the base of NW. As the voltage drop in the current collector is negligible, ϕ_1 at Point A approximately equals to the cell voltage. Fig. 6.7 shows that η and ϕ_2 display a sudden change at the beginning of the lithiation process and then become relatively stable whereas U reduces steadily with the local SOC over time. After the initial stage, ϕ_1 reduces at a similar rate as U. The stabilized η and ϕ_2 values determine the range of ϕ_1 . Further away from zero are these potentials, smaller is the range of ϕ_1 , which in turns leads to a lower maximum SOC.

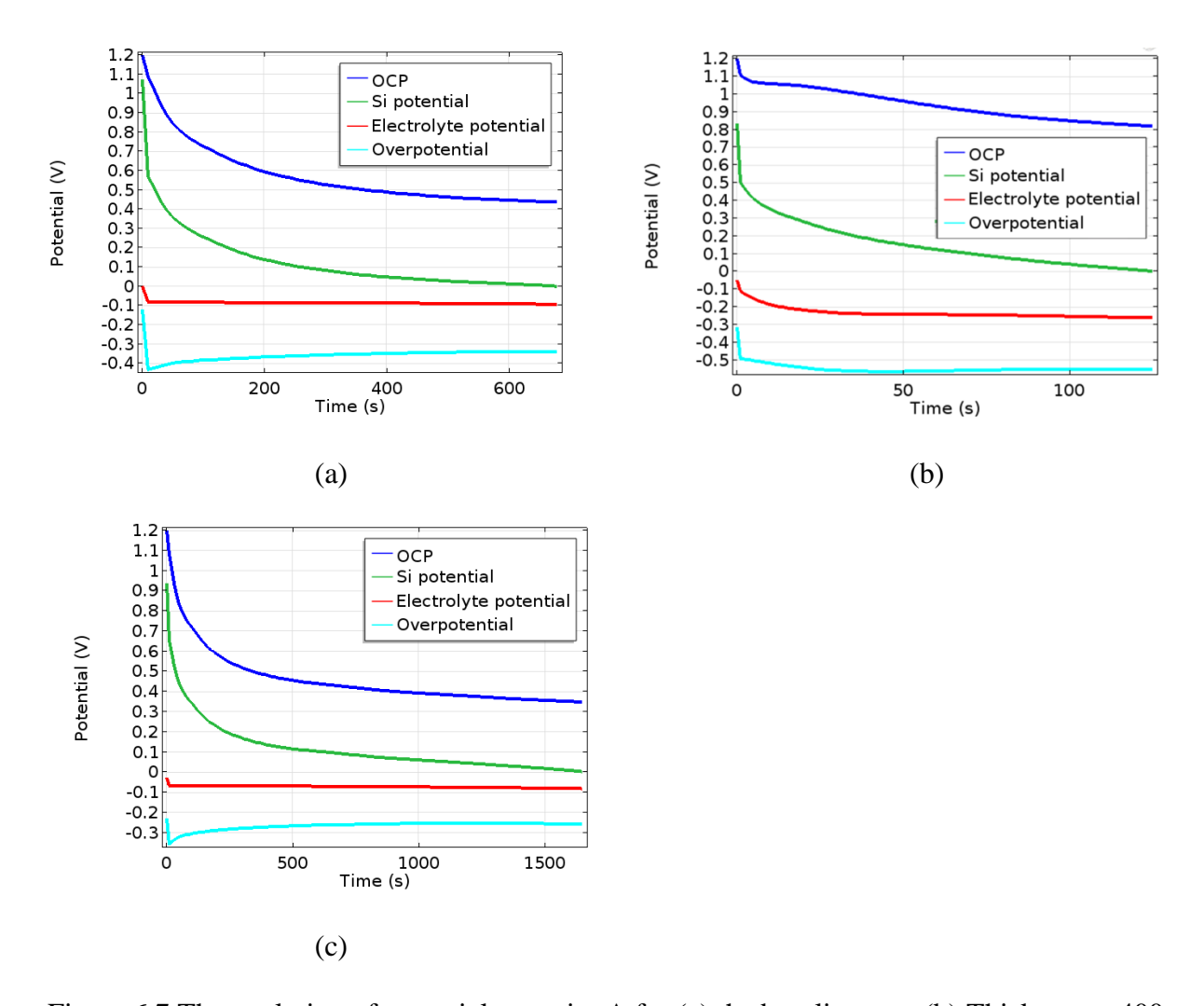


Figure 6.7 The evolution of potentials at point A for (a) the baseline test; (b) Thickness = 400 nm, and (c) $3M \text{ LiPF}_6$ electrolyte.

As shown by Eq. 3.18, ϕ_2 is influenced by c_2 , the Li⁺ concentration in the electrolyte, and k_2 , the ionic conductivity, and the latter is also a function of c_2 . The local ϕ_2 , therefore, is influenced by the concentration polarization. The factor enhancing the concentration polarization would lead to a lower stabilized ϕ_2 value. The stabilized η value follows the same trend. Table 6.8 summarizes the trends how various design parameters influence these potentials. Fig. 6.8 compares the profiles of ϕ_2 and η at the Si-electrolyte interface at SOC=0.03 for different cases.

Increasing the SR and electrolyte concentration, and reducing the AR and nanowall thickness lead to reduced concentration polarization, a lower magnitude of ϕ_2 and η , and higher SOC.

Table 6.8 The influences of design parameters on $\,c_2\,$ polarization, $\,\phi_2\,$, $\,\eta\,$, $\,\phi_1\,$ and SOC

Test Conditions	Concentration polarization	Electrolyte potential (ϕ_2)	Overpotential (η)	Overall Si potential (ϕ_1)	Final SOC
$_{\mathrm{AR}}$ \uparrow	↑	\downarrow	\downarrow	\downarrow	\rightarrow
$_{ m SR} \uparrow$	\	↑	↑	↑	↑
Li ⁺ c ₂ ↑	~	↑	↑		↑
Wall thickness	↑	\downarrow	\downarrow	\downarrow	\

 $[\]uparrow$ =increases, \downarrow =decrease, \cong = same level

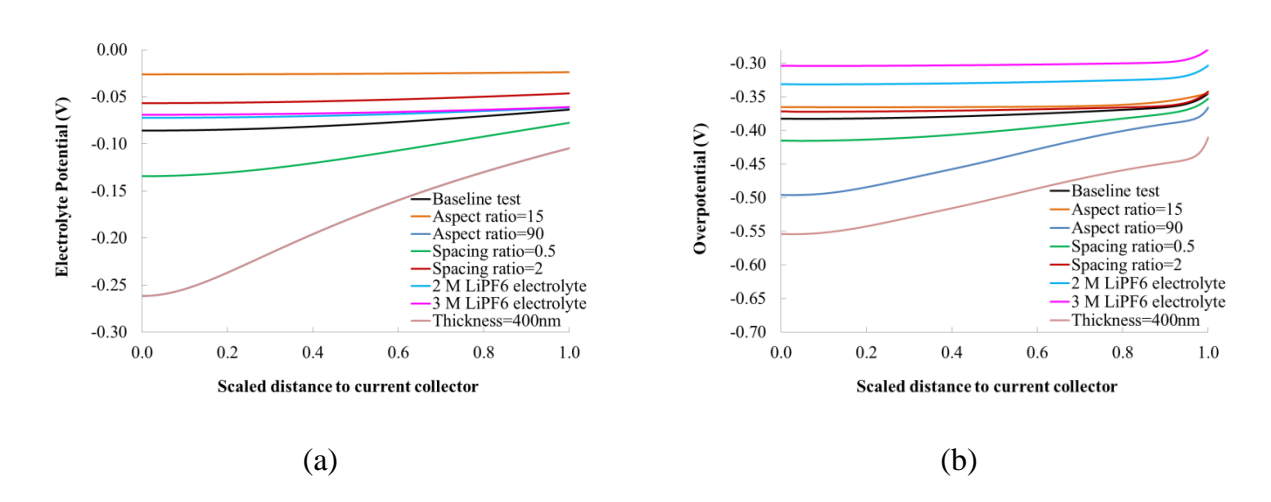


Figure 6.8 The profiles of (a) electrolyte potential and (b) overpotential along line ① in Fig. 6.5 at SOC=0.03 for various test cases.

6.5.4 Cell Capacity

The capacity of a cell is compared by the specific capacity (mAh/g) and the volumetric capacity (mAh/cm³). Table 6.9 presents a comparison of the cell capacity for SiNWs half cells with different AR and SR values under 0.25C, 1C and 4C charging rates. The capacity was calculated based on the total weight or volume of Si, 10 µm thick Cu current collector[114], and the fluid electrolyte contained inside the cell. The capacities as a function of AR and SR are also shown in Fig. 6.9. Table 6.10 presents the cell capacity retention in reference to 0.25C.

The results show that the cell with the highest SOC is not necessarily the one with the highest capacity, such as the case of AR=15 and SR=2. Furthermore, the capacity is not a linear function of AR and SR. A high level of specific capacity is found in cells with AR=90 and SR=2 at low C rate (0.25C), and with AR=45 and SR=2 at higher C rates (1C-4C). On the other hand, the volumetric capacity is relatively high when SR in the range of 1-2, AR is in range of 45-90 at low C rate (0.25C-1C) and is in the range of 15-45 at high C rate (1C-4C). The capacity retention is judged by the SOC ratio with reference of 0.25C. As shown, the AR increases resulted in decrease in capacity retention.

Table 6.9 Comparison of the specific and volumetric capacity of half cell with SiNWs under 0.25C, 1C and 4C $\,$

AR	SR	Specific capacity (mAh/g)			Volumetric capacity (mAh/cm ³)		
		0.25C	1C	4C	0.25C	1C	4C
15	0.5	78.27	54.16	8.54	566.05	391.68	61.78
15	1	96.59	55.42	7.92	693.66	398.00	56.86
15	2	67.59	40.75	6.35	482.02	290.60	45.26
45	0.5	148.82	42.25	2.14	834.78	237.01	12.01
45	1	216.66	60.88	6.66	1182.45	332.26	36.35
45	2	178.64	75.45	8.76	956.39	403.92	46.91
90	0.5	131.80	10.51	0.81	578.41	46.13	3.55
90	1	262.56	31.33	1.57	1115.13	133.07	6.65
90	2	280.90	51.86	3.43	1153.28	212.91	14.09

Table 6.10 Comparison of the SOC and the capacity retention of half cell with SiNWs under 0.25C, 1C and 4C $\,$

AR	SR	SOC			Capacity Retention	
		0.25C	1C	4C	1C/0.25C	4C/0.25C
15	0.5	0.45	0.31	0.049	0.69	0.11
15	1	0.73	0.42	0.060	0.58	0.082
15	2	0.76	0.46	0.072	0.61	0.095
45	0.5	0.32	0.09	0.0046	0.28	0.014
45	1	0.61	0.17	0.019	0.28	0.031
45	2	0.73	0.31	0.036	0.42	0.049
90	0.5	0.16	0.013	0.0010	0.081	0.006
90	1	0.42	0.050	0.0025	0.12	0.006
90	2	0.65	0.12	0.0079	0.18	0.012

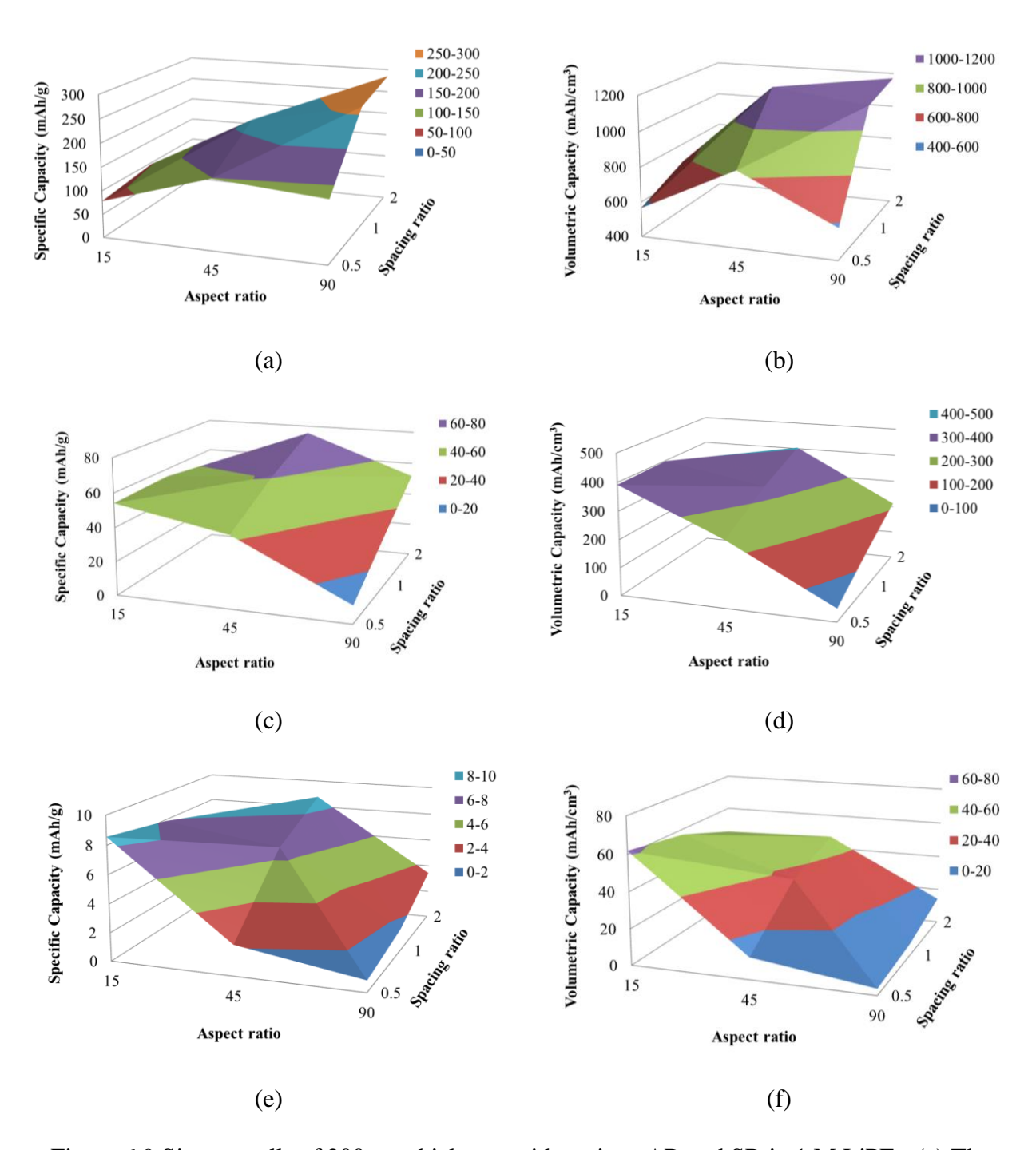


Figure 6.9 Si nanowalls of 200 nm thickness with various AR and SR in 1 M LiPF₆. (a) The specific capacity and (b) the volumetric capacity at 0.25C rate, (c)(d) at 1C, and (e)(f) at 4C.

6.6 Conclusion

A multiphysics microstructure-resolved model (MRM) has been developed for Li-ion battery (LIB) cell with a-Si anode. The model couples the electrochemical kinetics, species transport, and the structural/stress evolutions. The coupled diffusion and deformation problem was solved in COMSOL Multiphysics®. Besides the parameters determined in our previous studies, the reaction rate constant ($k_0 = 8 \times 10^{-15}$ (m/s) (mol/m³)^{-0.7}) and apparent transfer coefficient ($\alpha_a = 0.7$; $\alpha_c = 0.3$) were determined in this work. The model was validated by simulating a-Si experiments from literature.

The model was used to investigate the parameter design of Si nanowall anodes with a half cell configuration. The results showed that the maximum SOC of a cell can achieve under a given charging rate depends on the electrolyte potential and overpotential. The two potentials in turns depend on concentration polarization. The factors reducing concentration polarization will enhance the maximum achievable SOC of the cell. Such measures include increasing the space ratio and Li⁺ concentration in the electrolyte, and reducing the aspect ratio and nanowall thickness. On the other hand, the cell with the highest SOC does not necessarily lead to the highest capacity. The specific/volumetric capacities display a nonlinear relationship with the aspect ratio and spacing ratio. The MRM model can be used for design optimization.

Chapter 7 Conclusion and Outlook

7.1 Conclusion and Contributions

In this work, an MRM model has been developed for a basic Li-ion battery cell with Si anode in Li-ion. This model couples the electrochemical kinetics, species transport, and the structural/stress evolutions. The model can be used for the design optimization of Si anode and the battery performance of the cell. It can also be used to investigate the stress and deformation in different cell components. The specific contributions are

7.1.1 Identify the Range of Li Diffusion for a-Si Anode

The lack of key material properties for Si/Li_xSi, especially the Li diffusivity in Si, has prevented the efficient use of such numerical tools in the design of lithium-ion batteries with Si anodes. Therefore, parameter investigations were firstly performed using FEA on the single Si particles outside the MRM model. The Li diffusion and volume expansion were coupled and solved in COMSOL Multiphysics[®]. By comparing with the lithiation experimental observations for the a-Si nanospheres, the range of Li diffusivity for a-Si anode was identified. This value is one of the key input parameter for MRM model for Si.

7.1.2 Identify the Chemical-Mechanical Two-Way Coupling Mechanism for Si under Large Deformation Framework

A strong asymmetric rate behavior between lithiation and delithiation has been observed in amorphous Si (a-Si) anode in the form of thin films, but not in other geometries, such as Si nanospheres. The chemo-mechanical coupling of Si under large deformation was investigated by simulating the rate behavior of the two geometries. The results reveal that the rate behavior is affected by the geometry and the constraint of the electrode, the chemo-mechanical coupling, and the prior process. A substrate-constrained film has a relatively low surface/volume ratio and

a constant surface area. Its lithiation has a great tendency to be hindered by surface limitation. The chemo-mechanical coupling also plays an important role. The stress profiles differ in the two geometries but both affect the lithiation process more than the delithiation process. The overall delithiation capacity is affected very little by the chemo-mechanical coupling. In cyclic loading, the delithiation capacity is reduced at the same rate as the lithiation capacity because of the low initial state of charge in the electrode. The asymmetric rate behavior was absent under cyclic loading. On the other hand, a slow charging process resulted in a better retained delithiation capacity and an asymmetric rate behavior at higher rates.

7.1.3 Identify the Range of the Electrochemical Kinetic Parameters

In order to correctly predict the cell performance, the electrochemical reaction of Si in cell under the large deformation framework was studied first. Through correlating the simulation results to the cell cycling experiments, the electrochemical reaction related parameters were characterized, including the reaction rate constant and apparent transfer coefficient. The model was validated with Li-ion cell experimental results in literature, obtained with both Si nanowires and thin films at different cycling rates

7.1.4 A Design Tool for the Optimal Design of Battery Cells with a-Si Anode

The use of MRM model was demonstrated in a parameter study of Si nanowall|Li cells. The specific and volumetric capacities of the cell as a function of the size, length/size ratio, spacing of the nanostructure, and the Li⁺ concentration in the electrolyte were investigated. The results show that the cell with the highest SOC is not necessarily the one with the highest capacity. Furthermore, the capacity is not a linear function of design parameters, such as aspect ratio or spacing ratio. For example, a larger aspect ratio of Si nanowall is beneficial to specific and

volumetric capacities at low cycling rates, and vice versa. Study also showed that the spacing ratio between Si nanowall is best for volumetric capacity when ranges from 1-2.

7.2 Outlook of Future Work

The study of high capacity Li-ion battery is a field full of opportunities. The MRM model developed in this work can be used not only in improving battery design but also in advancing our understanding of the coupled electrochemical and mechanical processes.

7.2.1 Interfacial Interplay between Si and Other Components

Interfacial problems are present from a number of places in Li-ion battery, including

- 1) When Si is surrounded by electrolyte, the solid electrolyte interface (SEI) layer is generated at the Si surface during cell cycling. Interface evolves between Si and SEI.
- 2) To prevent SEI, coatings were deposit on Si surface using material such as Cu and graphite. The interplay between Si and Cu or graphite raises another interaction problem.
- 3) Most electrode matrices consist of not only active Si particles but also binder. The interface between Si and binder present an interfacial problem.
- 4) When Si is deposited directly onto the current collector, there is an interface between Si and current collector. A preliminary study on this problem is showed in Appendix D.

By adjusting the MRM model with the inclusion of interface and the possibility of interfacial delamination, the unidentified interaction mechanisms may be revealed.

7.2.2 Thermal Management of Li-Ion Cell

The thermal management of commercialized Li-ion cell has been one of the design criteria in industries such as small electronics and automobile. With a new type of electrode material (Si), the heat generated during battery cycling may be greatly altered. So the design of the thermal management system strongly relies on the prediction of heat generation and temperature variance.

The MRM model can be further developed to consider the temperature influence on the electrochemical reactions, mass transport and structural and stress evolutions under various cycling conditions.

7.2.3 Extension of Model to Other High Energy Density Electrode Material Li-Ion Cell

Besides Si, other high capacity electrode materials such as Sn, Ge and Al, etc., also exhibit large volume change with lithiation/delithiation. The current model can be adopted to investigate these electrode materials as well.

The model can also be used in a multi-scale framework, or in conjunction with other software, to investigate the performance of battery packs.

APPENDICES

Appendix A Effect of Li Transport Distance Change and Geometrical Constraint on Different

Si Geometries

Under galvanostatic cycling, a constant Li flux N is maintained at the Si electrode surface. The Fick's first law corresponding to this boundary condition is

$$-\frac{D_1}{RT}c_1\nabla\mu_{Li}=N$$
 Eq. A1

The differences between Si thin film and sphere geometries under the influence of volume expansion and geometrical constraint will be discussed in A.1 and A.2.

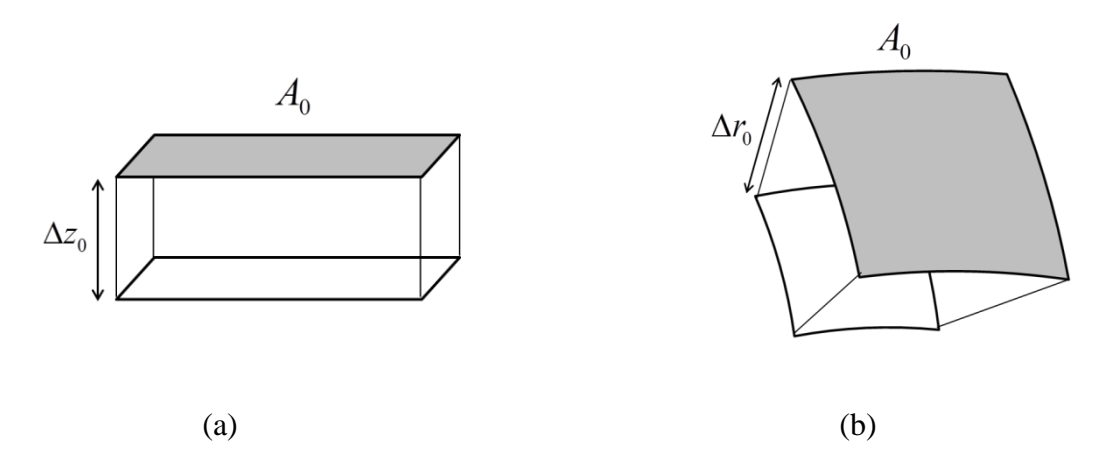


Figure A.1 Control elements at electrode surface in Si geometry (a) thin film and (b) sphere

A.1Si Thin Film

For a substrate-constrained Si thin film, as it is confined to expand only along the z direction, the $\nabla \mu_{Li}$ in Eq. A1 is reduced to 1D with $\partial \mu_{Li}/\partial z$. Fig. A.1(a) shows a rectangular control element at the surface. It has a surface area of A_0 and an initial thickness of Δz_0 . The Li flux applied at A_0 is N_0 , Eq. A1 becomes

$$-\frac{D_1}{RT}c_1\frac{\partial \mu_{Li}}{\partial z_0} = \mathbf{N_0}$$
 Eq. A2

The control volume thickness changes to Δz during lithiation and the surface area remains as A_0 . Eq. A2 becomes

$$-\frac{D_1}{RT}c_1\frac{\partial \mu_{Li}}{\partial z} = \mathbf{N_0}$$
 Eq. A3

The relationship between Δz and Δz_0 is

$$\Delta z = \det(\mathbf{F})\Delta z_0 = J\Delta z_0$$
 Eq. A4

where **F** is the deformation gradient. J is the determinant of **F**, which reveals the volume change of the element, i.e., $J = V/V_0$ [195]. Therefore

$$\frac{\partial \mathbf{z}}{\partial \mathbf{z}_0} = \mathbf{J}$$
 Eq. A5

Apply the chain rule to Eq. A3 and substitute Eq. A5 in, we have

$$-\frac{D_1}{RT}c_1\frac{\partial \mu_{Li}}{\partial z_0}\frac{\partial z_0}{\partial z} = J^{-1}\left(-\frac{D_1}{RT}c_1\frac{\partial \mu_{Li}}{\partial z_0}\right) = \mathbf{N_0}$$
 Eq. A6

The lithium induced volume expansion increases the Li transport distance and results in a *J* times slower diffusion. Therefore, lithiation stopped at lower capacity when maximum concentration reached at the thin film surface. Vice versa, during delithiation, the delithiation accompanied volume shrinking decreases the Li transport distance, and resulted in a *J* times faster delithiation. Thus, the end-state of delithiation was close to full discharge. Thus, the asymmetric rate behavior would be observed even without considering the stress effect on Li diffusion in thin film.

A.2 Si Nanosphere

In contrary to thin film geometry, Si nanosphere is considered to expand freely without constraint, as explained in the main text. According to the spherical symmetry, the $\nabla \mu_{Li}$ in Eq. A1 can be reduced to 1D with $\partial \mu_{Li}/\partial r$. Fig. A.1(b) shows the control element at the particle

surface with an initial thickness of Δr_0 and initial surface area A_0 . Li flux applied at A_0 is N_0 . Eq. A1 becomes

$$-\frac{D_1}{RT}c_1\frac{\partial \mu_{Li}}{\partial r_0} = N_0$$
 Eq. A7

As lithiation proceeds, the radius of the sphere increased from r_0 to r and the surface area increased to $A = A_0 r^2 / r_0^2$. Therefore, the surface Li flux decreases from N_0 to N

$$N = N_0 \frac{r_0^2}{r^2}$$
 Eq. A8

Substitute Eq. A8 to Eq. A7, then

$$-\frac{D_1}{RT}c_1\frac{\partial \mu_{Li}}{\partial r} = N_0\frac{r_0^2}{r^2}$$
 Eq. A9

Apply chain rule to Eq. A9

$$-\frac{D_1}{RT}c_1\frac{\partial \mu_{Li}}{\partial r_0}\frac{\partial r_0}{\partial r} = N_0\frac{r_0^2}{r^2}$$
 Eq. A10

The relationship between Δr and Δr_0 is

Eq.
$$\Delta r = det(F) \Delta r_0 = J^{1/3} \Delta r_0 \label{eq:det_fit}$$
 All

where F and J share the same definiations as in Eq. A4.

The relationship between r and r_0 is

$$r = r_0 \left(\frac{V}{V_0}\right)_{\text{sphere}}^{1/3}$$
 Eq. A12

where $(V/V_0)_{sphere}$ is the volume ratio (current volume/initial volume) of the sphere.

Substitute Eq. A11 and 12 to Eq. A10, we have

$$J^{-1/3} \left(\frac{V}{V_0}\right)_{\text{sphere}}^{2/3} \left(-\frac{D_1}{RT} c_1 \frac{\partial \mu_{Li}}{\partial r_0}\right) = N_0$$
 Eq.

In spherical geometry, although the lithium induced volume expansion increases the Li transport distance to $J^{-1/3}$ times, the surface area also increases along with the expansion to $(V/V_0)_{\rm sphere}^{2/3}$ times. If the Li concentration is uniform inside the Si sphere when lithiating at low C rate, then $J = (V/V_0)_{\rm sphere}$. Eq. A13 reduces to

$$J^{1/3}\left(-\frac{D_1}{RT}c_1\frac{\partial\mu_{Li}}{\partial r_0}\right) = N_0$$
 Eq. A14

Overall, the Li diffusion became $J^{1/3}$ times faster. Therefore, the asymmetric rate behavior was not seen in Si nanosphere with α =0. At high C rate, the $J > (V/V_0)_{sphere}$ due to the higher Li concentration at the particle surface. Yet, $J^{-1/3}(V/V_0)_{sphere}^{2/3}$ may still be larger than one unless cycling rate is ultrahigh. As a result, no asymmetric rate behavior was observed for Si nanosphere even at 100C.

Appendix B Transport Phenomena in Si-Li Cells

The use of MRM model is demonstrated by a parameter study for a half cell with Si nanowalls (SiNWs) anode. Fig. B.1 shows the FE model for this investigation. It includes two half SiNWs with fluid electrolyte filling the space between them, a current collector at the anode side and a Li counter electrode Fig. B.1(b)-(e) present selected results at the end of lithiation for the case of 200nm SiNWs with SR=1, AR=15, and in 1M LiPF₆ in EC/DMC. The MRM model can provide not only the overall cell information, like the cell voltage, but also details inside the cell, such as the Li concertation in Si (Fig. B.1(b)) and in the electrolyte (Fig. B.1(c)), individual stress component in solid components (Fig. B.1(d)) and the velocity of the electrolyte (Fig. B.1(e)), etc.

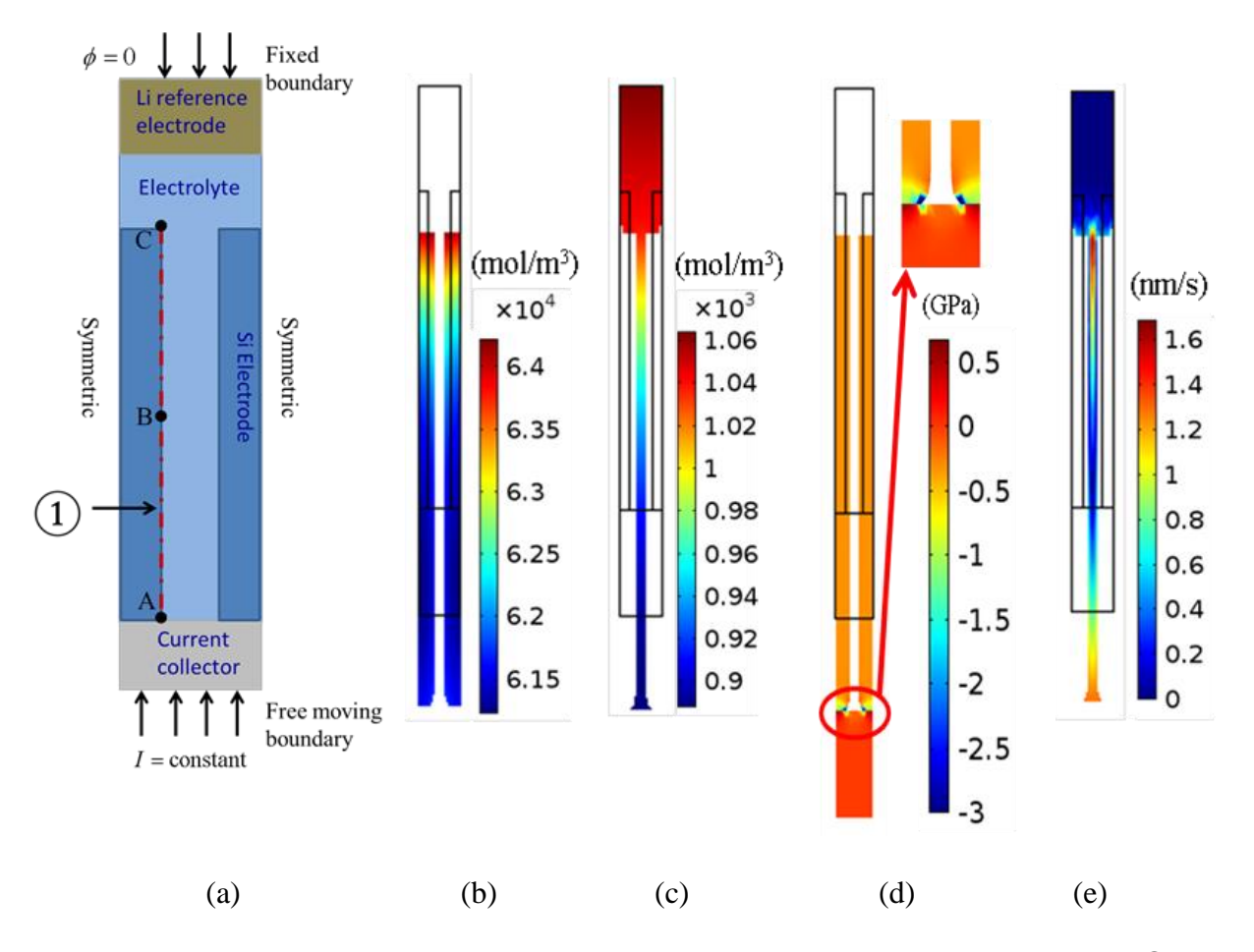


Figure B.1 (a) Schematic of the model used for the parameter study for Si half cell. Line ① and Points A-C are for the data analysis in later discussion; (b)-(f) are profiles at the end of charging at 1C for the case of 200nm SiNWs, with SR=1, AR=15, in 1M LiPF₆ in EC/DMC. The original sizes and shapes are shown in dark lines. (b) Li concentration in Si; (c) Li⁺ in electrolyte; (d) the hydrostatic stress in Si and in current collector; (e) the magnitude of fluid velocity in the electrolyte.

Therefore, by using the MRM model, the cell transport phenomena and other parameters of research interest could be investigated locally. As shown in Table B1, the baseline test in Chapter 6 were plotted along line ①, including the Si potential ϕ_1 , electrolyte potential ϕ_2 , OCP

U, Overpotential at Si surface (bottom to top) η , Li concentration in Si c_1 , Li concentration in electrolyte c_2 , Current at Si surface (bottom to top) $i_{1,2}$, Exchange current density at Si surface (bottom to top) i_{Si} .

Table B.1 Results in baseline test at t=130s (SOC=0.03)

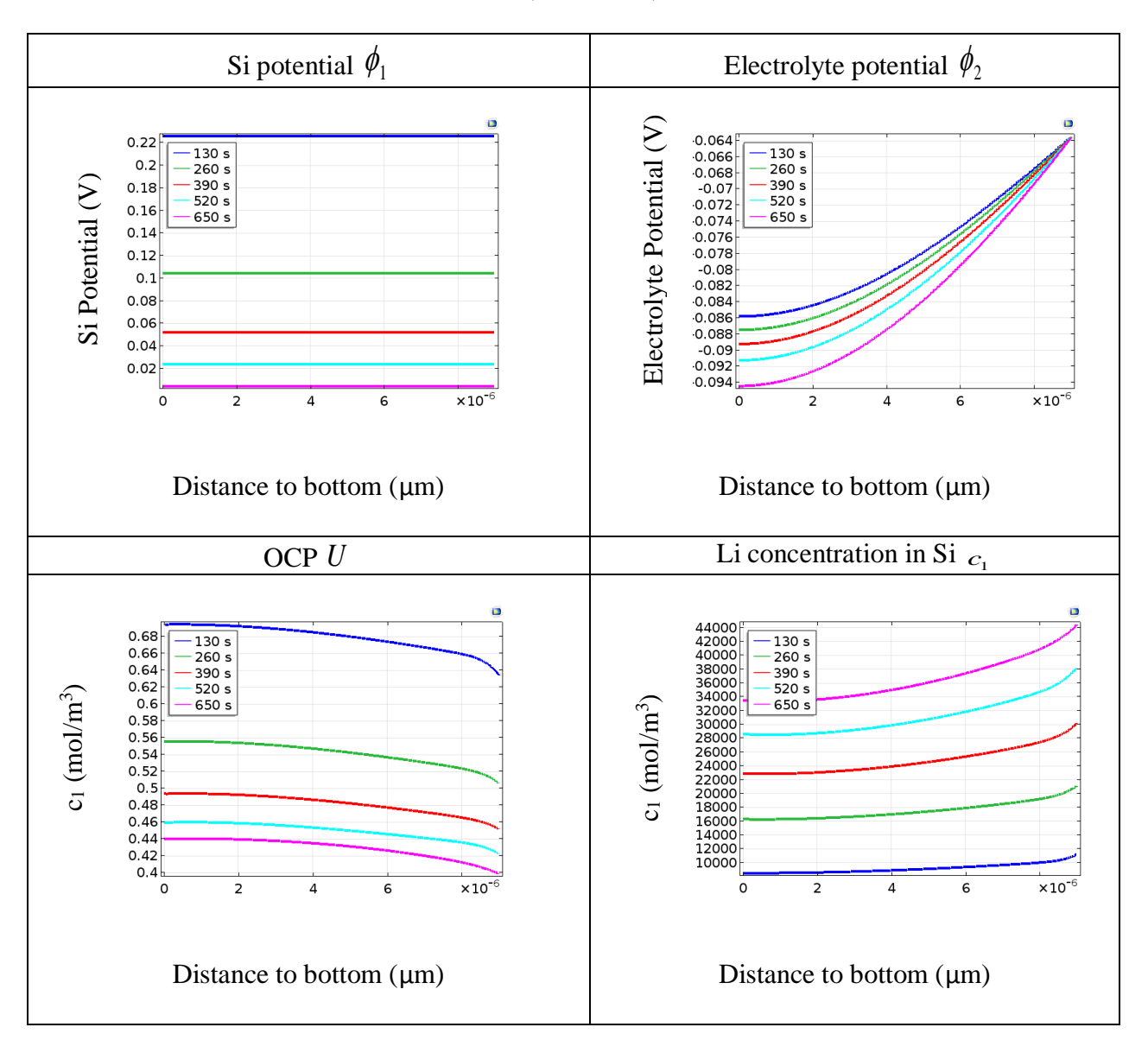
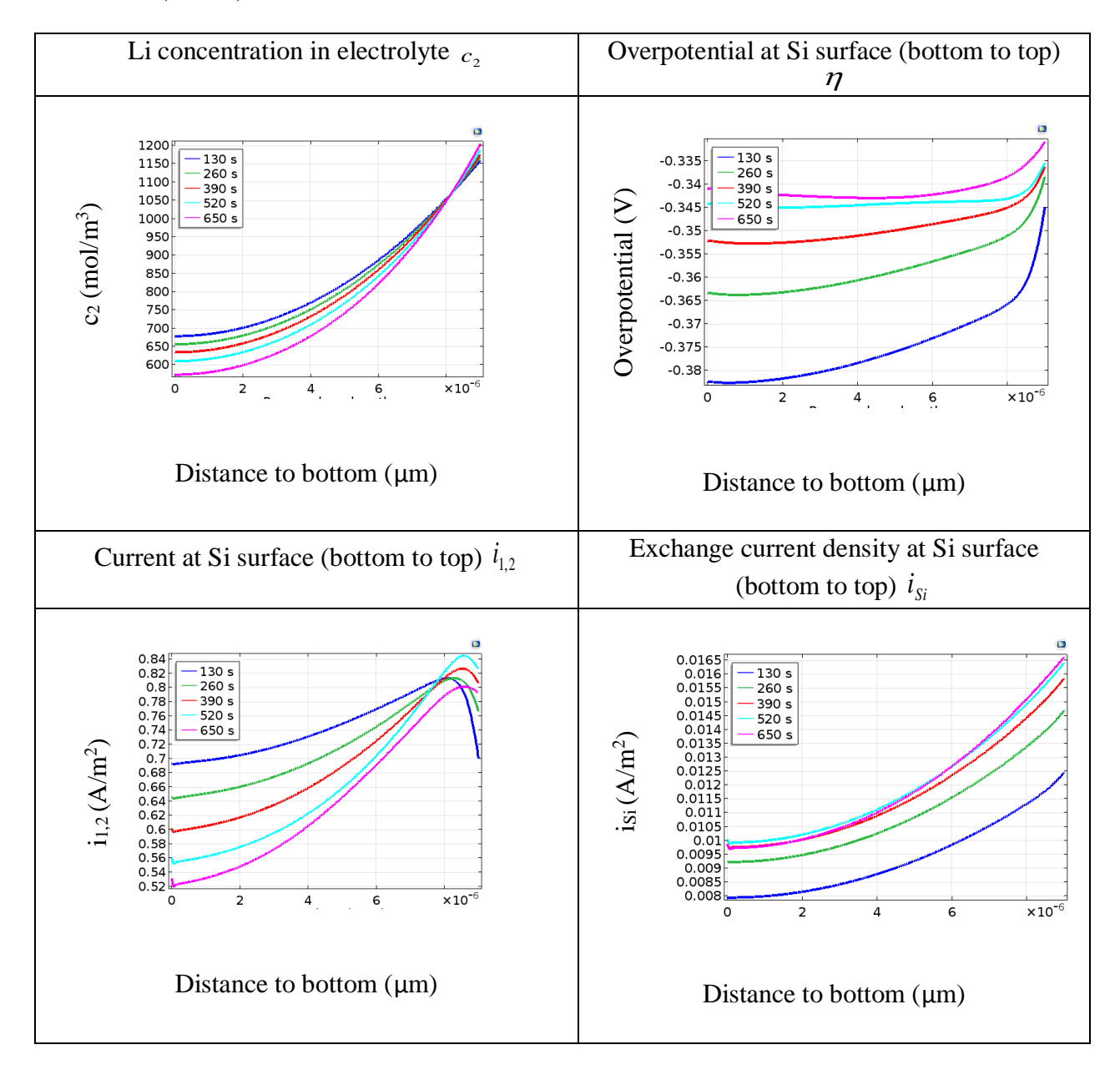


Table B.1 (cont'd)



Appendix C Electrical Conductivity

The order of Si conductivity is selected based on references [107,138]. The reported range varies between 0.1~100 S/m. The conductivity influence on the cell performance is investigated in the model presented in Fig. C.1(a). The tests were conducted for conductivity equals to 33 S/m, 0.33 S/m and 0.033 S/m, respectively. The potential profiles along the Si nanowall were plotted in Fig. C.1(b)-(e). The potential drop across line ① proportionally increases as the conductivity decreases. For example, k_I =33 S/m, the potential drop across line ① is about 10⁻⁵ V/ μ m; k_I =0.033 S/m, the potential drop is about 10⁻² V/ μ m. Overall, the results showed that, even conductivity drops to a very small value, the potential of Si nanowall is still very small and would not present much influence on cell SOC. Therefore, the k_I is kept at 33 S/m in the study in Chapter 6.

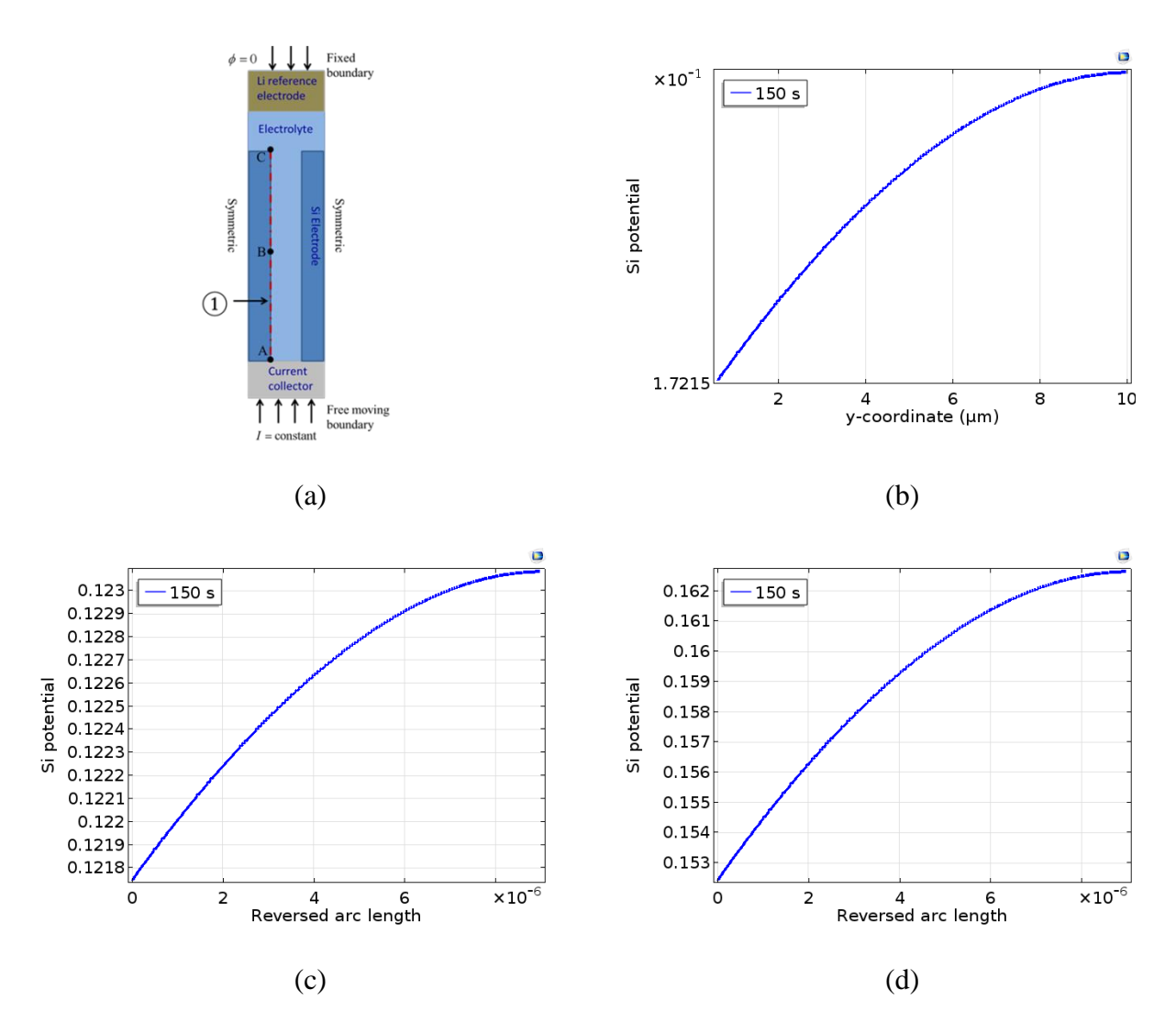


Figure C.1 The investigation of electronic conductivity in Li-Si alloy by plotting the Si potential along ① in (a) at same time (t=150s) when (b) k_I =33 S/m; (c) k_I =0.33 S/m; (d) k_I =0.033 S/m.

Appendix D Si-Current Collector Interaction

The interface in Li-ion battery with Si anode includes the Si/substrate interface, Si/coating interface and Si/binder interface, etc. The interface between different materials often induces complexities such as compound formation and interdiffusion[196]. Furthermore, during battery operation, the movement of Li at this region makes the problem more complex. The interface is extremely important for battery performance prediction in MRM model. Here, we take the Sicurrent collector interface as an example, to show the importance of studying the interface interactions.

Only a few investigations have focused on the interface between Si and current collector. Cu is usually used as current collector for Si. Experimental observations showed that the interface sliding happened during lithiation[50] accompanied by large volume change at Si/Cu interface. A first principle simulation predicted that there was Li segregation at interface, which allowed an almost frictionless interface sliding by changes from Si-Cu to Li-Cu and Li-Si bond, forming interdiffused Li-Si-Cu phase[197,198]. Therefore, the lithiation of interface region and its property evolution may be different from bulk Si and bulk Cu. On the other hand, the adhesion strength at Si/Cu interface is weaker than the bulk materials[199]. The first principle simulation predicted the interface adhesion strength is further reduced by Li segregation[197] that is prone to delamination failure as seen in experiments[199]. Therefore, the material properties at interface are very important input in the modeling Si anode in Li-ion battery. However, quantitative studies for interface properties at Si/Cu or for other kinds, such as Si/Ni, during lithiation are not available in literature. This presents another obstacle in simulating Si anode in Li-ion battery.

The experiment of lithiation of a-Si pillars by Bucci et al.[167] provide a good study case. As shown in Fig. D.1 (a), the a-Si pillar was on a Ni pillar of same diameter formed by deposition and etching process. After lithiation, the a-Si pillar almost doubled its size while the Ni portion showed little deformation. Pillars were sectioned with focused ion beam (FIB) after lithiation or one cycle of lithiation and delithiation. Cracks were observed only in samples after delithiation, as shown in Fig. D.1(b-c). The crack was initiated from the surface of the Si pillar near the interface and propagated into the bulk Si.

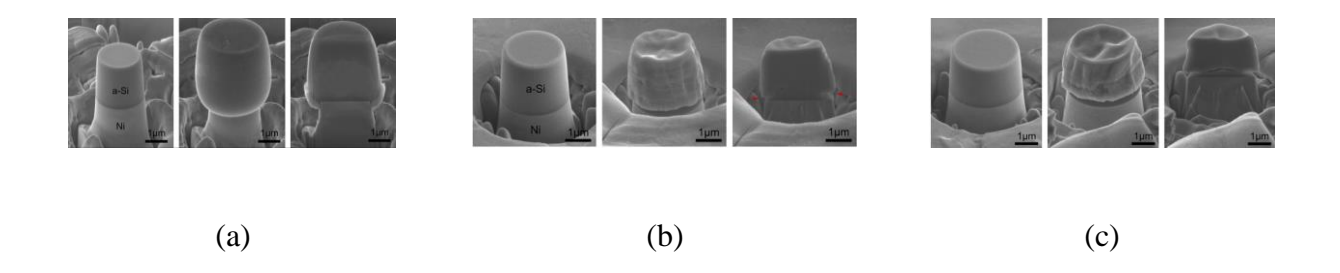


Figure D.1Lithiation and delithiation of a-Si pillars on Ni substrate: (a) lithiation of pillars with diameter of 2100 nm and height of 2300nm; (b) delithiation of pillars with diameter of 2600 nm and height of 2300nm, in which crack is observed at Si surface near Si-Ni interface; (c) delithiation of pillar with diameter of 3150 nm and height of 2100nm, in which the crack propagates toward center of Si pillar[167].

The behavior of a-Si pillar during lithiation/delithiation has been investigated without the consideration of chemical-mechanical coupling and using the Li diffusivity reported in Bucci et al.[167]. The results are showed in Table D.1. For comparison, the FEA results for this

experiment by Bucci et al.[167] were also presented as Simulation I for comparison, where the Ni pillar was treated as rigid material and Si-Ni was treated as perfect bonding. Apparently, this treatment produced better results in Si. However, the change in Ni substrate was not considered.

Bucci et al. did not show the interaction between Si and Ni substrate. Therefore, two more studies conducted in this work are presented in Table D.1. In Simulation II, the a-Si and Ni pillar were modeled as continuous solid with different properties. Ni was modeled with an elastic-plastic material. As shown, the Ni pillar deformed with Si pillar and a high stress was generated in Ni close to the interface. This deformation mode was different from the experimental observation. In Simulation III, a soft interface with properties as shown in Fig. D.2 was introduced between Si and Ni. This resulted in a large deformation in the interface layer while the Ni pillar remained almost undeformed. The shape changes of the Si and Ni pillars after lithiation and delithiation closely agreed with the experimental observation.

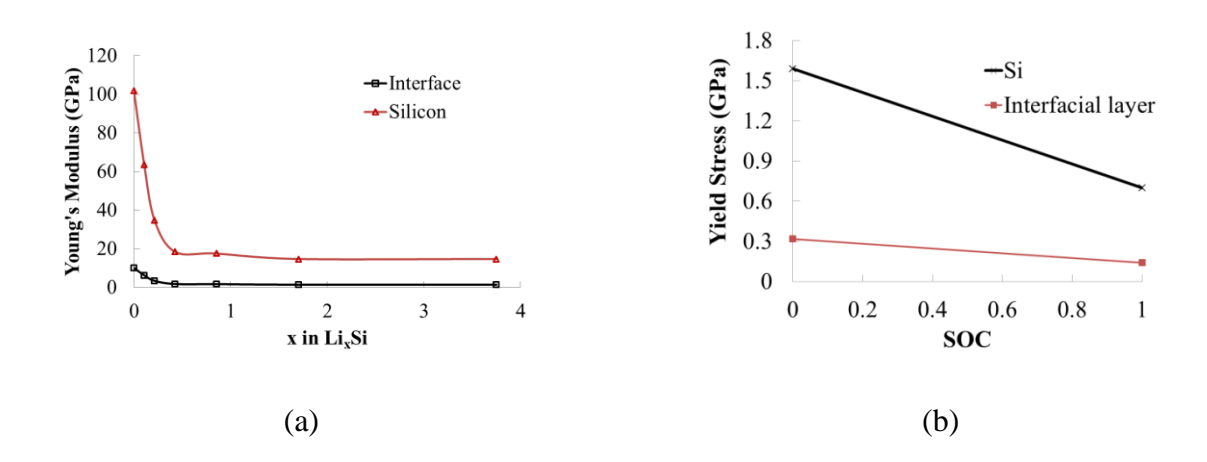


Figure D.2Mechanical properties for the bulk Si and the interface region are modeled separately.

(a) Young's Modulus as a function of concentration; (b) yield stress as a function of concentration.

Table D.1 Preliminary study on Si-Ni interface

Process	Substrate and interface properties	Lithiation	Delithiation
Experiment [167]	-	tun tun	1µm
Simulation I [167]	Ni substrate as rigid substrate Perfect bonding between Si and Ni	σ _{ZZ} [MPa] 1500 1000 1000 200 200 200 200 2100 21	σ _{II} [MPa] 129 129 129 129 129 129 129 129 129 12
Simulation II	Ni substrate with realistic mechanical property Perfect bonding between Si and Ni		-
Simulation III	Ni substrate with realistic mechanical property Thin film region for Li segregated interface		Start of delithiation End of delithiation

This preliminary FEA tests in Table D.1 showed that the interface between Si and current collector may influence the prediction of both shape change and the stress state in Si electrode and substrate. Given Si interface with different current collector/binder/coating materials, this kind of study should be conducted to correctly predict the mechanical response of them and their influence to cell performance.

Appendix E Stress State in Si Nanosphere

E.1 Si Nanosphere with Two Phase Lithiation

The mean stress evolution along particle radius in test 6 in Chapter 4 is shown in Fig. E.1(a). The two-phase lithiation presents a huge effect on stress generated at reaction front because of the high concentration gradient. Homogeneous mean stress in Li-poor core and inhomogeneous in Li-rich shell are accumulated along with lithiation. A stress jump is seen at the reaction front over a small shell thickness, showing the newly lithiated element is further compressed. The similar analytical prediction has seen in literature [64]. Effect of the reaction front extends further into the bulk phases. The Li-poor phase experiences tensile stress at first and gradually reduces to compressive stress as more Si got lithiated. In the meantime, the lithiated silicon located just outside reaction front suffers an elastic reloading due to the push from newly lithiated silicon. As the lithiation is a dynamic process, reaction front effect is repeated and added on to lithiated silicon. A stress fluctuation is seen in Li-rich phase. Overtime, stress becomes smooth in early lithiated silicon. Eventually the stress contour in Fig. E.1(a) is seen along particle radius as the particle got lithiated. The highest compressive stress stays at particle center after two-phase lithiation finishes. Under the high compressive stress along the particle lithiation, the particle tends not to fracture during the first lithiation.

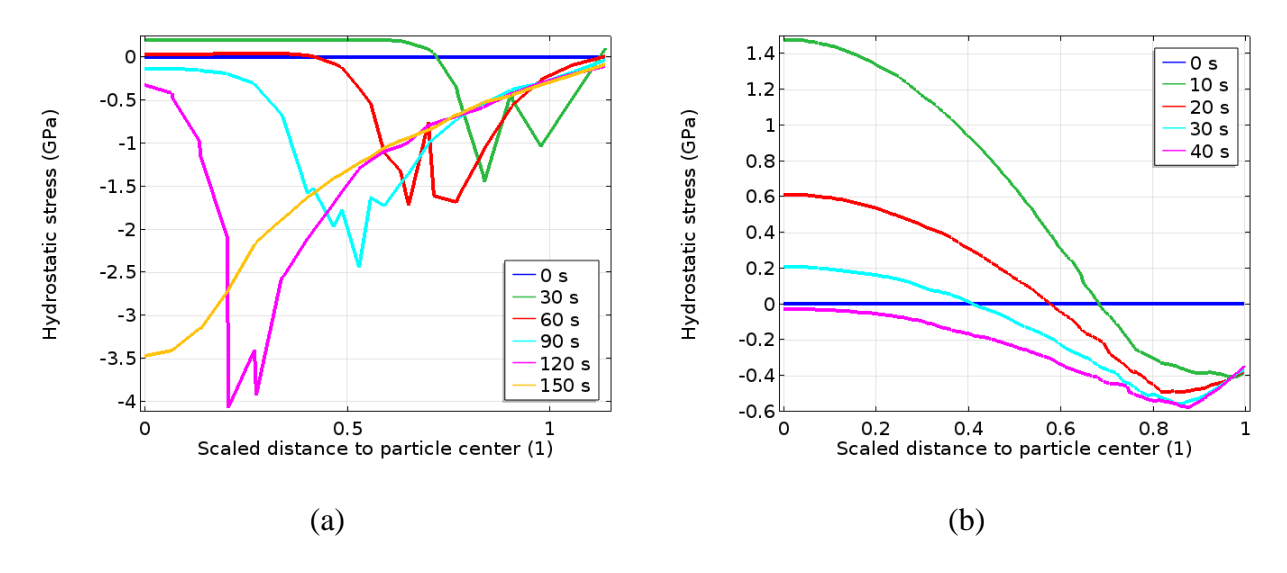


Figure E.1 Hydrostatic stress along particle radius at selected times during (a) two phase lithiation, and (b) single phase lithiation.

E.2 Si Nanosphere with Single Phase Lithiation

The single phase lithiation of Si nanosphere with diameter of 500 nm was also studied, with the hydrostatic stress plotted in Fig. E.1(b). Distinct stress state was observed in single-phase lithiation from the two-phase lithiation process. The stress changes smoothly without the existence of the reaction front. The stress changes from compressive near the particle surface to tensile inside. Especially at early stage of lithiation, the particle center experiences high tensile hydrostatic stress, which would easily cause particle to fracture from inside and form hollow spaces. Therefore, by designing hollow structured Si structure would be beneficial to the structural stability and increase cyclability.

BIBLIOGRAPHY

BIBLIOGRAPHY

- 1. Karden, E., Ploumen, S., Fricke, B., Miller, T., & Snyder, K. (2007). Energy storage devices for future hybrid electric vehicles. *Journal of Power Sources*, *168*(1), 2–11. doi:10.1016/j.jpowsour.2006.10.090
- 2. Fischer, M., Werber, M., & Schwartz, P. V. (2009). Batteries: Higher energy density than gasoline? *Energy policy*, *37*(7), 2639–2641.
- 3. Tarascon, J.-M., & Armand, M. (2001). Issues and challenges facing rechargeable lithium batteries. *Nature*, 414(6861), 359–367. doi:10.1038/35104644
- 4. Lithium Ion Battery Component Cost Shares | New Energy and Fuel. (n.d.). Retrieved from http://newenergyandfuel.com/http:/newenergyandfuel/com/2010/02/04/the-battery-explosion-is-coming-part-one/lithium-ion-battery-component-cost-shares/
- 5. Harris, S. J., Timmons, A., Baker, D. R., & Monroe, C. (2010). Direct in situ measurements of Li transport in Li-ion battery negative electrodes. *Chemical Physics Letters*, 485(4–6), 265–274. doi:10.1016/j.cplett.2009.12.033
- 6. Zhang, S. S. (2007). A review on the separators of liquid electrolyte Li-ion batteries. *Journal of Power Sources*, 164(1), 351–364. doi:10.1016/j.jpowsour.2006.10.065
- 7. Wakihara, M. (2001). Recent developments in lithium ion batteries. *Materials Science and Engineering: R: Reports*, *33*(4), 109–134.
- 8. Nishi, Y. (2001). Lithium ion secondary batteries; past 10 years and the future. *Journal of Power Sources*, 100(1–2), 101–106. doi:10.1016/S0378-7753(01)00887-4
- 9. Tirado, J. L. (2003). Inorganic materials for the negative electrode of lithium-ion batteries: state-of-the-art and future prospects. *Materials Science and Engineering: R: Reports*, 40(3), 103–136. doi:10.1016/S0927-796X(02)00125-0
- 10. Li, H., Huang, X., Chen, L., Wu, Z., & Liang, Y. (1999). A High Capacity Nano Si Composite Anode Material for Lithium Rechargeable Batteries. *Electrochemical and Solid-State Letters*, 2(11), 547–549. doi:10.1149/1.1390899
- 11. Kasavajjula, U., Wang, C., & Appleby, A. J. (2007). Nano- and bulk-silicon-based insertion anodes for lithium-ion secondary cells. *Journal of Power Sources*, *163*(2), 1003–1039. doi:10.1016/j.jpowsour.2006.09.084
- 12. Li, J., & Dahn, J. R. (2007). An In Situ X-Ray Diffraction Study of the Reaction of Li with Crystalline Si. *Journal of The Electrochemical Society*, *154*(3), A156–A161. doi:10.1149/1.2409862

- 13. Obrovac, M. N., & Christensen, L. (2004). Structural Changes in Silicon Anodes during Lithium Insertion/Extraction. *Electrochemical and Solid-State Letters*, 7(5), A93–A96. doi:10.1149/1.1652421
- 14. Larcher, D., Beattie, S., Morcrette, M., Edström, K., Jumas, J.-C., & Tarascon, J.-M. (2007). Recent findings and prospects in the field of pure metals as negative electrodes for Li-ion batteries. *Journal of Materials Chemistry*, *17*(36), 3759–3772. doi:10.1039/B705421C
- 15. Beaulieu, L. Y., Hatchard, T. D., Bonakdarpour, A., Fleischauer, M. D., & Dahn, J. R. (2003). Reaction of Li with Alloy Thin Films Studied by In Situ AFM. *Journal of The Electrochemical Society*, *150*(11), A1457–A1464. doi:10.1149/1.1613668
- 16. Sun, C.-F., Karki, K., Jia, Z., Liao, H., Zhang, Y., Li, T., ... Wang, Y. (2013). A Beaded-String Silicon Anode. *ACS Nano*, 7(3), 2717–2724. doi:10.1021/nn4001512
- 17. Timmons, A., & Dahn, J. R. (2007). Isotropic Volume Expansion of Particles of Amorphous Metallic Alloys in Composite Negative Electrodes for Li-Ion Batteries. *Journal of The Electrochemical Society*, *154*(5), A444–A448. doi:10.1149/1.2711075
- 18. Wu, H., & Cui, Y. (2012). Designing nanostructured Si anodes for high energy lithium ion batteries. *Nano Today*, 7(5), 414–429. doi:10.1016/j.nantod.2012.08.004
- 19. Liu, X. H., Zhong, L., Huang, S., Mao, S. X., Zhu, T., & Huang, J. Y. (2012). Size-Dependent Fracture of Silicon Nanoparticles During Lithiation. *ACS Nano*, 6(2), 1522–1531. doi:10.1021/nn204476h
- 20. Huggins, R. A., & Nix, W. D. (2000). Decrepitation model for capacity loss during cycling of alloys in rechargeable electrochemical systems. *Ionics*, 6(1-2), 57–63. doi:10.1007/BF02375547
- 21. Hu, Y., Zhao, X., & Suo, Z. (2010). Averting cracks caused by insertion reaction in lithium—ion batteries. *Journal of Materials Research*, 25(06), 1007–1010. doi:10.1557/JMR.2010.0142
- 22. Liu, G., Xun, S., Vukmirovic, N., Song, X., Olalde-Velasco, P., Zheng, H., ... Yang, W. (2011). Polymers with Tailored Electronic Structure for High Capacity Lithium Battery Electrodes. *Advanced Materials*, 23(40), 4679–4683. doi:10.1002/adma.201102421
- 23. Xun, S., Song, X., Battaglia, V., & Liu, G. (2013). Conductive Polymer Binder-Enabled Cycling of Pure Tin Nanoparticle Composite Anode Electrodes for a Lithium-Ion Battery. *Journal of The Electrochemical Society*, *160*(6), A849–A855. doi:10.1149/2.087306jes
- 24. Yoshio, M., Tsumura, T., & Dimov, N. (2005). Electrochemical behaviors of silicon based anode material. *Journal of Power Sources*, *146*(1–2), 10–14. doi:10.1016/j.jpowsour.2005.03.143

- 25. Liu, W.-R., Wang, J.-H., Wu, H.-C., Shieh, D.-T., Yang, M.-H., & Wu, N.-L. (2005). Electrochemical Characterizations on Si and C-Coated Si Particle Electrodes for Lithium-Ion Batteries. *Journal of The Electrochemical Society*, 152(9), A1719–A1725. doi:10.1149/1.1954967
- 26. Kulova, T. L., Skundin, A. M., Pleskov, Y. V., Terukov, E. I., & Kon'kov, O. I. (2007). Lithium insertion into amorphous silicon thin-film electrodes. *Journal of Electroanalytical Chemistry*, 600(1), 217–225. doi:10.1016/j.jelechem.2006.07.002
- 27. Bourderau, S., Brousse, T., & Schleich, D. (1999). Amorphous silicon as a possible anode material for Li-ion batteries. *Journal of Power Sources*, 81–82, 233–236. doi:10.1016/S0378-7753(99)00194-9
- 28. Ohara, S., Suzuki, J., Sekine, K., & Takamura, T. (2004). A thin film silicon anode for Liion batteries having a very large specific capacity and long cycle life. *Journal of Power Sources*, *136*(2), 303–306. doi:10.1016/j.jpowsour.2004.03.014
- 29. Jung, H., Park, M., Han, S. H., Lim, H., & Joo, S.-K. (2003). Amorphous silicon thin-film negative electrode prepared by low pressure chemical vapor deposition for lithium-ion batteries. *Solid State Communications*, *125*(7–8), 387–390. doi:10.1016/S0038-1098(02)00849-9
- 30. Chan, C. K., Peng, H., Liu, G., McIlwrath, K., Zhang, X. F., Huggins, R. A., & Cui, Y. (2008). High-performance lithium battery anodes using silicon nanowires. *Nature Nanotechnology*, *3*(1), 31–35. doi:10.1038/nnano.2007.411
- 31. Peng, K., Jie, J., Zhang, W., & Lee, S.-T. (2008). Silicon nanowires for rechargeable lithium-ion battery anodes. *Applied Physics Letters*, *93*(3), 033105. doi:doi:10.1063/1.2929373
- 32. Lang, C. M., Cheimets, A. B., Moran, P. D., & Vega, J. A. (2013). Multi-Amp Hour Cell Construction Using PSI's Silicon Whisker and Carbon Nanofiber Composite Anode. *Meeting Abstracts*, *MA2013-02*(14), 977–977.
- 33. Cui, L.-F., Yang, Y., Hsu, C.-M., & Cui, Y. (2009). Carbon–Silicon Core–Shell Nanowires as High Capacity Electrode for Lithium Ion Batteries. *Nano Letters*, *9*(9), 3370–3374. doi:10.1021/nl901670t
- 34. Wang, C.-M., Li, X., Wang, Z., Xu, W., Liu, J., Gao, F., ... Baer, D. R. (2012). In Situ TEM Investigation of Congruent Phase Transition and Structural Evolution of Nanostructured Silicon/Carbon Anode for Lithium Ion Batteries. *Nano Letters*, *12*(3), 1624–1632. doi:10.1021/nl204559u
- 35. Qu, J., Li, H., Henry Jr., J. J., Martha, S. K., Dudney, N. J., Xu, H., ... Dai, S. (2012). Self-aligned Cu–Si core–shell nanowire array as a high-performance anode for Li-ion batteries. *Journal of Power Sources*, *198*, 312–317. doi:10.1016/j.jpowsour.2011.10.004

- 36. Yao, Y., McDowell, M. T., Ryu, I., Wu, H., Liu, N., Hu, L., ... Cui, Y. (2011). Interconnected Silicon Hollow Nanospheres for Lithium-Ion Battery Anodes with Long Cycle Life. *Nano Letters*, *11*(7), 2949–2954. doi:10.1021/nl201470j
- 37. Kim, H., Han, B., Choo, J., & Cho, J. (2008). Three-Dimensional Porous Silicon Particles for Use in High-Performance Lithium Secondary Batteries. *Angewandte Chemie International Edition*, 47(52), 10151–10154. doi:10.1002/anie.200804355
- 38. Choi, J. W., Hu, L., Cui, L., McDonough, J. R., & Cui, Y. (2010). Metal current collector-free freestanding silicon–carbon 1D nanocomposites for ultralight anodes in lithium ion batteries. *Journal of Power Sources*, *195*(24), 8311–8316. doi:10.1016/j.jpowsour.2010.06.108
- 39. Li, J., Dozier, A. K., Li, Y., Yang, F., & Cheng, Y.-T. (2011). Crack Pattern Formation in Thin Film Lithium-Ion Battery Electrodes. *Journal of The Electrochemical Society*, *158*(6), A689–A694. doi:10.1149/1.3574027
- 40. Magasinski, A., Dixon, P., Hertzberg, B., Kvit, A., Ayala, J., & Yushin, G. (2010). High-performance lithium-ion anodes using a hierarchical bottom-up approach. *Nature Materials*, 9(4), 353–358. doi:10.1038/nmat2725
- 41. Wang, J. W., Liu, X. H., Zhao, K., Palmer, A., Patten, E., Burton, D., ... Huang, J. Y. (2012). Sandwich-Lithiation and Longitudinal Crack in Amorphous Silicon Coated on Carbon Nanofibers. *ACS Nano*, 6(10), 9158–9167. doi:10.1021/nn3034343
- 42. McDowell, M. T., Lee, S. W., Harris, J. T., Korgel, B. A., Wang, C., Nix, W. D., & Cui, Y. (2013). In Situ TEM of Two-Phase Lithiation of Amorphous Silicon Nanospheres. *Nano Letters*, *13*(2), 758–764. doi:10.1021/nl3044508
- 43. Chan, C. K., Patel, R. N., O'Connell, M. J., Korgel, B. A., & Cui, Y. (2010). Solution-Grown Silicon Nanowires for Lithium-Ion Battery Anodes. *ACS Nano*, *4*(3), 1443–1450. doi:10.1021/nn901409q
- 44. Liu, X. H., Zheng, H., Zhong, L., Huang, S., Karki, K., Zhang, L. Q., ... Huang, J. Y. (2011). Anisotropic Swelling and Fracture of Silicon Nanowires during Lithiation. *Nano Letters*, *11*(8), 3312–3318.
- 45. Lee, S. W., McDowell, M. T., Choi, J. W., & Cui, Y. (2011). Anomalous Shape Changes of Silicon Nanopillars by Electrochemical Lithiation. *Nano Letters*, *11*(7), 3034–3039.
- 46. Anantharaman, T. R. (1984). *Metallic glasses: production properties and applications*. Aedermannsdorf, Switzerland: Trans Tech Publications.
- 47. Limthongkul, P., Jang, Y.-I., Dudney, N. J., & Chiang, Y.-M. (2003). Electrochemically-driven solid-state amorphization in lithium-silicon alloys and implications for lithium storage. *Acta Materialia*, *51*(4), 1103–1113. doi:10.1016/S1359-6454(02)00514-1

- 48. Ogata, K., Salager, E., Kerr, C. J., Fraser, A. E., Ducati, C., Morris, A. J., ... Grey, C. P. (2014). Revealing lithium–silicide phase transformations in nano-structured silicon-based lithium ion batteries via in situ NMR spectroscopy. *Nature Communications*, *5*. doi:10.1038/ncomms4217
- 49. Ghassemi, H., Au, M., Chen, N., Heiden, P. A., & Yassar, R. S. (2011). In Situ Electrochemical Lithiation/Delithiation Observation of Individual Amorphous Si Nanorods. *ACS Nano*, 5(10), 7805–7811. doi:10.1021/nn2029814
- 50. Wang, J. W., He, Y., Fan, F., Liu, X. H., Xia, S., Liu, Y., ... Zhu, T. (2013). Two-Phase Electrochemical Lithiation in Amorphous Silicon. *Nano Letters*, *13*(2), 709–715. doi:10.1021/nl304379k
- 51. Yang, H., Huang, S., Huang, X., Fan, F., Liang, W., Liu, X. H., ... Zhang, S. (2012). Orientation-Dependent Interfacial Mobility Governs the Anisotropic Swelling in Lithiated Silicon Nanowires. *Nano Letters*, *12*(4), 1953–1958. doi:10.1021/nl204437t
- 52. Goldman, J. L., Long, B. R., Gewirth, A. A., & Nuzzo, R. G. (2011). Strain Anisotropies and Self-Limiting Capacities in Single-Crystalline 3D Silicon Microstructures: Models for High Energy Density Lithium-Ion Battery Anodes. *Advanced Functional Materials*, 21(13), 2412–2422. doi:10.1002/adfm.201002487
- 53. Ryu, I., Choi, J. W., Cui, Y., & Nix, W. D. (2011). Size-dependent fracture of Si nanowire battery anodes. *Journal of the Mechanics and Physics of Solids*, 59(9), 1717–1730. doi:10.1016/j.jmps.2011.06.003
- 54. Liu, X. H., Wang, J. W., Huang, S., Fan, F., Huang, X., Liu, Y., ... Huang, J. Y. (2012). In situ atomic-scale imaging of electrochemical lithiation in silicon. *Nature Nanotechnology*, 7(11), 749–756. doi:10.1038/nnano.2012.170
- 55. Bower, A. F. (2009). *Applied Mechanics of Solids* (1 edition.). Boca Raton: CRC Press.
- 56. Hill, R. (1998). *The Mathematical Theory of Plasticity*. Oxford: New York: Oxford University Press.
- 57. Zhao, K., Pharr, M., Cai, S., Vlassak, J. J., & Suo, Z. (2011). Large Plastic Deformation in High-Capacity Lithium-Ion Batteries Caused by Charge and Discharge. *Journal of the American Ceramic Society*, 94, s226–s235. doi:10.1111/j.1551-2916.2011.04432.x
- 58. Brassart, L., Zhao, K., & Suo, Z. (2013). Cyclic plasticity and shakedown in high-capacity electrodes of lithium-ion batteries. *International Journal of Solids and Structures*, 50(7–8), 1120–1129. doi:10.1016/j.ijsolstr.2012.12.019
- 59. Jirasek, M., & Bazant, Z. P. (2002). *Inelastic Analysis of Structures*. John Wiley & Sons.
- 60. Sethuraman, V. A., Chon, M. J., Shimshak, M., Srinivasan, V., & Guduru, P. R. (2010). In situ measurements of stress evolution in silicon thin films during electrochemical lithiation

- and delithiation. *Journal of Power Sources*, *195*(15), 5062–5066. doi:10.1016/j.jpowsour.2010.02.013
- 61. McDowell, M. T., Ryu, I., Lee, S. W., Wang, C., Nix, W. D., & Cui, Y. (2012). Studying the Kinetics of Crystalline Silicon Nanoparticle Lithiation with In Situ Transmission Electron Microscopy. *Advanced Materials*, 24(45), 6034–6041. doi:10.1002/adma.201202744
- 62. Luo, L., Wu, J., Luo, J., Huang, J., & Dravid, V. P. (2014). Dynamics of Electrochemical Lithiation/Delithiation of Graphene-Encapsulated Silicon Nanoparticles Studied by In-situ TEM. *Scientific Reports*, 4. doi:10.1038/srep03863
- 63. Bucci, G., Nadimpalli, S. P. V., Sethuraman, V. A., Bower, A. F., & Guduru, P. R. (2014). Measurement and modeling of the mechanical and electrochemical response of amorphous Si thin film electrodes during cyclic lithiation. *Journal of the Mechanics and Physics of Solids*, 62, 276–294. doi:10.1016/j.jmps.2013.10.005
- 64. Zhao, K., Pharr, M., Wan, Q., Wang, W. L., Kaxiras, E., Vlassak, J. J., & Suo, Z. (2012). Concurrent Reaction and Plasticity during Initial Lithiation of Crystalline Silicon in Lithium-Ion Batteries. *Journal of The Electrochemical Society*, 159(3), A238–A243. doi:10.1149/2.020203jes
- 65. Zhao, K., Tritsaris, G. A., Pharr, M., Wang, W. L., Okeke, O., Suo, Z., ... Kaxiras, E. (2012). Reactive Flow in Silicon Electrodes Assisted by the Insertion of Lithium. *Nano Letters*, *12*(8), 4397–4403. doi:10.1021/nl302261w
- 66. Kushima, A., Huang, J. Y., & Li, J. (2012). Quantitative Fracture Strength and Plasticity Measurements of Lithiated Silicon Nanowires by In Situ TEM Tensile Experiments. *ACS Nano*, 6(11), 9425–9432. doi:10.1021/nn3037623
- 67. Levitas, V. I., & Attariani, H. (2013). Anisotropic Compositional Expansion and Chemical Potential for Amorphous Lithiated Silicon under Stress Tensor. *Scientific Reports*, *3*. doi:10.1038/srep01615
- 68. Crank, J. (1980). *The Mathematics of Diffusion* (2 edition.). Oxford: Oxford University Press.
- 69. Sukharev, V., Zschech, E., & Nix, W. D. (2007). A model for electromigration-induced degradation mechanisms in dual-inlaid copper interconnects: Effect of microstructure. *Journal of Applied Physics*, *102*(5), 053505. doi:10.1063/1.2775538
- 70. Li, J. C. M. (1981). Chemical potential for diffusion in a stressed solid. *Scripta Metallurgica*, *15*(1), 21–28. doi:10.1016/0036-9748(81)90130-7
- 71. van Loo, F. J. J. (1990). Multiphase diffusion in binary and ternary solid-state systems. *Progress in Solid State Chemistry*, 20(1), 47–99. doi:10.1016/0079-6786(90)90007-3
- 72. Borg, R. J., & Dienes, G. J. (2012). An Introduction to Solid State Diffusion. Elsevier.

- 73. Crank, J. (1975). *The mathematics of diffusion* (Vol. 2). Clarendon press Oxford.
- 74. Gao, Y. F., Cho, M., & Zhou, M. (2013). Mechanical reliability of alloy-based electrode materials for rechargeable Li-ion batteries. *Journal of Mechanical Science and Technology*, 27(5), 1205–1224. doi:10.1007/s12206-013-0401-7
- 75. Haftbaradaran, H., Gao, H., & Curtin, W. A. (2010). A surface locking instability for atomic intercalation into a solid electrode. *Applied Physics Letters*, *96*(9), 091909. doi:10.1063/1.3330940
- 76. Bower, A. F., Guduru, P. R., & Sethuraman, V. A. (2011). A finite strain model of stress, diffusion, plastic flow, and electrochemical reactions in a lithium-ion half-cell. *Journal of the Mechanics and Physics of Solids*, 59(4), 804–828. doi:10.1016/j.jmps.2011.01.003
- 77. Cui, Z., Gao, F., & Qu, J. (2012). A finite deformation stress-dependent chemical potential and its applications to lithium ion batteries. *Journal of the Mechanics and Physics of Solids*, 60(7), 1280–1295. doi:10.1016/j.jmps.2012.03.008
- 78. Levitas, V. I., & Attariani, H. (2014). Anisotropic compositional expansion in elastoplastic materials and corresponding chemical potential: Large-strain formulation and application to amorphous lithiated silicon. *Journal of the Mechanics and Physics of Solids*, 69, 84–111. doi:10.1016/j.jmps.2014.04.012
- 79. Chakraborty, J., Please, C. P., Goriely, A., & Chapman, S. J. (2015). Combining mechanical and chemical effects in the deformation and failure of a cylindrical electrode particle in a Li-ion battery. *International Journal of Solids and Structures*, *54*, 66–81. doi:10.1016/j.ijsolstr.2014.11.006
- 80. Porter, D. A., & Easterling, K. E. (1992). *Phase Transformations in Metals and Alloys, Third Edition (Revised Reprint)*. CRC Press.
- 81. McPherson, J. W. (1986). Stress Dependent Activation Energy. In *Reliability Physics Symposium*, 1986. 24th Annual (pp. 12–18). Presented at the Reliability Physics Symposium, 1986. 24th Annual. doi:10.1109/IRPS.1986.362105
- 82. Haftbaradaran, H., Song, J., Curtin, W. A., & Gao, H. (2011). Continuum and atomistic models of strongly coupled diffusion, stress, and solute concentration. *Journal of Power Sources*, 196(1), 361–370. doi:10.1016/j.jpowsour.2010.06.080
- 83. Yang, F. (2005). Interaction between diffusion and chemical stresses. *Materials Science and Engineering: A*, 409(1–2), 153–159. doi:10.1016/j.msea.2005.05.117
- 84. Gao, Y. F., Cho, M., & Zhou, M. (2013). Stress relaxation through interdiffusion in amorphous lithium alloy electrodes. *Journal of the Mechanics and Physics of Solids*, 61(2), 579–596. doi:10.1016/j.jmps.2012.09.004

- 85. Johari, P., Qi, Y., & Shenoy, V. B. (2011). The Mixing Mechanism during Lithiation of Si Negative Electrode in Li-Ion Batteries: An Ab Initio Molecular Dynamics Study. *Nano Letters*, *11*(12), 5494–5500. doi:10.1021/nl203302d
- 86. Larché, F., & Cahn, J. W. (1973). A linear theory of thermochemical equilibrium of solids under stress. *Acta Metallurgica*, *21*(8), 1051–1063. doi:10.1016/0001-6160(73)90021-7
- 87. Larché, F. C., & Cahn, J. l. (1982). The effect of self-stress on diffusion in solids. *Acta Metallurgica*, *30*(10), 1835–1845. doi:10.1016/0001-6160(82)90023-2
- 88. Larché, F. C., & Cahn, J. W. (1985). Overview no. 41 The interactions of composition and stress in crystalline solids. *Acta Metallurgica*, *33*(3), 331–357. doi:10.1016/0001-6160(85)90077-X
- 89. Hay, R. S., & Evans, B. (1987). Chemically induced grain boundary migration in calcite: temperature dependence, phenomenology, and possible applications to geologic systems. *Contributions to Mineralogy and Petrology*, *97*(1), 127–141. doi:10.1007/BF00375220
- 90. Kikuchi, R., & Cahn, J. W. (1979). Theory of interphase and antiphase boundaries in f.c.c. alloys. *Acta Metallurgica*, 27(8), 1337–1353. doi:10.1016/0001-6160(79)90203-7
- 91. Guo, Z.-S., Zhang, T., Zhu, J., & Wang, Y. (2014). Effects of hydrostatic pressure and modulus softening on electrode curvature and stress in a bilayer electrode plate. *Computational Materials Science*, *94*, 218–224. doi:10.1016/j.commatsci.2014.04.019
- 92. Sheldon, B. W., Soni, S. K., Xiao, X., & Qi, Y. (2011). Stress Contributions to Solution Thermodynamics in Li-Si Alloys. *Electrochemical and Solid-State Letters*, *15*(1), A9–A11. doi:10.1149/2.016201es1
- 93. Verbrugge, M. W., & Koch, B. J. (1996). Modeling Lithium Intercalation of Single-Fiber Carbon Microelectrodes. *Journal of The Electrochemical Society*, *143*(2), 600–608. doi:10.1149/1.1836486
- 94. Ding, N., Xu, J., Yao, Y. X., Wegner, G., Fang, X., Chen, C. H., & Lieberwirth, I. (2009). Determination of the diffusion coefficient of lithium ions in nano-Si. *Solid State Ionics*, 180(2–3), 222–225. doi:10.1016/j.ssi.2008.12.015
- 95. Yoshimura, K., Suzuki, J., Sekine, K., & Takamura, T. (2007). Measurement of the diffusion rate of Li in silicon by the use of bipolar cells. *Journal of Power Sources*, *174*(2), 653–657. doi:10.1016/j.ipowsour.2007.06.115
- 96. Kulova, T. L., Pleskov, Y. V., Skundin, A. M., Terukov, E. I., & Kon'kov, O. I. (2006). Lithium intercalation into amorphous-silicon thin films: An electrochemical-impedance study. *Russian Journal of Electrochemistry*, *42*(7), 708–714. doi:10.1134/S1023193506070032
- 97. Li, J., Xiao, X., Yang, F., Verbrugge, M. W., & Cheng, Y.-T. (2012). Potentiostatic Intermittent Titration Technique for Electrodes Governed by Diffusion and Interfacial

- Reaction. *The Journal of Physical Chemistry C*, *116*(1), 1472–1478. doi:10.1021/jp207919q
- 98. Xie, J., Imanishi, N., Zhang, T., Hirano, A., Takeda, Y., & Yamamoto, O. (2010). Li-ion diffusion in amorphous Si films prepared by RF magnetron sputtering: A comparison of using liquid and polymer electrolytes. *Materials Chemistry and Physics*, *120*(2–3), 421–425. doi:10.1016/j.matchemphys.2009.11.031
- 99. Xia, H., Tang, S., & Lu, L. (2007). Properties of amorphous Si thin film anodes prepared by pulsed laser deposition. *Materials Research Bulletin*, 42(7), 1301–1309. doi:10.1016/j.materresbull.2006.10.007
- 100. Chon, M. J., Sethuraman, V. A., McCormick, A., Srinivasan, V., & Guduru, P. R. (2011). Real-Time Measurement of Stress and Damage Evolution during Initial Lithiation of Crystalline Silicon. *Physical Review Letters*, *107*(4), 045503. doi:10.1103/PhysRevLett.107.045503
- 101. Sethuraman, V. A., Van Winkle, N., Abraham, D. P., Bower, A. F., & Guduru, P. R. (2012). Real-time stress measurements in lithium-ion battery negative-electrodes. *Journal of Power Sources*, 206, 334–342. doi:10.1016/j.jpowsour.2012.01.036
- 102. Sethuraman, V. A., Chon, M. J., Shimshak, M., Van Winkle, N., & Guduru, P. R. (2010). In situ measurement of biaxial modulus of Si anode for Li-ion batteries. *Electrochemistry Communications*, *12*(11), 1614–1617. doi:10.1016/j.elecom.2010.09.008
- 103. Hertzberg, B., Benson, J., & Yushin, G. (2011). Ex-situ depth-sensing indentation measurements of electrochemically produced Si–Li alloy films. *Electrochemistry Communications*, *13*(8), 818–821. doi:10.1016/j.elecom.2011.05.011
- 104. Berla, L. A., Lee, S. W., Cui, Y., & Nix, W. D. (2015). Mechanical behavior of electrochemically lithiated silicon. *Journal of Power Sources*, 273, 41–51.
- 105. Zhao, K., Wang, W. L., Gregoire, J., Pharr, M., Suo, Z., Vlassak, J. J., & Kaxiras, E. (2011). Lithium-Assisted Plastic Deformation of Silicon Electrodes in Lithium-Ion Batteries: A First-Principles Theoretical Study. *Nano Letters*, 11(7), 2962–2967. doi:10.1021/nl201501s
- 106. Chou, C.-Y., & Hwang, G. S. (2013). Surface effects on the structure and lithium behavior in lithiated silicon: A first principles study. *Surface Science*, 612, 16–23. doi:10.1016/j.susc.2013.02.004
- 107. McDowell, M. T., & Cui, Y. (2011). Single Nanostructure Electrochemical Devices for Studying Electronic Properties and Structural Changes in Lithiated Si Nanowires. *Advanced Energy Materials*, 1(5), 894–900. doi:10.1002/aenm.201100258
- 108. Shenoy, V. B., Johari, P., & Qi, Y. (2010). Elastic softening of amorphous and crystalline Li–Si Phases with increasing Li concentration: A first-principles study. *Journal of Power Sources*, 195(19), 6825–6830. doi:10.1016/j.jpowsour.2010.04.044

- 109. Mr. Green Car: Recycling electric vehicle batteries |. (2012, November 28). *The Rock River Times*. Retrieved from http://rockrivertimes.com/2012/11/28/mr-green-car-recycling-electric-vehicle-batteries/
- 110. Xu, Z.-L., Gang, Y., Akbari Garakani, M., Abouali, S., Huang, J.-Q., & Kim, J.-K. (2016). Carbon-coated mesoporous silicon microsphere anodes with greatly reduced volume expansion. *Journal of Materials Chemistry A*, *4*(16), 6098–6106. doi:10.1039/C6TA01344A
- 111. Kim, H. S., Jeong, T.-G., & Kim, Y.-T. (2016). Electrochemical Properties of Lithium Sulfur Battery with Silicon Anodes Lithiated by Direct Contact Method. *Journal of Electrochemical Science and Technology*, 7(3), 228–233. doi:10.5229/JECST.2016.7.3.228
- 112. Alhanouti, M., Gießler, M., Blank, T., & Gauterin, F. (2016). New Electro-Thermal Battery Pack Model of an Electric Vehicle. *Energies*, 9(7), 563. doi:10.3390/en9070563
- 113. Studying Impedance to Analyze the Li-Ion Battery with an App. (n.d.). *COMSOL Multiphysics*©. Retrieved from https://www.comsol.com/blogs/studying-impedance-to-analyze-the-li-ion-battery-with-an-app/
- 114. Wu, W., Xiao, X., Wang, M., & Huang, X. (2014). A Microstructural Resolved Model for the Stress Analysis of Lithium-Ion Batteries. *Journal of The Electrochemical Society*, *161*(5), A803–A813. doi:10.1149/2.082405jes
- 115. Wang, M., Xiao, X., & Huang, X. (2016). Study of lithium diffusivity in amorphous silicon via finite element analysis. *Journal of Power Sources*, *307*, 77–85. doi:10.1016/j.jpowsour.2015.12.082
- 116. Deshpande, R., Qi, Y., & Cheng, Y.-T. (2010). Effects of Concentration-Dependent Elastic Modulus on Diffusion-Induced Stresses for Battery Applications. *Journal of The Electrochemical Society*, *157*(8), A967–A971. doi:10.1149/1.3454762
- 117. Deshpande, R., Cheng, Y.-T., Verbrugge, M. W., & Timmons, A. (2011). Diffusion Induced Stresses and Strain Energy in a Phase-Transforming Spherical Electrode Particle. *Journal of The Electrochemical Society*, *158*(6), A718–A724. doi:10.1149/1.3565183
- 118. Sethuraman, V. A., Srinivasan, V., & Newman, J. (2013). Analysis of Electrochemical Lithiation and Delithiation Kinetics in Silicon. *Journal of The Electrochemical Society*, *160*(2), A394–A403. doi:10.1149/2.008303jes
- 119. Drozdov, A. D. (2014). A model for the mechanical response of electrode particles induced by lithium diffusion in Li-ion batteries. *Acta Mechanica*, 225(11), 2987–3005. doi:10.1007/s00707-014-1096-2
- 120. Drozdov, A. D. (2014). Viscoplastic response of electrode particles in Li-ion batteries driven by insertion of lithium. *International Journal of Solids and Structures*, *51*(3–4), 690–705. doi:10.1016/j.ijsolstr.2013.10.033

- 121. Haftbaradaran, H., Xiao, X., & Gao, H. (2013). Critical film thickness for fracture in thinfilm electrodes on substrates in the presence of interfacial sliding. *Modelling and Simulation in Materials Science and Engineering*, 21(7), 074008. doi:10.1088/0965-0393/21/7/074008
- 122. Huang, X., Pu, H., Chang, J., Cui, S., Hallac, P. B., Jiang, J., ... Chen, J. (2013). Improved Cyclic Performance of Si Anodes for Lithium-Ion Batteries by Forming Intermetallic Interphases between Si Nanoparticles and Metal Microparticles. *ACS Applied Materials & Interfaces*, 5(22), 11965–11970. doi:10.1021/am403718u
- 123. Grantab, R., & Shenoy, V. B. (2012). Pressure-Gradient Dependent Diffusion and Crack Propagation in Lithiated Silicon Nanowires. *Journal of The Electrochemical Society*, 159(5), A584–A591. doi:10.1149/2.072205jes
- 124. Higa, K., & Srinivasan, V. (2015). Stress and Strain in Silicon Electrode Models. *Journal of The Electrochemical Society*, *162*(6), A1111–A1122. doi:10.1149/2.0091507jes
- 125. Pharr, M., Zhao, K., Wang, X., Suo, Z., & Vlassak, J. J. (2012). Kinetics of Initial Lithiation of Crystalline Silicon Electrodes of Lithium-Ion Batteries. *Nano Letters*, *12*(9), 5039–5047. doi:10.1021/nl302841y
- 126. Freund, L. B., & Suresh, S. (2009). *Thin Film Materials: Stress, Defect Formation and Surface Evolution* (1 edition.). Cambridge, England; New York: Cambridge University Press.
- 127. Gao, Y. F., & Zhou, M. (2011). Strong stress-enhanced diffusion in amorphous lithium alloy nanowire electrodes. *Journal of Applied Physics*, *109*(1), 014310–014310–6. doi:doi:10.1063/1.3530738
- 128. Pal, S., Damle, S. S., Patel, S. H., Datta, M. K., Kumta, P. N., & Maiti, S. (2014). Modeling the delamination of amorphous-silicon thin film anode for lithium-ion battery. *Journal of Power Sources*, 246, 149–159. doi:10.1016/j.jpowsour.2013.06.089
- 129. Gwak, Y., Moon, J., & Cho, M. (2016). Multi-scale analysis of an electrochemical model including coupled diffusion, stress, and nonideal solution in a silicon thin film anode. *Journal of Power Sources*, *307*, 856–865. doi:10.1016/j.jpowsour.2016.01.037
- 130. Doyle, M., Fuller, T. F., & Newman, J. (1993). Modeling of Galvanostatic Charge and Discharge of the Lithium/Polymer/Insertion Cell. *Journal of The Electrochemical Society*, 140(6), 1526–1533. doi:10.1149/1.2221597
- 131. Doyle, M., Newman, J., Gozdz, A. S., Schmutz, C. N., & Tarascon, J.-M. (1996). Comparison of Modeling Predictions with Experimental Data from Plastic Lithium Ion Cells. *Journal of The Electrochemical Society*, *143*(6), 1890–1903. doi:10.1149/1.1836921
- 132. Wang, C.-W., & Sastry, A. M. (2007). Mesoscale Modeling of a Li-Ion Polymer Cell. *Journal of The Electrochemical Society*, *154*(11), A1035–A1047. doi:10.1149/1.2778285

- 133. Wu, W., Xiao, X., & Huang, X. (2012). The effect of battery design parameters on heat generation and utilization in a Li-ion cell. *Electrochimica Acta*, 83, 227–240. doi:10.1016/j.electacta.2012.07.081
- 134. Gu, W. B., & Wang, C. Y. (2000). Thermal-Electrochemical Modeling of Battery Systems. *Journal of The Electrochemical Society*, 147(8), 2910–2922. doi:10.1149/1.1393625
- 135. Kumaresan, K., Sikha, G., & White, R. E. (2008). Thermal Model for a Li-Ion Cell. *Journal of The Electrochemical Society*, *155*(2), A164–A171. doi:10.1149/1.2817888
- 136. Xiao, X., Wu, W., & Huang, X. (2010). A multi-scale approach for the stress analysis of polymeric separators in a lithium-ion battery. *Journal of Power Sources*, 195(22), 7649–7660. doi:10.1016/j.jpowsour.2010.06.020
- 137. Wu, W., Xiao, X., Huang, X., & Yan, S. (2014). A multiphysics model for the in situ stress analysis of the separator in a lithium-ion battery cell. *Computational Materials Science*, 83, 127–136. doi:10.1016/j.commatsci.2013.10.002
- 138. Chandrasekaran, R., & Fuller, T. F. (2011). Analysis of the Lithium-Ion Insertion Silicon Composite Electrode/Separator/Lithium Foil Cell. *Journal of The Electrochemical Society*, *158*(8), A859–A871. doi:10.1149/1.3589301
- 139. Newman, J., & Thomas-Alyea, K. E. (2004). *Electrochemical Systems*. John Wiley & Sons.
- 140. Xu, R., Vasconcelos, L. S. de, & Zhao, K. (2016). Computational analysis of chemomechanical behaviors of composite electrodes in Li-ion batteries. *Journal of Materials Research*, *31*(18), 2715–2727. doi:10.1557/jmr.2016.302
- 141. Shewmon, P. (1991). Diffusion in Solids (2 edition.). Warrendale, Pa: Wiley.
- 142. Barsoum, M., & Barsoum, M. W. (2002). *Fundamentals of Ceramics* (1 edition.). Bristol: CRC Press.
- 143. Cheng, Y.-T., & Verbrugge, M. W. (2008). The influence of surface mechanics on diffusion induced stresses within spherical nanoparticles. *Journal of Applied Physics*, 104(8), 083521–083521–6. doi:doi:10.1063/1.3000442
- 144. Golmon, S., Maute, K., Lee, S.-H., & Dunn, M. L. (2010). Stress generation in silicon particles during lithium insertion. *Applied Physics Letters*, 97(3), 033111–033111–3. doi:doi:10.1063/1.3458707
- 145. McDowell, M. T., Lee, S. W., Ryu, I., Wu, H., Nix, W. D., Choi, J. W., & Cui, Y. (2011). Novel Size and Surface Oxide Effects in Silicon Nanowires as Lithium Battery Anodes. *Nano Letters*, *11*(9), 4018–4025. doi:10.1021/nl202630n

- 146. Christensen, J., & Newman, J. (2006). Stress generation and fracture in lithium insertion materials. *Journal of Solid State Electrochemistry*, 10(5), 293–319. doi:10.1007/s10008-006-0095-1
- 147. Yang, B., He, Y.-P., Irsa, J., Lundgren, C. A., Ratchford, J. B., & Zhao, Y.-P. (2012). Effects of composition-dependent modulus, finite concentration and boundary constraint on Li-ion diffusion and stresses in a bilayer Cu-coated Si nano-anode. *Journal of Power Sources*, 204, 168–176. doi:10.1016/j.jpowsour.2012.01.029
- 148. Cheng, Y.-T., & Verbrugge, M. W. (2010). Diffusion-Induced Stress, Interfacial Charge Transfer, and Criteria for Avoiding Crack Initiation of Electrode Particles. *Journal of The Electrochemical Society*, *157*(4), A508–A516. doi:10.1149/1.3298892
- 149. An, Y., & Jiang, H. (2013). A finite element simulation on transient large deformation and mass diffusion in electrodes for lithium ion batteries. *Modelling and Simulation in Materials Science and Engineering*, 21(7), 074007. doi:10.1088/0965-0393/21/7/074007
- 150. Zhang, X., Shyy, W., & Sastry, A. M. (2007). Numerical Simulation of Intercalation-Induced Stress in Li-Ion Battery Electrode Particles. *Journal of The Electrochemical Society*, *154*(10), A910–A916. doi:10.1149/1.2759840
- 151. Obrovac, M. N., Christensen, L., Le, D. B., & Dahn, J. R. (2007). Alloy Design for Lithium-Ion Battery Anodes. *Journal of The Electrochemical Society*, *154*(9), A849–A855. doi:10.1149/1.2752985
- 152. Wiley: Lithium Ion Batteries: Fundamentals and Performance Masataka Wakihara, Osamu Yamamoto. (n.d.). Retrieved May 6, 2016, from http://www.wiley.com/WileyCDA/WileyTitle/productCd-3527611983.html
- 153. Manthiram, A. (2011). Materials Challenges and Opportunities of Lithium Ion Batteries. *The Journal of Physical Chemistry Letters*, 2(3), 176–184. doi:10.1021/jz1015422
- 154. Zhang, X., Sastry, A. M., & Shyy, W. (2008). Intercalation-Induced Stress and Heat Generation within Single Lithium-Ion Battery Cathode Particles. *Journal of The Electrochemical Society*, *155*(7), A542–A552. doi:10.1149/1.2926617
- 155. Wang, M., & Xiao, X. (2016). Investigation of the chemo-mechanical coupling in lithiation/delithiation of amorphous Si through simulations of Si thin films and Si nanospheres. *Journal of Power Sources*, 326, 365–376. doi:10.1016/j.jpowsour.2016.07.011
- 156. Heat Transfer in Deformed Solids. (2014, May 28). *COMSOL Blog*. Retrieved from http://www.comsol.com/blogs/heat-transfer-deformed-solids/
- 157. Standards & Properties: Mechanical Properties of Copper and Copper Alloys at Low Temperatures. (n.d.). Retrieved October 29, 2016, from https://www.copper.org/resources/properties/144_8/

- 158. International, A. S. M. (2002). Atlas of Stress-strain Curves. ASM International.
- 159. Lee, S.-I., Jung, U.-H., Kim, Y.-S., Kim, M.-H., Ahn, D.-J., & Chun, H.-S. (n.d.). A study of electrochemical kinetics of lithium ion in organic electrolytes. *Korean Journal of Chemical Engineering*, *19*(4), 638–644. doi:10.1007/BF02699310
- 160. Dougassa, Y. R., Jacquemin, J., Ouatani, L. El, Tessier, C., & Anouti, M. (2014). Viscosity and Carbon Dioxide Solubility for LiPF6, LiTFSI, and LiFAP in Alkyl Carbonates: Lithium Salt Nature and Concentration Effect. *The Journal of Physical Chemistry B*, 118(14), 3973–3980. doi:10.1021/jp500063c
- 161. Wu, W., Xiao, X., Wang, M., & Huang, X. (2014). A Microstructural Resolved Model for the Stress Analysis of Lithium-Ion Batteries. *Journal of The Electrochemical Society*, *161*(5), A803–A813. doi:10.1149/2.082405jes
- 162. Wu, J. J., & Bennett, W. R. (2012). Fundamental investigation of Si anode in Li-Ion cells. In 2012 IEEE Energytech (pp. 1–5). Presented at the 2012 IEEE Energytech. doi:10.1109/EnergyTech.2012.6304667
- 163. Misra, S., Liu, N., Nelson, J., Hong, S. S., Cui, Y., & Toney, M. F. (2012). In Situ X-ray Diffraction Studies of (De)lithiation Mechanism in Silicon Nanowire Anodes. *ACS Nano*, 6(6), 5465–5473. doi:10.1021/nn301339g
- 164. Liu, X. H., Zhang, L. Q., Zhong, L., Liu, Y., Zheng, H., Wang, J. W., ... Huang, J. Y. (2011). Ultrafast Electrochemical Lithiation of Individual Si Nanowire Anodes. *Nano Letters*, 11(6), 2251–2258. doi:10.1021/nl200412p
- 165. Wang, J. W., He, Y., Fan, F., Liu, X. H., Xia, S., Liu, Y., ... Zhu, T. (2013). Two-Phase Electrochemical Lithiation in Amorphous Silicon. *Nano Letters*, *13*(2), 709–715. doi:10.1021/nl304379k
- 166. Kim, S.-P., Datta, D., & Shenoy, V. B. (2014). Atomistic Mechanisms of Phase Boundary Evolution during Initial Lithiation of Crystalline Silicon. *The Journal of Physical Chemistry C*, 118(31), 17247–17253. doi:10.1021/jp502523t
- 167. Berla, L. A., Lee, S. W., Ryu, I., Cui, Y., & Nix, W. D. (2014). Robustness of amorphous silicon during the initial lithiation/delithiation cycle. *Journal of Power Sources*, 258, 253–259. doi:10.1016/j.jpowsour.2014.02.032
- 168. Pharr, M., Suo, Z., & Vlassak, J. J. (2014). Variation of stress with charging rate due to strain-rate sensitivity of silicon electrodes of Li-ion batteries. *Journal of Power Sources*, 270, 569–575. doi:10.1016/j.jpowsour.2014.07.153
- 169. Kim, C.-U. (2011). *Electromigration in Thin Films and Electronic Devices: Materials and Reliability*. Elsevier.

- 170. Liu, X., Zhou, Y., Zheng, X., & Wang, J. (2012). Charging efficiency improvement by structuring lithium battery electrodes. *Journal of Applied Physics*, 111(11), 114303. doi:10.1063/1.4723553
- 171. Swaminathan, N., & Qu, J. (2007). Interactions Between Non-Stoichiometric Stresses and Defect Transport in a Tubular Electrolyte. *Fuel Cells*, 7(6), 453–462. doi:10.1002/fuce.200700027
- 172. Sethuraman, V. A., Srinivasan, V., Bower, A. F., & Guduru, P. R. (2010). In Situ Measurements of Stress-Potential Coupling in Lithiated Silicon. *Journal of The Electrochemical Society*, *157*(11), A1253–A1261. doi:10.1149/1.3489378
- 173. Li, J., Dudney, N. J., Xiao, X., Cheng, Y.-T., Liang, C., & Verbrugge, M. W. (2015). Asymmetric Rate Behavior of Si Anodes for Lithium-Ion Batteries: Ultrafast De-Lithiation versus Sluggish Lithiation at High Current Densities. *Advanced Energy Materials*, 5(6), 1401627. doi:10.1002/aenm.201401627
- 174. Liu, N., Wu, H., McDowell, M. T., Yao, Y., Wang, C., & Cui, Y. (2012). A Yolk-Shell Design for Stabilized and Scalable Li-Ion Battery Alloy Anodes. *Nano Letters*, *12*(6), 3315–3321. doi:10.1021/nl3014814
- 175. Liu, P., Sridhar, N., & Zhang, Y.-W. (2012). Lithiation-induced tensile stress and surface cracking in silicon thin film anode for rechargeable lithium battery. *Journal of Applied Physics*, *112*(9), 093507–093507–5. doi:doi:10.1063/1.4764329
- 176. Stoney, G. G. (1909). The Tension of Metallic Films Deposited by Electrolysis. *Proceedings of the Royal Society of London. Series A*, 82(553), 172–175. doi:10.1098/rspa.1909.0021
- 177. Janssen, G. C. A. M., Abdalla, M. M., van Keulen, F., Pujada, B. R., & van Venrooy, B. (2009). Celebrating the 100th anniversary of the Stoney equation for film stress: Developments from polycrystalline steel strips to single crystal silicon wafers. *Thin Solid Films*, *517*(6), 1858–1867. doi:10.1016/j.tsf.2008.07.014
- 178. Wu, H., Chan, G., Choi, J. W., Ryu, I., Yao, Y., McDowell, M. T., ... Cui, Y. (2012). Stable cycling of double-walled silicon nanotube battery anodes through solid-electrolyte interphase control. *Nature Nanotechnology*, 7(5), 310–315. doi:10.1038/nnano.2012.35
- 179. Smith, M., García, R. E., & Horn, Q. C. (2009). The Effect of Microstructure on the Galvanostatic Discharge of Graphite Anode Electrodes in LiCoO2-Based Rocking-Chair Rechargeable Batteries. *Journal of The Electrochemical Society*, *156*(11), A896–A904. doi:10.1149/1.3216000
- 180. Less, G. B., Seo, J. H., Han, S., Sastry, A. M., Zausch, J., Latz, A., ... Fell, S. (2012). Micro-Scale Modeling of Li-Ion Batteries: Parameterization and Validation. *Journal of The Electrochemical Society*, *159*(6), A697–A704. doi:10.1149/2.096205jes

- 181. Yan, B., Lim, C., Yin, L., & Zhu, L. (2012). Three Dimensional Simulation of Galvanostatic Discharge of LiCoO2 Cathode Based on X-ray Nano-CT Images. *Journal of The Electrochemical Society*, *159*(10), A1604–A1614. doi:10.1149/2.024210jes
- 182. Zhang, C., Santhanagopalan, S., Sprague, M. A., & Pesaran, A. A. (2015). Coupled mechanical-electrical-thermal modeling for short-circuit prediction in a lithium-ion cell under mechanical abuse. *Journal of Power Sources*, 290, 102–113. doi:10.1016/j.jpowsour.2015.04.162
- 183. Pannala, S., Turner, J. A., Allu, S., Elwasif, W. R., Kalnaus, S., Simunovic, S., ... Nanda, J. (2015). Multiscale modeling and characterization for performance and safety of lithium-ion batteries. *Journal of Applied Physics*, 118(7), 072017.
- 184. Chevrier, V. L., & Dahn, J. R. (2009). First Principles Model of Amorphous Silicon Lithiation. *Journal of The Electrochemical Society*, *156*(6), A454–A458. doi:10.1149/1.3111037
- 185. Valøen, L. O., & Reimers, J. N. (2005). Transport Properties of LiPF6-Based Li-Ion Battery Electrolytes. *Journal of The Electrochemical Society*, *152*(5), A882–A891. doi:10.1149/1.1872737
- 186. Dahbi, M., Ghamouss, F., Tran-Van, F., Lemordant, D., & Anouti, M. (2011). Comparative study of EC/DMC LiTFSI and LiPF6 electrolytes for electrochemical storage. *Journal of Power Sources*, 196(22), 9743–9750. doi:10.1016/j.jpowsour.2011.07.071
- 187. Song, J. Y., Wang, Y. Y., & Wan, C. C. (2000). Conductivity Study of Porous Plasticized Polymer Electrolytes Based on Poly(vinylidene fluoride) A Comparison with Polypropylene Separators. *Journal of The Electrochemical Society*, *147*(9), 3219–3225. doi:10.1149/1.1393886
- 188. Zhang, S. S., Jow, T. R., Amine, K., & Henriksen, G. L. (2002). LiPF6–EC–EMC electrolyte for Li-ion battery. *Journal of Power Sources*, *107*(1), 18–23. doi:10.1016/S0378-7753(01)00968-5
- 189. Wenige, R., Niemann, M., Heider, U., Jungnitz, M., & Hilarius, V. (n.d.). Liquid Electrolyte Systems For Advanced Lithium Batteries. Merck KGaA, D-64271 Darmtadt, Germany. Retrieved July 7, 2016, from https://www.cheric.org/PDF/Symposium/S-J2-0063.pdf
- 190. Chandrasekaran, R., Magasinski, A., Yushin, G., & Fuller, T. F. (2010). Analysis of Lithium Insertion/Deinsertion in a Silicon Electrode Particle at Room Temperature. *Journal of The Electrochemical Society*, 157(10), A1139–A1151. doi:10.1149/1.3474225
- 191. Baggetto, L., Niessen, R. A. H., Roozeboom, F., & Notten, P. H. L. (2008). High Energy Density All-Solid-State Batteries: A Challenging Concept Towards 3D Integration. Advanced Functional Materials, 18(7), 1057–1066. doi:10.1002/adfm.200701245

- 192. Li, J., Xiao, X., Yang, F., Verbrugge, M. W., & Cheng, Y.-T. (2012). Potentiostatic Intermittent Titration Technique for Electrodes Governed by Diffusion and Interfacial Reaction. *The Journal of Physical Chemistry C*, *116*(1), 1472–1478. doi:10.1021/jp207919q
- 193. Baggetto, L., Oudenhoven, J. F. M., van Dongen, T., Klootwijk, J. H., Mulder, M., Niessen, R. A. H., ... Notten, P. H. L. (2009). On the electrochemistry of an anode stack for all-solid-state 3D-integrated batteries. *Journal of Power Sources*, *189*(1), 402–410. doi:10.1016/j.jpowsour.2008.07.076
- 194. Swamy, T., & Chiang, Y.-M. (2015). Electrochemical Charge Transfer Reaction Kinetics at the Silicon-Liquid Electrolyte Interface. *Journal of The Electrochemical Society*, *162*(13), A7129–A7134. doi:10.1149/2.0181513jes
- 195. Fu, Y. B., & Ogden, R. W. (2001). *Nonlinear Elasticity: Theory and Applications*. Cambridge University Press.
- 196. Wang, X.-G., & Smith, J. R. (2005). \$\mathrm{Si}\\mathrm{Cu}\$ Interface Structure and Adhesion. *Physical Review Letters*, 95(15), 156102. doi:10.1103/PhysRevLett.95.156102
- 197. Stournara, M. E., Xiao, X., Qi, Y., Johari, P., Lu, P., Sheldon, B. W., ... Shenoy, V. B. (2013). Li Segregation Induces Structure and Strength Changes at the Amorphous Si/Cu Interface. *Nano Letters*, *13*(10), 4759–4768. doi:10.1021/nl402353k
- 198. Wang, H., Hou, B., Wang, X., Xia, S., & Chew, H. B. (2015). Atomic-Scale Mechanisms of Sliding along an Interdiffused Li–Si–Cu Interface. *Nano Letters*, *15*(3), 1716–1721. doi:10.1021/nl5043837
- 199. Maranchi, J. P., Hepp, A. F., Evans, A. G., Nuhfer, N. T., & Kumta, P. N. (2006). Interfacial Properties of the a-Si/Cu :Active–Inactive Thin-Film Anode System for Lithium-Ion Batteries. *Journal of The Electrochemical Society*, *153*(6), A1246–A1253. doi:10.1149/1.2184753